UNIVERSIDADE DE SÃO PAULO
INSTITUTO DE FÍSICA DE SÃO CARLOS

Carlos Eduardo Máximo

Collective scattering of light from disordered atomic clouds

São Carlos

2017

Carlos Eduardo Máximo

Collective scattering of light from disordered atomic clouds

Thesis presented to the Graduate Program in Physics at the Instituto de Física de São Carlos, Universidade de São Paulo to obtain the degree of Doctor of Science.

Concentration area: Basic Physics

Advisor: Prof. Dr. Romain Pierre Marcel Bachelard
Co-Advisor: Prof. Dr. Philippe Wilhelm Courteille

Original version

São Carlos
2017

Cataloguing data revised by the Library and Information Service
of the IFSC, with information provided by the author

Máximo, Carlos Eduardo
Collective scattering of light from disordered atomic clouds / Carlos Eduardo Máximo; advisor Romain Pierre Marcel Bacheard; co-advisor Philippe Wilhelm Courteille -- São Carlos 2017.
75 p.

Thesis (Doctorate - Graduate Program in Basic Physics) -- Instituto de Física de São Carlos, Universidade de São Paulo - Brasil , 2017.

1. Radiation-matter interaction. 2. Collective scattering of light by cold atoms. 3. Anderson localization of light. 4. Optical binding. I. Pierre Marcel Bacheard, Romain, advisor. II. Wilhelm Courteille, Philippe, co-advisor. III. Title.

ACKNOWLEDGEMENTS

I would like to thank especially my advisor, Prof. Romain Bachelard, for his guidance during these four years and for helping me to be not only a better researcher but also a better person. Thanks for teachings on physics, Matlab, scientific writing, diplomacy, emotional equilibrium and tolerance. I am sure that everything will serve to my whole life.

I would like to thank my co-advisor, Prof. Philippe Courteille, for welcoming me in your group and for all your advices and support over these years.

I would like to thank Prof. Robin Kaiser for his involvement in my Ph.D., especially during my stay in his group in Nice, France. His broad knowledge has made this thesis richer, and I expect that such collaboration goes beyond this Ph.D..

I would like to thank Prof. Nicola Piovella for sharing his dedicated efforts in our common theoretical projects.

I would like to thank Tiago Santiago for his friendship and all our exchanges. My Ph.D. became definitely more interesting with our discussions on politics, economy, science and religion.

I would like to thank Michele Araújo for her assistance during my period abroad, in France, without whom everything would have been much more difficult to be accomplished.

I would like to thank Andrés Salas for the fun conversations and for all his help to prepare such beautiful pictures of science.

I would like to thank the IFSC members, Amilson Fritsch, André Cidrim, André Smaira, Arnor Orozco, Emmanuel Gutierrez, Florent Cottier, Marcos Miotti, Michal Hemmerling, Noel Moreira, Raul Teixeira, Rodrigo Shiozak, Tiago Arruda, and to the former members, Diego Pires and Paulo Moriya, for contributing to my life, even for a short moment.

I would like to thank my parents, Carlos Alberto Maximo and Marta Maximo, who gave me the opportunity to do what I do, and to my wife, Heliny Maximo, for all emotional and spiritual support in the adversity. To them, I dedicate this thesis.

I would like to thank God for giving me hope amid such turbulent times in Brazil.

Finally, I would like to thank the FAPESP (process: 2014/19459-6) and CNPq (process: 149839/2013-8) Brazilian agencies for funding this work and making it possible.

"This much I can say with definiteness - namely, that there is no scientific basis for the denial of religion - nor is there in my judgement any excuse for a conflict between science and religion, for their fields are entirely different. Men who know very little of science and men who know very little of religion do indeed get to quarrelling, and the onlookers imagine that there is a conflict between science and religion, whereas the conflict is only between two different species of ignorance.

The first important quarrel of this sort arose over the advancing by Copernicus of his theory that the earth, instead of being a flat plane and the center of the universe, was actually only one of a number of little planets, rotating once a day upon its axis and circling once a year about the sun. Copernicus was a priest - the canon of a cathedral - and he was primarily a religious rather than a scientific man. He knew that the foundations of real religion are not laid where scientific discoveries of any kind can disturb them. He was persecuted, not because he went against the teachings of religion but because under his theory man was not the center of the universe and this was most displeasing news to a number of egoists."

Robert Andrews Millikan (1868–1953) - Nobel laureate in Physics (1923).

ABSTRACT

MÁXIMO, C. E. **Collective scattering of light from disordered atomic clouds**. 2017. 75p. Thesis (Doctor in Science) - Instituto de Física de São Carlos, Universidade de São Paulo, São Carlos, 2017.

In this thesis, we investigate the coherent scattering of light by atoms randomly distributed in space. As described by a model of coupled dipoles, the cooperation in the spontaneous emission process results from purely optical interactions between the atomic internal degrees of freedom. In the optically dilute regime, where the atomic medium can be described by a refractive index, we have shown that light can be deflected with the application of a gradient of magnetic field. In the dense regime, short-range interactions appear to suppress Anderson localization of light even in two dimensions, a result which disassembles the common belief that "all waves are localized in two dimensions". We also find that the fringe pattern, resulting from the interference between light scattered by an atomic cloud and that of its specular image, is robust to both disorder averaging and saturation. Finally, we demonstrate two-atom bound states in the two-dimensional motion through the long-range optical coupling. This "optical binding effect" with an atom pair will be important to investigate the all-optical stabilization of large clouds.

Keywords: Radiation-matter interaction. Collective scattering of light by cold atoms. Anderson localization of light. Optical binding.

RESUMO

MÁXIMO, C. E. **Espalhamento coletivo de luz por nuvens atômicas desordenadas**. 2017. 75p. Tese (Doutorado em Ciências) - Instituto de Física de São Carlos, Universidade de São Paulo, São Carlos, 2017.

Nesta tese, investigamos o espalhamento coerente de luz por átomos distribuídos aleatoriamente no espaço. Conforme descrito por um modelo de dipolos acoplados, a cooperação no processo de emissão espontânea resulta de interações puramente ópticas entre os graus internos de liberdade dos átomos. No regime opticamente diluído, onde o meio atômico pode ser descrito por um índice de refração, mostramos que a luz pode ser desviada com a aplicação de um gradiente de campo magnético. No regime denso, as interações de curto alcance parecem suprimir a localização de Anderson da luz mesmo em duas dimensões, resultado que desmonta a crença comum de que "todas as ondas estão localizadas em duas dimensões". Também descobrimos que o padrão de franjas, resultante da interferência entre a luz espalhada por uma nuvem atômica e a de sua imagem especular, é robusto tanto contra a média em disordem quanto contra saturação. Finalmente, demonstramos estados ligados de dois átomos no movimento bidimensional através do acoplamento óptico de longo alcance. Este "optical binding effect" com um par de átomos será importante para investigar a estabilização totalmente óptica de nuvens extensas.

Palavras-chave: Interação radiação-matéria. Espalhamento coletivo de luz por átomos frios. Localização de Anderson de luz. Optical binding.

LIST OF FIGURES

CONTENTS

1 INTRODUCTION

The interaction of radiation with matter is one of the most widespread mechanism in nature. It is present from the single atom spontaneous emission in the visible spectrum to astrophysical processes, such as x-ray production in black holes. In our daily life, the electromagnetic radiation reaching our eyes at a given moment has undergone some manifestation of the *scattering* phenomenon, whatever its original source. Looking at a tree in a forest or a cloud in the blue sky, we always see sun rays which were scattered by a multitude of microscopic particles. Even the light coming from a home-made electric bulb does not reach us exactly as it left the hot filament. As a consequence, the final observation strongly depends on the properties of the scattering medium during the light propagation, which rises up a fundamental out-of-equilibrium problem in physics.

The purpose of this thesis is to explore the *collective scattering of light by cold atomic clouds* within different contexts. Although a precise definition of collectivity is still an open discussion,[1] in general, such terminology englobes those phenomena indescribable by a mere extrapolation of the single particle physics. The Nobel laureate Philip Warren Anderson (1977) synthesized this concept with three words: "More Is Different".[2] Collective effects will typically depend either on the atomic density, which is a measure of the typical number of neighbouring atoms, or on the *optical thickness*, where the size of the scattering sample is the most relevant parameter. Optical thickness-induced phenomena are often refereed by the cold atoms community as a *cooperative effect* in light scattering, a definition we also adopt here.

The discussion on cooperativity in the spontaneous emission of atomic ensembles started with the seminal work of Dicke (1954).[3] When considering a set of identical two-level atoms interacting with a single light mode, Dicke pointed out that the spontaneous decay of the many-atom system is dramatically altered by their cooperation. He demonstrated the existence of a coherent *superradiant* emission, as he called it, characterized by a lifetime proportional to the inverse of the number of atoms N. Since the total energy radiated scales linearly with the number of radiators, the total intensity emitted by the atomic ensemble ends up being proportional to N^2, instead of N, as expected for independent atoms. Dicke's publication was first corroborated in the context of nonlinear optics experiments[4] before it inspired a series of new investigations in the 1970s[5,6] and 1980s.[7,8]

The counterpart of superradiance is the *subradiance* effect. It arises when an antisymmetric state decouples from the environment and simply exhibits no decay. In realistic situations, there is always a finite coupling with the environment, so it leads to decay times longer than the one expected for independent atoms. Although subradiance can be considered as a light storage mechanism in atomic ensembles, it should not be

confused with *radiation trapping*[9]: successive incoherent photon absorption (emission) events which are described by a particle-like random walk of photons. For samples with a large number of scatterers, radiation trapping also predicts long photon storage times, as a consequence of the huge number of scattering events necessary to escape the cloud. Yet it completely neglects the wave nature of light (incoherent model), whereas subradiance, like superradiance, is an interference phenomena which only appears in coherent models.[10] Due to the weak coupling of subradiant states with the environment, experiments on subradiance are challenging: There are substantial reports in the context of two[11–13] and many atoms.[14,15]

When only a single atom gets excited in an atomic cloud, one might intuitively expect no cooperative effect since the exchange of photons will be limited. Surprisingly, this is not the correct answer as the system may be prepared in a superposition of states where each atom has a chance to be the excited one. In particular, it was shown that superradiance can occur even in the single-photon regime (*single-photon superradiance*),[16,17] an effect which is of strong interest for quantum information applications.[18–25] This discovery lead to investigations on collective effects in the linear optics regime, stimulating the development of a *Coupled-Dipole Model* (CDM).[26] CDM equations are typically derived from quantum formalisms, as it should be when quantum ingredients are under concern (atoms). Nevertheless, when a low pump intensity is assumed (linear optics regime), these equations acquire a classical form that can be derived from the standard Maxwell equations.[27] Then, it becomes clear that super- and subradiance are not restricted to the quantum world, as first introduced by Dicke, and one may focus on linear optics, leaving apart the exponential grow of more-than-one excitation Hilbert spaces. The whole content of this thesis relies on results which are extracted from this classical Coupled-Dipole Model, so we dedicate the second chapter of this thesis to its derivation.

The CDM approach addresses light-mediated long-range coupling between the atoms and allowed to obtain an accurate description of experiments at a reasonable theoretical and computational cost. It has been successfully supporting experiments in the linear optics regime, including the observation of the cooperative radiation pressure force,[28,29] superradiance[30] and subradiance[15] in large atomic clouds, linewidth broadening and frequency shifts due to motional effects.[31] On the theoretical and numerical side, the amount of results based on several CDM variations are substantial.[32–34] One can cite the study of mechanisms to control subradiance,[35] where the classical ballistic motion of the atoms simulate temperature, and the atomic distribution influence on cooperative spontaneous emission.[36] Interestingly, the latter work demonstrated that the superradiant Dicke limit is only attained in a regular (periodic) distribution of atoms.

In the context of dense atomic clouds with a spherical symmetry, explicit analytical results were obtained from the CDM equations by applying fluid approximations. In this

approach, the atomic cloud appears as a smooth and extended dielectric body, whose refractive index depends on the atomic density. Additionally to sub- and superradiance, this method was also capable to predict Mie resonances in cold atomic clouds[37] and brought new insights regarding on cooperative decay modes.[26] Actually, the first paper of this thesis (Section 3.1), the *Atomic Lighthouse Effect*,[38] is mainly based on this continuous approximation, and we show that the light scattered by an atomic cloud can be deviated by a gradient of magnetic field. Note that the CDM predicts a highly directional superradiant emission whose angular intensity distribution is concentrated in the forward direction.[10] When a gradient of magnetic field is applied orthogonally to the laser propagation, such forward lobe deviates maximally in the optically dilute regime, returning to its original position in the highly cooperative regime. The lighthouse effect represents our first Ph.D. publication, so it served us as an important pedagogical introduction to the community of collective effects in light scattering. An experimental verification of this phenomena is planned on a cold atom experiment in São Carlos-SP.

The microscopic version of the CDM combines light interference with disordered atomic distributions, which brings out the possibility of investigating *Anderson Localization* for light. In 1958, Anderson demonstrated that electronic waves become exponentially localized in space[39] in the presence of disordered potentials. As a result, the electronic diffusion completely ceases and the conductor under concern undergoes a transition to an insulator phase. Yet such transition takes place only in three dimensions (3D), whereas for one (1D) and two dimensions (2D), the electron is always localized whatever the degree of disorder.[40] The interpretation of localization as a interference-induced phenomena lead to its observation in classical waves,[41] as for example, in electromagnetic waves. Light has some important advantages with respect to electrons: photons do not interact with each other during the scattering process in linear optics and the associated experiments are more easily controlled at room temperature. Indeed, there are references in literature claiming localization of light measurements in 1D,[42] 2D[43] and mainly in 3D.[44–46] In particular, the reports in 3D are not consensually accepted. Some groups advocated that the experimental data could be explained by absorption instead localization, and a controversy has established in the community. In order to give an idea of the current status of the discussion, note that one of the groups who has claimed localization observation published a new paper admitting that the results are not unambiguous.[47] Actually, this paper presents a very good summary of the entire controversy, where it becomes clear that Anderson localization of light in 3D still remains an open question.

The community of localization of light lived a small revolution with a new publication entitled "*Absence of Anderson localization of Light in a random ensemble of point scatterers*".[48] In this work, the authors call the attention on an important peculiarity of electromagnetic waves: their vectorial nature. Indeed neither the theory of localization nor previous experimental observations had taken into account polarization effects, yet

this ingredient appears to be responsible for drastic modifications on the light transport in disordered media. Note that a scalar scattering approximation in 3D is reasonable only for dilute regimes and creates long-range correlations between the scatterers. On the contrary, it was expected that Anderson localization of light in 3D could be reached only in dense samples, as in condensed matter systems and in other wave phenomena. Surprisingly, short-range terms which are induced by the vectorial nature of light actually inhibit localization, as demonstrated in[48,49] via scaling analysis. This important result has stimulated us to investigate the role of polarization in 2D, which was supposed to always present localized states. In our publication,[50] included in Section 3.2, we derive an unprecedented two-dimensional model where scalar and vectorial subsystems coexist uncoupled. There, the effect of near-field terms on 2D localization was explored in details by comparing vectorial model with a scalar one which is valid for dense regimes. Such a Ph.D. project contributed with two new pieces of information: 2D localization of light get suppressed by both near field terms and polarization; spatial-like localization (Anderson) seems to be independent from time-like localization (Dicke subradiance).

Disordered samples can also bring out the weak version of localization even for vectorial waves, namely the *Coherent Backscattering of light* (CBS). This effect is understood as the constructive interference between a scattering path, involving two or more scatterers, and its reciprocal (time-reversed) path.[51] Different from strong localization, which is characterized by a constructive interference within the sample, CBS leads to an enhanced scattering into the backward direction with respect to the incident laser.[52,53] It turns out that, when considering cold atoms scattering light, quantum mechanisms are know to break the time-reversal symmetry of reciprocal multiple scattering paths, which makes the CBS effect vanish. For instance, in the strong driving regime, the path information becomes available through the inelastically scattered photons[54,55] and the suitable theoretical treatment of saturation in multiple scattering has not been solved in its full generality.

An alternative to CBS that can still survives in the nonlinear optics regime was explored in this doctorate, namely *mirror-assisted Coherent Backscattering* (mCBS). This different configuration accounts with a reflective interface introduced behind the atomic cloud, which induces constructive interference between the radiation of the atom and that of its image. As shown experimentally and theoretically in one of our papers,[56] more precisely in Section 3.3, mCBS arises through fringes with circular symmetry surrounding the normal to the mirror. Interestingly, this constructive interference can be also observed in optically dilute samples, where multiple scattering is too weak to produce observable signatures. Our work consisted in to understanding theoretically the intensity patterns measurements in both the linear and saturated regimes (i.e., classical and quantum regimes). The characterization of the fringes allowed to determine precisely the position and longitudinal size of the atomic cloud. In the strong field regime, where the atoms are

saturated, the comparison between theoretical and experimental curves demonstrates that, in contrast to the standard CBS, inelastic photons fully contribute to the mCBS fringes.

Since the internal dynamics of the atoms is usually much faster than that of their center-of-mass, for simplicity, in most effects previously mentioned it was assumed motionless particles distributed in vacuum (zero temperature). This regime is achievable thanks to laser-cooling techniques, very common to cold atoms experiments,[57–59] where Doppler broadening can be strongly reduced and coherent cooperative effects could be proven.[15,30] Yet, for longer time scales, the atomic motion couples to the dipole degree of freedom, and such interplay induces the emergence of two fundamental optical forces: the radiation pressure force, which accelerates particles in the light propagation direction,[60] and the dipole force, which tends to trap them into intensity extrema, as for example in optical lattices.[61] Beyond single-particle physics, these optical forces get modified by particles cooperation during the scattering of light. For instance, the radiation pressure force compresses optically thick atomic clouds, as a result of intensity attenuation in the main scattering direction.[62] Also, the gradient force can be cooperatively induced in the scattering of plane waves using nonlinear self-focusing by many-body matter waves.[63]

When various microscopic particles scatter light, the superposition of the re-emitted fields generates radiation pressure force and dipole force between the scatterers. Such interparticle forces can promote long-range spatial reorganization of the system in regions of the order of the light wavelength, an effect called Optical Binding (OB).[64] This effect was foremost investigated with dielectric particles moving in two dimensions within dissipative fluids.[65,66] After these demonstrations, experiments have been mostly realized with pairs of dielectric microsized-spheres interacting with intense light fields, where the bistability of the equilibrium interparticle separations was studied,[67] and optically restoring forces could be measured.[68] Theoretical approaches have focused on demonstrating one-[69] and two-dimensional (2D) [70,71] stability of spheres arrays numerically. In particular, bounded dynamical states were proved only above a critical friction ,[72] an ingredient shared by all OB investigations so far.

The last work of this thesis represents the first theoretical attempt to realize OB with cold atoms (Chapter 4). As such experiments are kept in extremely efficient vacuum conditions, it allows for unprecedented studies on optically bounded motion in the absence of nonradioactive friction. We considered a pair of atoms confined to move in two-dimensions by counterpropagating lasers, where the angular momentum of the binary system ends up a conserved quantity. We show that the field strength induces an unstable-stable dynamical phase transition, which is symmetrical with respect to the resonance. We also demonstrate that the injection of angular momentum in the two-atom system makes the optical binding more efficient. In order to stabilize atomic clouds, magneto-optical traps (MOT) account with inhomogeneous magnetic fields in addition to the laser cooling.

Our study on OB might give insights in how to stabilize large atomic clouds for longer times using only light.

This thesis is organized in a format which is based on the papers of the student. We first present in Chapter 2 the theoretical background which grounds our results, where a general derivation of the Coupled-Dipole Model is included. The already published papers can be found in Chapter 3, whereas a paper close to its submission can be read in a one-column letter format, in Chapter 4. Finally, we draw our general conclusions and discuss the natural continuation of these studies. All supplementary information regarding mathematical steps and less straightforward calculations are located separately in each section of Chapter 3.

2 COUPLED-DIPOLE MODEL

2.1 Hamiltonian for the radiation-matter interaction

Despite its apparent simplicity, the interaction between the radiation field and a one valence electron atom is actually a very challenging problem. The electromagnetic vector potential $\mathbf{A}$ depends nontrivially on relative and center-of-mass coordinates of the atom $(\mathbf{r}, \mathbf{R})$ and also couples to the conjugated momentums $(\mathbf{p}, \mathbf{P})$.[73] In order to simplify the description, one typically consider that the electromagnetic field does not vary substantially over the atom, i.e., the wavelength λ of the field is much larger than the de Broglie wavelength of the atom. Such assumption, known as the dipole approximation, takes into account only the zero order term of the $\mathbf{A}$ multipolar expansion, which depends only on the center-of-mass of the atom. Under this hypothesis, the light-atom Hamiltonian reduces to

$$H = \frac{P^2}{2M} + \frac{1}{2M}\left[\mathbf{p} - e\mathbf{A}\left(\mathbf{R}, t\right)\right]^2 + V\left(|\mathbf{r}|\right) + H_{field}, \tag{2.1}$$

where V is the Coulomb interaction between proton and electron, both with charge of modulus e. The free energy of the field is chosen as H_{field} and M stands for the atom mass.

For non-relativistic center-of-mass motion,[74] one can show that Eq.(2.1) is gauge invariant of

$$\mathcal{H} = H_{atom} + H_{field} + \frac{P^2}{2M} - e\mathbf{r} \cdot \mathbf{E}\left(\mathbf{R}, t\right), \tag{2.2}$$

where $\mathbf{E}$ describes the electric field at the atom center-of-mass. The Hamiltonian $H_{atom} = P^2/2M + V$ represents the atom as a closed system, and its analytical diagonalization leads to the well-known Hydrogen eigenfunctions. When considering the electric field description instead of the vector potential approach, the terminology "dipole approximation" becomes clear: the atom is recognized as an eletric dipole $e\mathbf{r}$ coupled to the light. Interestingly, such apparently naive picture grounds many celebrated results in literature regarding atoms-photons interaction,[75] and the results presented in this thesis also rely on this approximation.

As this thesis focuses on many-atoms interacting through light, the total Hamiltonian must be constructed by superimposing the interaction of each individual atom with the electric field. We start by defining the electric dipole moment of the atom j as $\mathbf{D}_j = e\mathbf{r}_j$ and redefining the center-of-mass coordinates as $\mathbf{R}_j \to \mathbf{r}_j$ and $\mathbf{P}_j \to \mathbf{p}_j$, with $j = 1, 2, \ldots, N$. Therefore, the relative coordinates of the atoms are hereafter identified as their internal degrees of freedom, which are encoded in the electric dipole moment $\mathbf{D}_j$. The center-of-mass coordinates will be referred to as their external degrees of freedom.

One pecularity of electromagnetic waves is their vectorial nature and, based on conservation arguments, they also transfer angular momentum to the atom. In general, it leads to population of the threefold degenerate magnetic structure of the atom, with the transitions evolving coupled. In the dilute regime, this description can be approximated by a two level structure, which is, for example, the relevant regime of our following papers: the Atomic Lighthouse Effect,[38] the Mirror-Assisted Coherent Backscattering[56] and the Optical Binding. However, a scalar theory is no longer a good approximation for Anderson Localization of Light[50] since it arises in the dense regime of disordered medium. Here we proceed on deriving first the vectorial model and, when appropriate, the scalar model will be identified by neglecting the polarization.

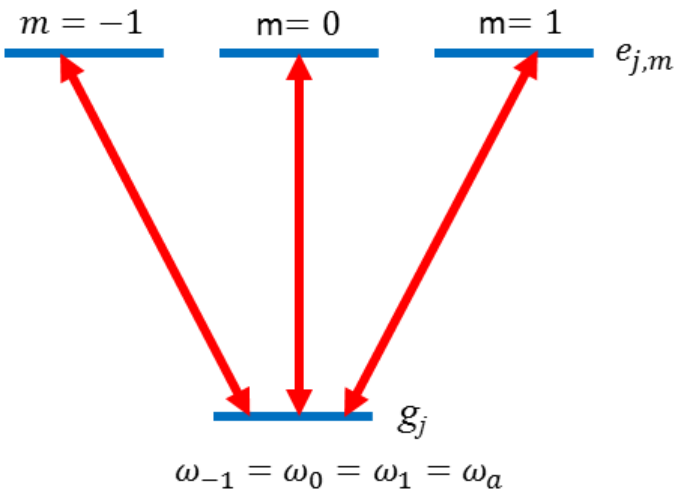

Figure 1 – Energy levels in the vector model of scattering. Three degenerate transitions are allowed.

Source: By the author.

The interaction between atoms and radiation is rigorously described by quantum mechanics, so let us promote all involved variables to operators: $O \to \hat{O}$. Based on the previous paragraph, the level configuration of each atom must respect the polarization selection rules. As represented in Fig.1, only transitions between a nondegenerate ground state $|g_j\rangle$ (angular momentum $\ell = 0$) and a threefold degenerate excited state $|e_{j,m}\rangle$ are allowed, where $m = 0, \pm 1$ indicates the possible projections of the angular momentum $\ell = 1$ on the quantization axis. Note that the transition $m = 0$ is accessed by linearly polarized light, whereas transitions $m = \pm 1$ are pumped by circularly polarized light, all of them with frequency ω_a. Therefore, if the dipole matrix elements $\mathbf{d}_{j,m} = \langle g_j | \hat{\mathbf{D}}_j | e_{j,m} \rangle$ are written in the diagonal base of H_{atom}, the Hamiltonian (2.2) can be cast in its fully

quantum form:

$$\begin{aligned}\hat{H} &= \frac{1}{2}\sum_{j=1}^{N}\left(\hbar\omega_a\hat{\sigma}_{z,j}+\frac{\hat{p}_j^2}{M}\right)+\hbar\sum_{\mathbf{k},s}\omega_{\mathbf{k}}\left(\hat{a}_{\mathbf{k},s}^{\dagger}\hat{a}_{\mathbf{k},s}+\frac{1}{2}\right)\\ &+\hbar\sum_{j=1}^{N}\sum_{m=-1}^{1}\sum_{\mathbf{k},s}\left(\hat{a}_{\mathbf{k},s}^{\dagger}e^{-i\mathbf{k}\cdot\hat{\mathbf{r}}_j}+\hat{a}_{\mathbf{k},s}e^{i\mathbf{k}\cdot\hat{\mathbf{r}}_j}\right)\left(g_{\mathbf{k},s}^{j,m}\hat{\sigma}_j^{(m)}+g_{\mathbf{k},s}^{j,m*}\hat{\sigma}_j^{\dagger(m)}\right)\\ &+\frac{\hbar}{2}\sum_{j=1}^{N}\sum_{m=-1}^{1}\left(\Omega_m\left(\hat{\mathbf{r}}_j\right)\hat{\sigma}_j^{(m)}e^{i\omega_0 t}+\Omega_m^{*}\left(\hat{\mathbf{r}}_j\right)\hat{\sigma}_j^{\dagger(m)}e^{-i\omega_0 t}\right). \qquad (2.3)\end{aligned}$$

In the first line of Eq.(2.3) , the diagonal single-atom term H_{atom} is now replaced by the superposition of the following operators

$$\hat{\sigma}_{z,j}=\sum_{m=-1}^{1}\left|e_{j,m}\right\rangle\left\langle e_{j,m}\right|-\left|g_j\right\rangle\left\langle g_j\right|, \qquad (2.4)$$

which represents the free energy of each atom. The free field Hamiltonian H_{field} become represented as a sum over the energy of an infinity of uncoupled oscillators, with frequency $\omega_{\mathbf{k}}=|\mathbf{k}|c$, which arises from the electric field expansion in terms of creation $\hat{a}_{\mathbf{k},s}$ and annihilation operators $\hat{a}_{\mathbf{k},s}^{\dagger}$. The atomic transitions are realized by the lowering $\hat{\sigma}_j^{(m)}=\left|g_j\right\rangle\left\langle e_{j,m}\right|$ and rising $\hat{\sigma}_j^{\dagger(m)}=\left|e_{j,m}\right\rangle\left\langle g_j\right|$ operators. Additionally, one can observe that the atom-field interaction has been subdivided into two contributions: atoms interacting with a driving field, of Rabi frequency $\Omega_m\left(\hat{\mathbf{r}}_j\right)$, and atoms interacting with an infinity set of vacuum modes $(\mathbf{k},\hat{\mathbf{e}}_{\mathbf{k},s})$. The former pumps transitions m without being affected by individual photon emissions (classical field approximation). The latter interaction has coupling frequency

$$g_{\mathbf{k},s}^{j,m}=\hat{\mathbf{e}}_{\mathbf{k},s}\cdot\mathbf{d}_{j,m}\sqrt{\frac{\omega_{\mathbf{k}}}{2\hbar\epsilon_0\mathcal{V}}}, \qquad (2.5)$$

where the quantities $\hbar$, ϵ_0 and $\mathcal{V}$ are, respectively, the Planck's constant, the vacuum permittivity and the quantization volume. The dynamics governed by Hamiltonian (2.3) cover all results contained in the present thesis, so in the following section, we derive from it the associated effective dynamics of the atoms.

2.2 Atomic cloud dynamics

As discussed in the introduction, cooperativity in coherent spontaneous emission was first introduced in the quantum context,[3] however, many non-trivial cooperative phenomena arise within the classical theory.[26,27] In the present section, we derive a classical master equation which grounds the results of this thesis: the Coupled-Dipole Model (CDM).

For low pump intensity, the linear optics regime is implemented on the atoms commutation relations through the following approximation:

$$\left[\hat{\sigma}_j^{\dagger(m)},\hat{\sigma}_{j'}^{(m')}\right]=\left(\left|e_{j,m}\right\rangle\left\langle e_{j,m}\right|-\left|g_j\right\rangle\left\langle g_j\right|\right)\delta_{j,j'}\delta_{m,m'}\approx-\delta_{j,j'}\delta_{m,m'}. \qquad (2.6)$$

Such assumption neglects multi-excitation in the atomic system by restricting the total Hilbert space to the single excitation basis $|g_1,\ldots,g_N\rangle$, $|e_{1,m},g_2,\ldots,g_N\rangle$, $|g_1,e_{2,m},\ldots,g_N\rangle$, $\ldots$,$|g_1,\ldots,g_{N-1},e_{N,m}\rangle$. Relation (2.6) rather reduces the complexity of the quantum problem since it leads to a linear instead of exponential growth with the system size.

Combining hypothesis (2.6) with the commutation relations

$$\left[\hat{\sigma}_j^{(m)},\hat{\sigma}_{z,j'}^{(m')}\right] = 2\hat{\sigma}_j^{(m)}\delta_{j,j'}\delta_{m,m'}, \tag{2.7}$$

$$\left[\hat{a}_{\mathbf{k},s},\hat{a}_{\mathbf{k}',s'}^{\dagger}\right] = \delta_{s,s'}\delta_{\mathbf{k},\mathbf{k}'}, \tag{2.8}$$

$$\left[\hat{\mathbf{p}}_j,\hat{H}\left(\hat{\mathbf{r}}_l\right)\right] = -i\hbar\nabla_{\mathbf{r}_j}\hat{H}\left(\hat{\mathbf{r}}_l\right), \tag{2.9}$$

one obtains the following Heisenberg equations of motion:

$$\frac{d\hat{a}_{\mathbf{k},s}}{dt} = -i\omega_{\mathbf{k}}\hat{a}_{\mathbf{k},s} - i\sum_{j=1}^{N}\sum_{m=-1}^{1}\left(g_{\mathbf{k},s}^{j,m}\hat{\sigma}_j^{(m)} + g_{\mathbf{k},s}^{j,m*}\hat{\sigma}_j^{\dagger(m)}\right)e^{-i\mathbf{k}\cdot\hat{\mathbf{r}}_j}, \tag{2.10}$$

$$\frac{d\hat{\sigma}_j^{(m)}}{dt} = -i\omega_a\hat{\sigma}_j^{(m)} - \frac{i}{2}\Omega_m^*\left(\hat{\mathbf{r}}_j\right)e^{-i\omega_0 t} - i\sum_{\mathbf{k},s}g_{\mathbf{k},s}^{j,m*}\left(\hat{a}_{\mathbf{k},s}e^{i\mathbf{k}\cdot\hat{\mathbf{r}}_j} + \hat{a}_{\mathbf{k},s}^{\dagger}e^{-i\mathbf{k}\cdot\hat{\mathbf{r}}_j}\right), \tag{2.11}$$

$$M\frac{d^2\hat{\mathbf{r}}_j}{dt^2} = -\nabla_{\hat{\mathbf{r}}_j}\hat{H}(\hat{\mathbf{r}}). \tag{2.12}$$

The equations above demonstrate that the dynamics of the vacuum modes of the field are coupled to internal and external degrees of freedom of the atoms. Since the modes of the radiation field behave as a reservoir with infinite degrees of freedom, it is convenient to substitute the formal solution of Eq.(2.10) in Eq.(2.11) and Eq.(2.12), by assuming the vacuum as the initial condition for the field. Thus, performing the unitary transformations

$$\hat{\sigma}_j^{(m)} \to \hat{\sigma}_j^{(m)}e^{i\omega_0 t}, \qquad \hat{a}_{\mathbf{k},s} \to \hat{a}_{\mathbf{k},s}e^{i\omega_{\mathbf{k}}t}, \tag{2.13}$$

the internal and external dynamics of the atoms can be respectively written in the form

$$\frac{d\hat{\sigma}_j^{(m)}}{dt} = i\Delta\hat{\sigma}_j^{(m)} - \frac{i}{2}\Omega_m^*\left(\hat{\mathbf{r}}_j\right) - \sum_{l=1}^{N}\sum_{n=-1}^{1}\sum_{\mathbf{k},s}g_{\mathbf{k},s}^{j,m*}\int_0^t d\tau\left(e^{-i\omega_{\mathbf{k}}\tau+i\mathbf{k}\cdot\hat{\mathbf{r}}_{jl}(t-\tau)} - c.c.\right)\times$$
$$\times\left(g_{\mathbf{k},s}^{l,n}\hat{\sigma}_l^{(n)}\left(t-\tau\right)e^{i\omega_0\tau} + g_{\mathbf{k},s}^{l,n*}\hat{\sigma}_l^{\dagger(n)}\left(t-\tau\right)e^{i\omega_0(2t-\tau)}\right), \tag{2.14}$$

$$\begin{aligned}
M\frac{d^2\hat{\mathbf{r}}_j}{dt^2} = & -\frac{\hbar}{2}\nabla_{\hat{\mathbf{r}}_j}\sum_{m=-1}^{1}\left(\Omega_m\left(\hat{\mathbf{r}}_j\right)\hat{\sigma}_j^{(m)} + \Omega_m^*\left(\hat{\mathbf{r}}_j\right)\hat{\sigma}_j^{\dagger(m)}\right)\\
& -i\hbar\nabla_{\hat{\mathbf{r}}_j}\sum_{l=1}^{N}\sum_{m,n=-1}^{1}\sum_{\mathbf{k},s}g_{\mathbf{k},s}^{j,m}\hat{\sigma}_j^{(m)}\int_0^t d\tau\left(e^{i\omega_{\mathbf{k}}\tau-i\mathbf{k}\cdot\hat{\mathbf{r}}_{jl}(t-\tau)} - c.c.\right)\times\\
& \times\left(g_{\mathbf{k},s}^{l,n}\hat{\sigma}_l^{(n)}\left(t-\tau\right)e^{-i\omega_0(2t-\tau)} + g_{\mathbf{k},s}^{l,n*}\hat{\sigma}_l^{\dagger(n)}\left(t-\tau\right)e^{-i\omega_0\tau}\right)\\
& -i\hbar\nabla_{\hat{\mathbf{r}}_j}\sum_{l=1}^{N}\sum_{m,n=-1}^{1}\sum_{\mathbf{k},s}g_{\mathbf{k},s}^{j,m*}\hat{\sigma}_j^{\dagger(m)}\int_0^t d\tau\left(e^{i\omega_{\mathbf{k}}\tau-i\mathbf{k}\cdot\hat{\mathbf{r}}_{jl}(t-\tau)} - c.c.\right)\times\\
& \times\left(g_{\mathbf{k},s}^{l,n}\hat{\sigma}_l^{(n)}\left(t-\tau\right)e^{i\omega_0\tau} + g_{\mathbf{k},s}^{l,n*}\hat{\sigma}_l^{\dagger(n)}\left(t-\tau\right)e^{i\omega_0(2t-\tau)}\right),
\end{aligned} \tag{2.15}$$

where we define the relative position coordinate operator between two atoms $\hat{\mathbf{r}}_{jl} \equiv \hat{\mathbf{r}}_j - \hat{\mathbf{r}}_l$ and the detuning $\Delta \equiv \omega_0 - \omega_a$.

As we are interested in evolution times satisfying $t \gg \max\left(|\mathbf{r}_{jl}|/c\right)$ and $t \gg 1/\omega_0$, with $|\mathbf{r}_{jl}|/c$ the photon time-of-flight between any pair of atoms, retardation effects can be neglected by applying the Markov approximation:

$$\hat{\sigma}_l^{(n)}(t-\tau) \approx \hat{\sigma}_l^{(n)}(t), \qquad \hat{\mathbf{r}}_{jl}(t-\tau) \approx \hat{\mathbf{r}}_{jl}(t). \tag{2.16}$$

Additionally, the terms proportional to $e^{i\omega_0(2t-\tau)}$ in Eq.(2.14) and Eq.(2.15) oscillates much faster than those $e^{i\omega_0\tau}$, so they do not contribute in average to the dynamics (Rotating Wave Approximation). All these assumptions are very useful to make the many-atom dynamics tractable and yields the following general equations of motion

$$\frac{d\hat{\sigma}_j^{(m)}}{dt} = i\Delta\hat{\sigma}_j^{(m)} - \frac{i}{2}\Omega_m^*(\hat{\mathbf{r}}_j) - \frac{1}{2}\sum_{n=-1}^{1}\sum_{l=1}^{N} K_{m,n}(\hat{\mathbf{r}}_{jl})\,\hat{\sigma}_l^{(n)}, \tag{2.17}$$

$$M\frac{d^2\hat{\mathbf{r}}_j}{dt^2} = -\frac{\hbar}{2}\nabla_{\hat{\mathbf{r}}_j}\sum_{m=-1}^{1}\left(\Omega_m(\hat{\mathbf{r}}_j)\,\hat{\sigma}_j^{(m)} + \Omega_m^*(\hat{\mathbf{r}}_j)\,\hat{\sigma}_j^{\dagger(m)}\right)$$

$$+\frac{i\hbar}{2}\nabla_{\hat{\mathbf{r}}_j}\sum_{l=1}^{N}\sum_{m,n=-1}^{1}\left(K_{m,n}(\hat{\mathbf{r}}_{jl})\,\hat{\sigma}_j^{\dagger(m)}\hat{\sigma}_l^{(n)} - K_{m,n}^*(\hat{\mathbf{r}}_{jl})\,\hat{\sigma}_j^{(m)}\hat{\sigma}_l^{\dagger(n)}\right), \tag{2.18}$$

where we define the generalized scattering Kernel

$$K_{m,n}(\hat{\mathbf{r}}_{jl}) \equiv 2\int_0^\infty d\tau e^{i\omega_0\tau}\sum_{\mathbf{k},s} g_{\mathbf{k},s}^{j,m*} g_{\mathbf{k},s}^{l,n}\left(e^{-i\omega_{\mathbf{k}}\tau + i\mathbf{k}\cdot\hat{\mathbf{r}}_{jl}} - e^{i\omega_{\mathbf{k}}\tau - i\mathbf{k}\cdot\hat{\mathbf{r}}_{jl}}\right). \tag{2.19}$$

As a consequence of the Markov approximation, the upper bound of the time integral in Eq.(2.19) was extended to infinity.

In order to calculate the evolution of the operators expected values, let us remind that we are under the dipole approximation. Therefore, the typical width of the atom is much smaller than the optical wavelength, which requires an atomic lifetime much shorter than its recoil time $2M\lambda/\hbar$. Such condition allows us to replace the position and momentum operators by classical variables ($\hat{\mathbf{r}}_j \to \mathbf{r}_j$ and $\hat{\mathbf{p}}_j \to \mathbf{p}_j$). On the dipole side, the dynamics of the expected values $\langle\hat{\sigma}_l^{(n)}\rangle \equiv \beta_l^{(n)}$ completely determines the internal motion of the atoms since quantum correlations do not play any role in the linear optics regime ($\langle\hat{\sigma}_j^{(m)\dagger}\hat{\sigma}_l^{(n)}\rangle \approx \beta_j^{*(m)}\beta_l^{(n)}$).[76] Thus, the classical equations of motion takes the following simpler form

$$\dot{\beta}_j^{(m)} = i\Delta\beta_j^{(m)} - \frac{i}{2}\Omega_m^*(\mathbf{r}_j) - \frac{1}{2}\sum_{n=-1}^{1}\sum_{l=1}^{N} K_{m,n}(\mathbf{r}_{jl})\,\beta_l^{(n)}, \tag{2.20}$$

$$\ddot{\mathbf{r}}_j = -\frac{\hbar}{M}\mathrm{Re}\left[\sum_{m=-1}^{1}\nabla_{\mathbf{r}_j}\Omega_m(\mathbf{r}_j)\,\beta_j^{(m)}\right]$$

$$-\frac{\hbar}{M}\mathrm{Im}\left[\sum_{l\neq j}\sum_{m,n=-1}^{1}\nabla_{\mathbf{r}_j}K_{m,n}(\mathbf{r}_{jl})\,\beta_j^{*(m)}\beta_l^{(n)}\right]. \tag{2.21}$$

Reminding that the most accessible source of information in cold atom experiments is the scattered light, which is based on photon absorption, the scattered electric field can be derived from the expression

$$\hat{\mathbf{E}}_s(\mathbf{r}) = \sum_{\mathbf{k},s} \sqrt{\frac{\hbar\omega_{\mathbf{k}}}{2\epsilon_0 V}}\, \hat{\mathbf{e}}_{\mathbf{k},s} \hat{a}_{\mathbf{k},s} e^{-i\omega_{\mathbf{k}} t + i\mathbf{k}\cdot\mathbf{r}}, \tag{2.22}$$

which is proportional to the photon annihilation operators.[77] With similar procedures presented so far, it is possible to obtain the total classical electric field in terms of the generalized kernel as

$$\mathbf{E}(\mathbf{r}) = \mathbf{E}_0(\mathbf{r}) + \frac{\hbar}{2di} \sum_{j=1}^{N} \overleftrightarrow{\mathbf{K}}(\mathbf{r} - \mathbf{r}_j) \cdot \boldsymbol{\beta}_j, \tag{2.23}$$

where $\mathbf{E}_0(\mathbf{r})$ is the incident electric field. Observe that, in the circular polarized basis ($\hat{\mathbf{e}}_{\pm 1} = (\hat{\mathbf{x}} \pm i\hat{\mathbf{y}})/\sqrt{2}$ and $\hat{\mathbf{e}}_0 = \hat{\mathbf{z}}$), we have defined the following mathematical objects:

$$\left[\overleftrightarrow{\mathbf{K}}(\mathbf{r} - \mathbf{r}_j)\right]_{m,n} \equiv K_{m,n}(\mathbf{r} - \mathbf{r}_j), \tag{2.24}$$

$$\left[\boldsymbol{\beta}_j\right]_m \equiv \beta_j^m. \tag{2.25}$$

At this point, it is worth emphasizing the importance of two contributions which have a strong influence on the atomic dynamics. First: the incident field profile $\mathbf{E}_0(\mathbf{r})$, which induces population, radiation pressure force and dipole force on the atoms, by means of the Rabi frequency $\Omega_m(\hat{\mathbf{r}}_j)$. Second: the generalized kernel $K_{m,n}(\hat{\mathbf{r}}_{jl})$, which depends on the superposition of all vacuum modes (see Eq.(2.19)) and leads to an effective coupling between the transition m of the atom j with transition n of the atom l. In particular, the gradient of the modulus of K generates dipole forces between atoms (see Eq.(2.21)), whereas the gradient of its phase gives rise to the radiation pressure force. Such interatomic forces are at the heart of our optical binding studies, in Chapter 4. Nevertheless, the optical force (2.21) is fully neglected in the papers of Chapter 3 ($\ddot{\mathbf{r}}_j \approx \dot{\mathbf{r}}_j \approx 0$), once the time scale under study there is much smaller than that of the center-of-mass motion. Finally, one must also note that, while the dipoles amplitude $\beta_l^{(n)}$ respond linearly to the light fields (see Eq.(2.20)), the coupling with their center-of-mass $\mathbf{r}_j$ introduces a nonlinearity in the system, which makes of the present problem even less trivial.

In the following, we discuss some examples of explicit effective interactions between atoms, which are obtained by integration over the vacuum modes in different configurations.

2.3 Light-mediated effective interaction

The spontaneous emission process naturally occurs in the three-dimensional space, so the light emitted from an atom has a finite probability to propagate in any direction. In order to avoid treating an infinite number of propagation directions in space, a typical

approach for a dense distribution consists in replacing the discrete sum over the **k**-space (see Eq.(2.19)) by the 3D integral[78]

$$\sum_{\mathbf{k}_{3D}} \rightarrow \frac{\mathcal{V}}{(2\pi)^3} \int d^3k. \tag{2.26}$$

The result gives rise to the single atom decay rate

$$K^{3D}_{m,n}\left(\mathbf{r}_{jl}=\mathbf{0}\right) = \frac{k_0^3 d^2}{3\pi\hbar\epsilon_0}\delta_{m,n} \equiv \Gamma_{3D}\delta_{m,n}, \tag{2.27}$$

and to the 3D vector kernel

$$K^{3D}_{m,n}\left(\mathbf{r}_{jl}\neq\mathbf{0}\right) = \Gamma_{3D}\frac{3}{2}\frac{e^{ik_0 r_{jl}}}{ik_0 r_{jl}}\left[\delta_{m,n}\left(1-\frac{1}{k_0^2 r_{jl}^2}+\frac{i}{k_0 r_{jl}}\right)+\mathcal{D}^{3D}_{m,n}\left(\frac{3}{k_0^2 r_{jl}^2}-\frac{3i}{k_0 r_{jl}}-1\right)\right], \tag{2.28}$$

where we have defined the directional function

$$\mathcal{D}^{3D}_{m,n}\left(\theta_{jl},\varphi_{jl}\right) = (-1)^{\delta_{m,n}+1}\, e^{i(n-m)\varphi_{jl}}\cos^2\theta_{jl}\left(\frac{\tan\theta_{jl}}{\sqrt{2}}\right)^{|m|+|n|}, \tag{2.29}$$

and the vector difference between any two atoms

$$\mathbf{r}_{jl} = r_{jl}\sin\theta_{jl}\cos\varphi_{jl}\hat{\mathbf{x}} + r_{jl}\sin\theta_{jl}\sin\varphi_{jl}\hat{\mathbf{y}} + r_{jl}\cos\theta_{jl}\hat{\mathbf{z}}. \tag{2.30}$$

Solutions (2.27)-(2.28) are not the focus of our work, however, the steps taken toward it are exactly the same to those adopted for 2D scattering, as exhibited in reference.[50]

Eq.(2.28) contains a competition between far-field ($1/r$) and near-field terms ($1/r^2$ and $1/r^3$), where the density of the atomic cloud determines which ones will dominate. On the one hand, near-field terms are important in the dense regime, so they should be accounted when studying Anderson localization of light. On the other hand, several experiments are operated in the optically dilute regime, where long-range terms dominate over near-field ones and polarization can be neglected. Actually, the scalar approximation can be derived considering a simple two-level system that decays in a set of vacuum modes.[26] In the latter scenario, it is much more convenient to work on a simplified spherically symmetric version of the scattering kernel, namely

$$K^{3D}_{m,n}\left(\mathbf{r}_{jl}\neq\mathbf{0}\right) \approx \Gamma\frac{e^{ik_0 r_{jl}}}{ik_0 r_{jl}}\delta_{m,n}, \tag{2.31}$$

with $\Gamma = 3\Gamma_{3D}/2$. Eq.(2.31) represents the so-called scalar Green function which leads to the simpler electric field expression

$$E\left(\mathbf{r}\right) = E_0\left(\mathbf{r}\right) + \frac{\hbar\Gamma}{id}\sum_{j=1}^{N}\frac{e^{ik_0|\mathbf{r}-\mathbf{r}_j|}}{k_0\left|\mathbf{r}-\mathbf{r}_j\right|}\beta j. \tag{2.32}$$

Equation above has been used with great success to describe cold atom experiments in the dilute regime[15,28,30] and also grounds theoretical efforts of this thesis.

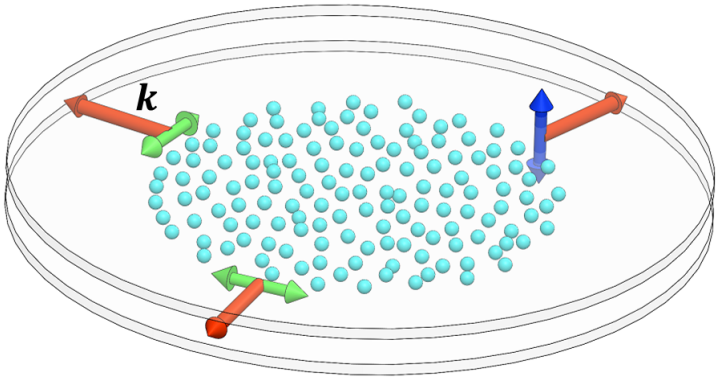

Figure 2 – Two-dimensional scattering scheme: the wave number k, close to resonance $k \approx k_0 = \omega_0/c$, is confined in the plane (x, y). This is possible because the cavity is tuned away from the resonance. At this limit, s-polarized light (blue arrow) completely decouples from the p-polarized light (green arrow).

Source: By the author.

A novelty of this thesis relies on the two-dimensional scattering condition

$$\sum_{\mathbf{k}_{2D}} \rightarrow \frac{V}{(2\pi)^3} \int d^3k \delta\left(\theta - \pi/2\right), \tag{2.33}$$

where the accessible vectors $\mathbf{k}$ satisfies the parametrization in polar coordinates $\mathbf{k} = k\left(\cos\phi, \sin\phi, 0\right)$, with $k = |\mathbf{k}|$ and $\phi \in [0; 2\pi]$. This situation can be generated, for example, inside a high finesse cavity, as outlined in Fig.2, when the atomic resonance is far-detuned from the cavity frequency. Then the probability of finding modes along the cavity axis is almost zero and the accessible vacuum modes must occupy only the cavity plane (x, y). The smaller the spacing between mirrors compared to their radius the closer the experiment become to our model. In the microwave regime, a similar experimental setup was achieved using micro-cylinders instead of atoms.[43] As can be noted in Chapter 3, the 2D condition (2.33) predicts two uncoupled subsystems, with two different single atom decay channels

$$K^{2D}_{m,n}\left(\mathbf{r}_{jl} = \mathbf{0}\right) = \delta_{m,n} \frac{k_0^3 d^2}{8\pi\hbar\epsilon_0} \left(2\delta_{m,0} + \delta_{|m|,1}\right) \equiv \delta_{m,n} \left(\Gamma_0 \delta_{m,0} + \Gamma_1 \delta_{|m|,1}\right), \tag{2.34}$$

and the 2D scattering kernel

$$K^{2D}_{m,n}\left(\mathbf{r}_{jl} \neq \mathbf{0}\right) = K^{2D}_{m,n}\left(\mathbf{r}_{jl} = \mathbf{0}\right) H_0\left(k_0 r_{jl}\right) + \Gamma_1 \delta_{1,|m|} \delta_{m,-n} e^{2im\varphi_{jl}} H_2\left(k_0 r_{jl}\right). \tag{2.35}$$

We have defined here the angle $\varphi_{jl} = \arctan\left(y_{jl}/x_{jl}\right)$ which determines the direction of the vector difference between each atom $\mathbf{r}_{jl} = r_{jl}\left(\cos\varphi_{jl}, \sin\varphi_{jl}\right)$. Observe that the decoupling between transitions does not arise from the application of a Zeeman magnetic field, where the three excited levels become non-degenerate, but from the geometric constraint imposed

by the cavity. A detailed derivation of the quantities (2.34) and (2.35) can be found in the paper of Section 3.2.

In the 2D scattering, the effective interactions between the atoms are thus represented by Hankel functions: H_0 is solution of the radial part of the 2D Helmholtz equation, known as the scalar Green function in 2D, and couples atoms that occupy the same sub levels, whereas the different transitions $m = \pm 1$ are coupled by the term H_2. Depending on the density regime, these functions can also cover different ranges, as can be seen in Table 1. Additional details and discussions on all topics can be found in the corresponding papers next Chapter.

Table 1 – Asymptotic Hankel functions expressions.

-	$H_0(x)$	$H_2(x)$
$x \to \infty$	$\frac{(1-i)e^{ix}}{\sqrt{x}}$	$-\frac{(1-i)e^{ix}}{\sqrt{x}}$
$x \to 0$	$\frac{2i\ln x}{\pi} + cte$	$-\frac{4i}{\pi x^2} + cte$

Source: By the author.

3 PAPERS

3.1 Atomic Lighthouse Effect

Máximo *et al.* Vol. 31, No. 11 / November 2014 / J. Opt. Soc. Am. A 2511

Atomic lighthouse effect

C. E. Máximo,[1,*] R. Kaiser,[2] Ph. W. Courteille,[1] and R. Bachelard[1]

[1]*Instituto de Física de São Carlos, Universidade de São Paulo, 13560-970 São Carlos, SP, Brazil*
[2]*Université de Nice Sophia Antipolis, CNRS, Institut Non-Linéaire de Nice, UMR 7335, F-06560 Valbonne, France*
**Corresponding author: dumax1@gmail.com*

Received July 29, 2014; revised September 22, 2014; accepted September 22, 2014;
posted September 23, 2014 (Doc. ID 219885); published October 27, 2014

We investigate the deflection of light by a cold atomic cloud when the light–matter interaction is locally tuned via the Zeeman effect using magnetic field gradients. This "lighthouse" effect is strongest in the single-scattering regime, where deviation of the incident field is largest. For optically dense samples, the deviation is reduced by collective effects, as the increase in linewidth leads to a decrease in magnetic field efficiency. © 2014 Optical Society of America

OCIS codes: (020.0020) Atomic and molecular physics; (020.1670) Coherent optical effects; (020.7490) Zeeman effect; (290.4210) Multiple scattering.
http://dx.doi.org/10.1364/JOSAA.31.002511

1. INTRODUCTION

The interference of light scattered by different particles of an ensemble is at the origin of a variety of collective phenomena such as superradiance [1], Bragg scattering, or collective frequency shifts [2–4]. The phenomena can be classified in two distinct regimes according to whether the scatterers interact with each other via mediation of the incident light or not. Bragg scattering, for example, is the result of a far-field interference of the light waves scattered by an optically dilute, periodic structure. In this case, even in the absence of communication between the scatterers, the radiated light pattern provides information on the scattering structure, a fact that is extensively used, e.g., in crystallography. On the other hand, optically dense structures lead to multiple scattering and strong interference in the near-field (i.e., within the structure) between the light waves scattered from different particles. One example is the opening of photonic bandgaps in period structures [5–9].

Cold atomic clouds are particularly attractive experimentation platforms as powerful techniques not only to shape the density distribution but also to fine-tune the light–matter interaction over wide ranges. Here, we show that sufficiently cold atomic clouds exposed to a gradient of the strength of the light–matter interaction deflect light due to collective scattering in the single-scattering regime. We propose to implement the required gradient by an inhomogeneous magnetic field exploiting the Zeeman effect. Because this phenomenon is reminiscent of an effect studied in nuclear physics called the "lighthouse effect" [10–13], we call this effect the "atomic lighthouse effect."

The nuclear lighthouse effect was used to perform spectroscopy and the transformation from time to angular coordinates allowed us to detect timescales difficult to achieve with present detection schemes. Similar light deviation effects have been experimentally observed for light passing through an atomic vapor in slow light and electromagnetically induced transparency schemes using either magnetically [14,15] or optically induced gradients [16,17].

We will show in this paper that the atomic lighthouse effect can be obtained on a two-level scheme and is a result of the interference of the light radiated by independent atoms. Similar to Bragg scattering, it is thus fully determined by the single-photon structure factor of the atomic cloud. However, light-induced interatomic cooperation dramatically *alters* the lighthouse effect in the case of optically dense samples. We prove this via calculations and simulations accounting for the light-induced interactions between the atoms in the multiple-scattering regime. The alteration can be understood as an increase in the atomic linewidth, due to the atoms' cooperation, that reduces the Zeeman effect. Hence, the reduction of the lighthouse effect provides a direct signature of cooperativity.

2. COUPLED DIPOLE MODEL

We describe the light deviation by a cloud of atoms with a model treating all atomic dipoles as being coupled via the incident light. This allows us to account for interferences between these dipoles in the optically dense regime. Photon random walk approaches are not sufficient. Furthermore, all dipoles are exposed to a locally varying atom–light interaction inducing an inhomogeneous phase profile of the dipole excitation across the atomic cloud.

Let us start by considering an ensemble of N two-level (g and e) atoms, each at a position $\mathbf{r}_j$ ($j = 1, 2, \ldots N$), driven by a uniform laser beam with wave vector $\mathbf{k}_0 = k_0\hat{\mathbf{z}}$. The detuning of the light from the atomic resonance is $\Delta_0 = \omega_0 - \omega_a$, and the Rabi frequency is $\Omega_0 = dE_0/\hbar$, where d is the dipole matrix element, E_0 is the field amplitude, and $\hbar$ is the Planck constant. The atom–light interaction is locally tuned with a inhomogeneous magnetic field in the quantization direction $\mathbf{B}(\mathbf{r}_j) = \hat{\mathbf{z}}B(\mathbf{r}_j)$ (see Fig. 1).

Let us consider an electronic transition with a structureless ground state and single excited state Zeeman level. This system is described by the following Hamiltonian [18] in the rotating wave approximation:

2512 J. Opt. Soc. Am. A / Vol. 31, No. 11 / November 2014 Máximo *et al.*

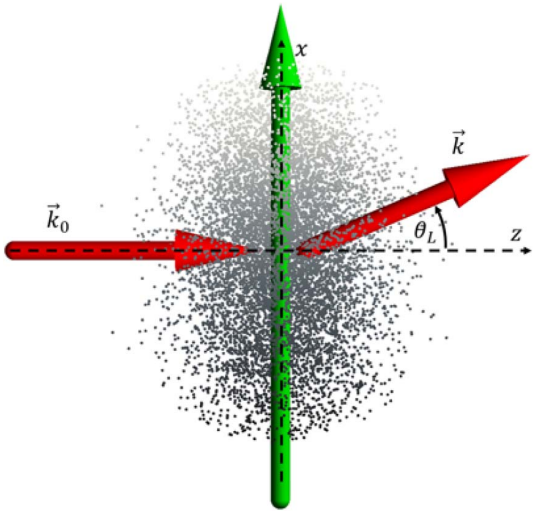

Fig. 1. Scheme of the atomic lighthouse effect. An incident laser beam labeled by its wave vector, $\mathbf{k}_0$, is scattered from a cloud of cold atoms to which a transverse magnetic field gradient, ∇B, is applied. As a consequence, the light is deviated by an angle θ_L.

$$\hat{H} = \frac{\hbar\Omega_0}{2}\sum_{j=1}^{N}(\hat{\sigma}_-^{(j)}e^{i\Delta_0 t - i\mathbf{k}_0\cdot\mathbf{r}_j} + \text{h.c.}) + \hbar\sum_{j=1}^{N}\sum_{\mathbf{k}} g_{\mathbf{k}}(\hat{\sigma}_-^{(j)}\hat{a}_{\mathbf{k}}^{\dagger}e^{i\Delta_{\mathbf{k}}t - i\mathbf{k}\cdot\mathbf{r}_j} + \text{h.c}) - \frac{\hbar}{2}\sum_{j=1}^{N}\Delta(\mathbf{r}_j)\sigma_z^{(j)}. \quad (1)$$

$\Delta_{\mathbf{k}} = \omega_{\mathbf{k}} - \omega_a$ is the detuning between the field emitted into mode $\mathbf{k}$ and the atomic transition ω_a. $g_{\mathbf{k}} = d\sqrt{\omega_k/\hbar\varepsilon_0 V_\nu}$ is the single-photon Rabi frequency for a photon volume V_ν. $\Delta(\mathbf{r}_j) = \mu_B m_j B(\mathbf{r}_j)/\hbar$ describes the (inhomogeneous) Zeeman effect, $\hat{\sigma}_-^{(j)} = |g_j\rangle\langle e_j|$ and $\hat{\sigma}_z^{(j)} = |e_j\rangle\langle e_j| - |g_j\rangle\langle g_j|$ are the Pauli matrices describing the de-excitation and the excited state population of atom j, respectively, whereas $\hat{a}_{\mathbf{k}}$ describes the photon annihilation in the mode $\mathbf{k}$. Note that the above model describes scalar light, an approximation valid for low density of atoms.

Under the Markov approximation and neglecting recoil or inelastic scattering, in the linear optics regime a scattering equation for the dipole excitation β_j can be derived (see, e.g., Ref. [2])

$$\frac{d\beta_j}{dt} = \left[i(\Delta(\mathbf{r}_j) + \Delta_0) - \frac{\Gamma}{2}\right]\beta_j - \frac{i\Omega_0}{2}e^{i\mathbf{k}_0\cdot\mathbf{r}_j} - \frac{\Gamma}{2}\sum_{m\neq j}\frac{\exp(ik_0|\mathbf{r}_j - \mathbf{r}_m|)}{ik_0|\mathbf{r}_j - \mathbf{r}_m|}\beta_m, \quad (2)$$

where $\Gamma = V_\nu g_{k_0}^2 k_0^2/\pi c$ is the transition linewidth, and $|\beta_j|^2$ corresponds to the probability for atom j to be excited. Since the laser Δ_0 is equivalent to a magnetic field offset, under the assumption of a single excited state Zeeman level, we may set $\Delta_0 = 0$ without loss of generality.

As the lighthouse effect relies on a global phase contrast in the dipole field rather than on disorder effects, we adopt a fluid description of the system introducing the local density $\rho(\mathbf{r})$ and dipole field $\beta(\mathbf{r})$. Then, in the steady state regime, Eq. (2) turns into a Fredholm equation of the second type,

$$\beta(\mathbf{r}) = \beta^{(1)}(\mathbf{r}) + \int \mathrm{d}^3\mathbf{r}'\rho(\mathbf{r}')K(\mathbf{r},\mathbf{r}')\beta(\mathbf{r}'), \quad (3)$$

where we have introduced the single-scattering dipole excitation,

$$\beta^{(1)}(\mathbf{r}) = \frac{\Omega_0}{\Gamma}\frac{e^{i\mathbf{k}_0\cdot\mathbf{r}}}{i + 2\Delta(\mathbf{r})/\Gamma}, \quad (4)$$

and the scattering kernel,

$$K(\mathbf{r},\mathbf{r}') = \frac{1}{2i\Delta(\mathbf{r})/\Gamma - 1}\frac{e^{ik_0|\mathbf{r}-\mathbf{r}'|}}{ik_0|\mathbf{r}-\mathbf{r}'|}. \quad (5)$$

The consequence of a differential Zeeman effect is intuitive in the single-scattering limit Eq. (4), where the field $\Delta(\mathbf{r})$ modulates spatially the phase (and amplitude) of the dipole field, thus modifying the direction of superradiant emission of the cloud. In the multiple-scattering regime, a more detailed study must be performed in order to understand how the rescattering of the photons alters this new phase profile (see Section 4).

3. SINGLE-SCATTERING REGIME

For the sake of simplicity, we focus on a constant magnetic field gradient, which is orthogonal to the laser beam and cancels at the cloud's center: $B(\mathbf{r}) = \eta x$. We found the lighthouse effect to be strongest is this geometry. Indeed, for a central detuning $\Delta(\mathbf{r} = \mathbf{0})$ much larger than the one created by the gradient of the magnetic field bR (R the cloud radius), the resulting gradient of phase is tuned down by a factor $1/(1 + 4\Delta(\mathbf{0})^2/\Gamma^2)$, thus reducing the deflection angle.

We describe the cloud's density distribution by Gaussian spheres, which presents the analytical advantage of having a factorizable density in Cartesian coordinates:

$$\rho(x,y,z) = \frac{N}{(2\pi)^{3/2}R^3}e^{-\frac{x^2+y^2+z^2}{2R^2}}. \quad (6)$$

The far-field radiated electric field is given by

$$E(\mathbf{k}) = \frac{\hbar\Gamma}{id}\frac{e^{ik_0 r}}{r}\int \mathrm{d}^3\mathbf{r}'\rho(\mathbf{r}')\beta(\mathbf{r}')e^{-i\mathbf{k}\cdot\mathbf{r}'}, \quad (7)$$

where, for clarity, we have omitted the time-dependent oscillating term $e^{-ik_0 ct}$. The field resulting from single-scattering $E^{(1)}$ is then calculated by replacing the complete dipole excitation β in Eq. (7) by the single-scattering excitation $\beta^{(1)}$ [see Eq. (4)]. For a Gaussian cloud, introducing the normalized gradient $\alpha = 2\mu_B\eta/(\hbar k_0\Gamma)$ and the normalized cloud size $\sigma = k_0 R$, it reads (see Appendix A)

$$E^{(1)}(\mathbf{k}) = -\sqrt{\frac{\pi}{2}}\frac{NE_0}{|\alpha|\sigma}\frac{e^{ik_0 r}}{r}\exp\left(\frac{1}{2\alpha^2\sigma^2} + \frac{\sin\theta}{\alpha} - \frac{\sigma^2}{2}(1-\cos\theta)^2\right) \times \operatorname{erfc}\left(\frac{1}{|\alpha|\sigma\sqrt{2}} + \frac{\operatorname{sign}(\alpha)\sigma\sin\theta}{\sqrt{2}}\right), \quad (8)$$

with $\alpha \neq 0$, $\phi = 0$, and $0 \leq \theta \leq 2\pi$. As can be seen in Fig. 3, this formula describes very well the scattering process in the

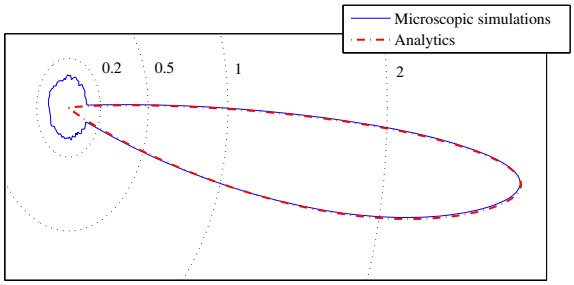

Fig. 2. Radiation pattern of light scattered ($|E|^2$) by an atom cloud under the influence of a differential Zeeman effect. Incident from the left, the light is deflected by a transverse magnetic field gradient. The analytical curve (red dashed) corresponds to Eq. (8), whereas the microscopic curve (blue solid) is obtained from simulations of the stationary solution of Eq. (2). The simulations are made for a cloud of $N = 100$ atoms with radius $\sigma = 35$ ($b_0 = 0.16$) and $\alpha = 1$. The microscopic simulations are averaged over 500 realizations. $|E|^2$ is in arbitrary unit, the dotted contour lines stand for its level.

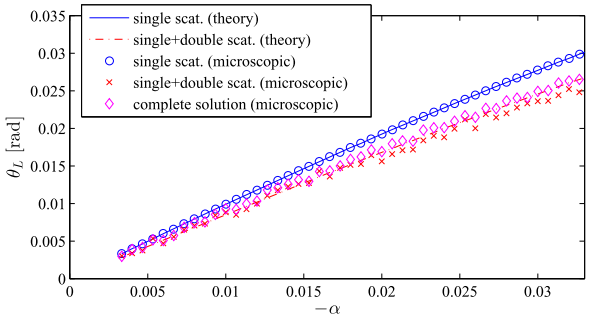

Fig. 3. Deflection angle θ_L as a function of the scaled magnetic field gradient α. The curves correspond respectively to single- (solid blue) and double-scattering (dashed red) contributions. The crosses, plus signs, and squares stand, respectively, for microscopic single-, double-, and full-scattering solutions. The simulations were realized for a cloud with radius $\sigma = 21$ ($b_0 = 0.5$) of $N = 113$ atoms, and averaged over 100 realizations.

single-scattering regime, i.e., for low optical thickness $b_0 = 2N/\sigma^2$. Let us remark that the normalized gradient α scales with the transition linewidth Γ, so different transitions may produce very different deviations.

The expansion in scattering orders is also investigated numerically, using Gaussian distributions $\{\mathbf{r}_i\}$ for direct simulations of the microscopic problem. Then, the single-scattering contribution is obtained by considering the single-scattering dipole excitation $\beta_j^{(1)} = (\Omega_0/\Gamma)/(i + 2\Delta(\mathbf{r}_j)/\Gamma)$, from which the radiated field is derived. The following scattering order is obtained as $\beta_j^{(2)} = \sum_m \mathbf{K}_{jm}\beta_m^{(1)}$, where the scattering matrix $\mathbf{K}$ has components $\mathbf{K}_{jm} = K(\mathbf{r}_j, \mathbf{r}_m)$ for $j \neq m$ and $\mathbf{K}_{jj} = 0$. Each higher scattering order is obtained by applying K on the previous one.

An illustration of Eq. (8) exhibiting the lighthouse effect is shown in Fig. 2. It clearly demonstrates how the transverse phase gradient deflects the incoming light. Furthermore, Eq. (8) appears to be in excellent agreement with numerical simulations of the microscopic problem of Eq. (2) realized in a regime where the cloud is optically thin ($b_0 = 0.16$). Indeed, the only difference between the two radiation patterns is an (apart from some noise) isotropic background present in the microscopic simulations. This background has its origin in the atomic disorder, which is naturally absent from our analytical approach.

The deflection angle θ_L is obtained by maximizing Eq. (8) over θ, which leads to

$$\frac{1}{\alpha} - \sigma\sqrt{\frac{2}{\pi}}\frac{\exp\left[-\frac{1}{2}\left(\frac{1}{|\alpha|\sigma} + \mathrm{sign}(\alpha)\sigma\sin\theta_L\right)^2\right]}{\mathrm{erfc}\left(\frac{1}{\sqrt{2}}\left(\frac{1}{|\alpha|\sigma} + \mathrm{sign}(\alpha)\sigma\sin\theta_L\right)\right)} = \sigma^2\tan\theta_L(1-\cos\theta_L). \quad (9)$$

Figure 3 compares the calculated deflection angle to microscopic simulations of Eq. (2), confirming the validity of the above formula. Under the approximation of a small total detuning over the cloud ($\alpha\sigma \ll 1$), we get

$$\theta_L = \sin^{-1}\left(\frac{1-\sqrt{1+4\alpha^2\sigma^2}}{2\alpha\sigma^2}\right) \approx -\alpha. \quad (10)$$

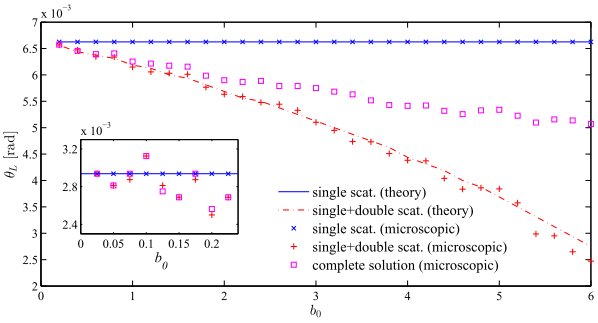

Fig. 4. Deflection angle θ_L as a function of the optical thickness b_0. The curves correspond respectively to single- (solid blue) and double-scattering (dashed red) contributions. The crosses, plus signs, and squares stand for, respectively, microscopic single-, double-, and full-scattering solutions. Simulations realized for a cloud of radius $\sigma = 21$, varying the number of particles N according to $b_0 = 2N/\sigma^2$, and averaged over 100 realizations. The inset shows the convergence to the single-scattering prediction for vanishing b_0. The latter simulations were realized for a system size $\sigma = 57$, in order to get sufficient a particle number at low optical thickness.

In the other limit of large α, note that the deviation angle is not limited by the diffraction limit from the cloud size. Indeed, an increasing gradient of the magnetic field means that only a smaller volume of atoms scatter the light efficiently, thus reducing the effective size of the macroscopic scatterer (see Fig. 7).

Yet, as one increases the optical thickness of the cloud (see Fig. 4), the single-scattering prediction loses its accuracy, pointing to the fact that the optically dense regime is ruled by photon rescattering. While an exact solution of the three-dimensional scattering problem including interference does not, to the best of our knowledge, exist, it is possible to probe the dense regime using, for example, a multiple-scattering expansion [19–22]. As we will see now, the double-scattering contribution can be evaluated, providing valuable hints of the dense regime.

4. MULTIPLE-SCATTERING REGIME

An analytical treatment of the multiple-scattering regime involves solving the problem of N fully coupled atom dipoles

[23–25]. Mean-field approaches such as the timed Dicke state [26] (TDS), or random walk approaches neglecting phase coherences, obviously cannot capture the modification of the atomic phase field. We thus resort to a multiple-scattering expansion, an approach that has proved particularly useful in the treatment of, e.g., coherent backscattering [20,27–29].

The double-scattering contribution to the field is obtained in Appendix A as

$$E^{(2)}(\theta) = NE_0 \frac{\sqrt{\pi} e^{1/(4\alpha^2\sigma^2)+\sin\theta/(2\alpha)-\sigma^2(1-\cos\theta)^2/4}}{16|\alpha|\sigma} \frac{e^{ik_0 r}}{r} \times \operatorname{erfc}\left(\frac{1}{2|\alpha|\sigma} + \frac{\operatorname{sign}(\alpha)\sigma\sin\theta}{2}\right) \times \frac{b_0}{\cos\frac{\theta}{2}} [e^{-\sigma^2(1+\sin\theta)^2} \operatorname{erfc}(-i\sigma(1+\sin\theta)) - e^{-\sigma^2(1-\sin\theta)^2} \operatorname{erfc}(-i\sigma(1-\sin\theta))]. \quad (11)$$

In Eq. (11), the first line describes the light deviation, while the second line yields the double-scattering process: the prefactor containing the optical thickness is typical for such an expansion. The validity of this expansion is delimited by the condition $b_0 < 1$, when single- and double-scattering are the dominant contributions.

In Fig. 5, the first-, second-, and complete-scattering solutions for the microscopic problem are plotted and compared to the analytical solution. The single- and double-scattering contributions are correctly predicted by the theory. Furthermore, the figure shows a reduction in the deflection angle as the optical thickness increases. Thus, the rescattering of the light by the atoms tends to erase the dipole phase gradient imposed by the magnetic field.

We note that the single- and double-scattering fields interfere destructively, since their electric fields have opposite signs. Thus, a careful treatment of the light field amplitude rather than the intensity is crucial, as already noted in [22].

As the optical thickness increases beyond unity, the numerical full-scattering solution, which contains all scattering orders, deviates from the prediction obtained for double-scattering. This is confirmed by the analysis performed in Fig. 4, where the deviation angle appears correctly predicted by the single-scattering approach for $b_0 \ll 1$ and by the double-scattering calculations for $b_0 \leq 1$. The extremum equation for the deflection angle θ_L including double-scattering is straightforwardly derived from Eq. (11), yet cumbersome, for which reason it is not presented here.

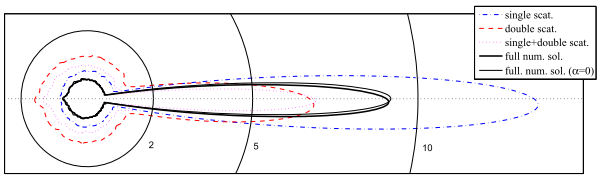

Fig. 5. Radiation pattern $|E|^2$ for different scattering orders (see legend), for the microscopic system. The solid thick and thin lines correspond respectively to the numerical full-scattering solution with and without the gradient of the magnetic field. Simulations realized for a cloud of $N = 225$ atoms, $\sigma = 21$ ($b_0 = 1$), and $\alpha = 0.013$, and averaged over 500 configurations. $|E|^2$ is in arbitrary units, the solid contour lines stand for its level.

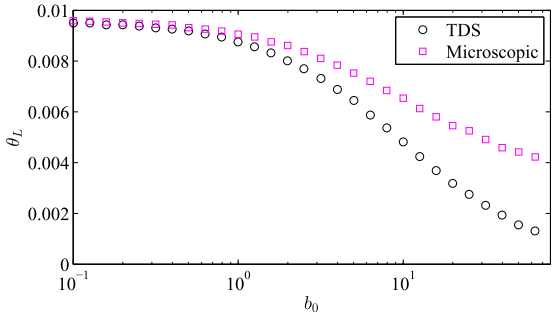

Fig. 6. Deviation angle for optically thick samples. Simulations realized for a cloud of size $\sigma = 21$, the number of particles being determined by the optical thickness, and $\alpha = -0.01$. The timed Dicke state (TDS) symbols refer to single-scattering calculations using the collective linewidth.

Features of the deep multiple-scattering regime can be captured using a modified timed Dicke state: this mean-field ansatz assumes a perfect synchronization of all atomic dipoles [26] and, as a consequence, a broadening of the atomic linewidth. For a Gaussian cloud, the collective linewidth is $\Gamma_N = \Gamma(1 + b_0/8)$ [30]. In our case, we also need to account for an effective reduction in the optical thickness due to the inhomogeneous detuning imposed by the gradient of the magnetic field. The average detuning of the atoms compared to those on the optical axis being $\delta_{\mathrm{LH}} = \alpha\sigma$, the effective optical thickness for the cloud is $b^{\mathrm{eff}} = b_0/(1 + 4\delta_{\mathrm{LH}}^2)$.

Replacing the atomic linewidth by the collective one $\Gamma(1 + b^{\mathrm{eff}}/8)$ in the single-scattering prediction, we predict a reduction in the lighthouse effect as the optical density increases: the increase in linewidth leads to a decrease in the normalized gradient α. Simulations of the microscopic problem confirm that result and show a qualitative agreement with the prediction of the modified timed Dicke ansatz (see Fig. 6).

5. DISCUSSION AND EXPERIMENTAL PERSPECTIVES

We investigated the deflection of light by an atomic cloud under the influence of a differential Zeeman shift and found that the single-scattering regime yields maximum deflection. Calculations and simulations for clouds of larger optical density, which are dominated by multiple scattering, revealed a reduction in the effect. This observation points to the fact that the lighthouse deflection is clearly not a cooperative effect in the sense that it does not result from light-mediated interaction of the atoms. It is rather similar to Bragg scattering, where the scattering pattern generated by the interference of the radiated waves provides information about the atomic cloud's structure. As soon as the atoms interact through their radiation, the emergence of multiple scattering washes out the phase gradient imposed externally by the magnetic field.

Our predictions can be experimentally verified, e.g., with a cloud of spatially confined cold atoms exposed to a uniform magnetic field gradient. Measurable deflections are expected when the parameter α is not too small compared to 1. According to the definition of α [below Eq. (7)], for a typical magnetic field gradient of $\eta = 100$ G/cm, this requires rather small linewidths of the atomic transition. A possible system would be a cloud of ultracold strontium driven on its intercombination line at $\lambda = 2\pi/k = 689$ nm. The transition linewidth being

$\Gamma = (2\pi)7.6$ kHz one could reach $\alpha = 0.8$ with the specified gradient.

In our derivations we assumed a single excited state Zeeman level. However, if the atomic cloud is trapped in a magneto-optical trap (MOT) we would rather have a distribution of atoms in all Zeeman levels. Furthermore, the magnetic field does not have the geometry of a uniform gradient but of a quadrupolar field. These problems, can, however, be circumvented by suddenly applying a magnetic field offset B_0 and simultaneously detuning the probe light beam to the Zeeman-shifted resonance. In that way, one spectrally filters out a single Zeeman state, i.e., the probe light predominantly interacts with atoms occupying a single Zeeman level. This requires $B_0 \gg \Gamma$, which is easy to satisfy in the case of a narrow linewidth Γ.

Typical values for a strontium MOT operated on the narrow intercombination line are an atom number of $N = 2 \cdot 10^7$ and a radial size of $\bar{R} = 70$ μm (or $\sigma = k\bar{R} \simeq 640$) [31], giving an optical density of $b_0 = 2N/(k\bar{R})^2 \simeq 100$ for the intercombination line. In practice, however, narrow transitions are generally dominated by Doppler broadening. At a temperature of 4 μK, for example, the Doppler broadening of the intercombination line is $k\bar{v} = k\sqrt{k_B T/m} = (2\pi)$ 28 kHz. Even if the temperature is at the Doppler limit of the intercombination line, $T_D = \hbar\Gamma/k_B = 365$ nK, the Doppler width still is 8.5 kHz.

To prevent blurring of the lighthouse deflection by the thermal atomic motion, it is important that the Doppler shift be smaller than the Zeeman shift, $k\bar{v} \ll \bar{R}\partial_r B$. In this case, the main effect of the thermal motion is to reduce the optical thickness of the atomic cloud, by a factor corresponding to the spectral overlap between the natural linewidth and the Doppler broadened width, $b_D = b_0\Gamma/kv$.

Another point ruling the detectability of the lighthouse deflection is, whether it exceeds the probe beam divergence angle. Assuming that it is optimally matched to the size of the cloud, $w_0 = \bar{R} = 70$ μm, we obtain the divergence angle $\alpha_{\text{div}} = \lambda/\pi w_0 = 0.18°$. Since $\sigma = 70$ μm/689 nm ≈ 101 and $\alpha \approx 0.4$, the deflection angle predicted by Eq. (9) is $\theta_L = 1.34°$, so that the deviated beam is easily separated from the incident laser (see Fig. 7).

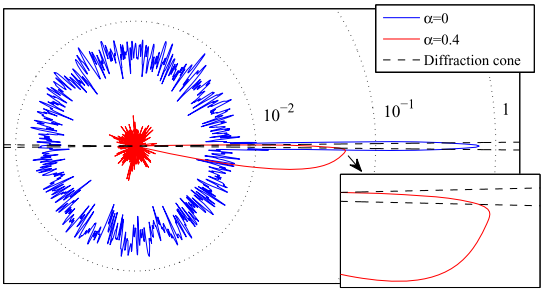

Fig. 7. Radiation pattern normalized by the incident intensity $|E/E_0|^2$ for the microscopic system, with (thick red) and without (thin blue) the gradient of the magnetic field. The inset allows us to observe that the lighthouse angle is not diffraction-limited (cone of black dashed lines; see main text). Note that the strong background radiation is due to the limited number of particles that can be simulated. The reduced radiated intensity in the presence of the gradient of the magnetic field is due to the fact that many atoms are driven out of resonance by it, so their coupling with the light is reduced. Simulations realized for a cloud of $N = 15000$ atoms, $\sigma = 101$ ($b_0 = 2.94$) and $\alpha = 0.4$, and averaged over 10 configurations. $|E|^2$ is in arbitrary units, the dotted contour lines stand for its level.

Even on regular MOTs operating on strong transitions, the atomic lighthouse effect should be detectable. Considering, for instance, the broad $^1S_0 - {}^1P_1$ transition in strontium [$\Gamma = (2\pi)32$ MHz], we estimate a deflection angle of $\theta_L = 0.026°$, which is of the same order of magnitude as the divergence angle, which for a MOT radius of typically $\bar{R} = 3$ mm, would be $\alpha_{\text{div}} = 0.028°$.

The experimental verification of the lighthouse effect would represent a nice confirmation that our actual understanding of how light is cooperatively scattered by ensembles of particles is correct, as the reduction in the deviation angle provides a direct measure of the collective atomic linewidth.

APPENDIX A: SINGLE- AND DOUBLE-SCATTERING STRUCTURE FACTOR

In the far-field limit and at a distance r, the single-scattering field is given by

$$E^{(1)}(\mathbf{k}) = -\frac{NE_0}{(2\pi)^{\frac{3}{2}}R^3}\frac{e^{ik_0 r}}{r}\int_{-\infty}^{\infty} e^{i(1-\cos\theta)k_0 z}e^{-z^2/2R^2}\,\mathrm{d}z \times \int_{-\infty}^{\infty} e^{-ik_0 y\,\sin\theta\,\sin\phi}e^{-y^2/2R^2}\,\mathrm{d}y \times \int_{-\infty}^{\infty}\frac{e^{-ik_0 x\,\sin\theta\,\cos\phi}e^{-x^2/2R^2}}{1-i\alpha k_0 x}\,\mathrm{d}x.$$

The first integral gives $\exp(-(1-\cos\theta)^2\sigma^2/2)$ that yields the forward emission of Rayleigh scattering, in a cone of width $\sim 1/\sigma$. The second integral produces a $\exp(-\sin^2\theta\sin^2\phi\sigma^2/2)$, yet since the problem is symmetric with respect to the $(\hat{x},\hat{z})$ plane, we restrict ourselves to this plane, taking $\phi = 0, \pi$. Finally, the integral over x, that contains the deviation is

$$\int_{-\infty}^{\infty}\frac{e^{\pm ik_0 x\sin\theta}e^{-x^2/2R^2}}{1-i\alpha k_0 x}\mathrm{d}x = \gamma^2\int_{-\infty}^{\infty}e^{-x^2/2R^2}\cos ax\frac{\mathrm{d}x}{\gamma^2+x^2} \pm \mathrm{sign}(\gamma)|\gamma|\int_{-\infty}^{\infty}e^{-x^2/2R^2}\sin ax\frac{x\mathrm{d}x}{\gamma^2+x^2},$$

with $a = k_0\,\sin\theta$ and $\gamma = 1/\alpha k_0$, and where the $\pm$ signs refer to the cases $\phi = 0, \pi$. Both integrals are solved using integral formula [32]

$$\int_{-\infty}^{\infty}e^{-x^2/2R^2}\sin ax\frac{x\mathrm{d}x}{\gamma^2+x^2} = -\frac{\pi}{2}e^{\gamma^2/2R^2}\left[e^{a|\gamma|}\,\mathrm{erfc}\left(\frac{1}{\sqrt{2}}\left(\frac{|\gamma|}{R}+aR\right)\right) - e^{-a|\gamma|}\,\mathrm{erfc}\left(\frac{1}{\sqrt{2}}\left(\frac{|\gamma|}{R}-aR\right)\right)\right], \quad \text{(A1)}$$

$$\int_{-\infty}^{\infty}e^{-x^2/2R^2}\cos ax\frac{\mathrm{d}x}{\gamma^2+x^2} = \frac{\pi}{2|\gamma|}e^{\gamma^2/2R^2}\left[e^{-a|\gamma|}\,\mathrm{erfc}\left(\frac{1}{\sqrt{2}}\left(\frac{|\gamma|}{R}-aR\right)\right) + e^{a|\gamma|}\,\mathrm{erfc}\left(\frac{1}{\sqrt{2}}\left(\frac{|\gamma|}{R}+aR\right)\right)\right]. \quad \text{(A2)}$$

Consequently, we have

$$\int_{-\infty}^{\infty} \frac{e^{\pm i \sin\theta k_0 x} e^{-x^2/2R^2}}{1 - i\alpha k_0 x} \mathrm{d}x = \pi|\gamma| e^{\frac{\gamma^2}{2R^2}} e^{\pm \mathrm{sign}(\gamma) a|\gamma|} \times \mathrm{Erfc}\left[\frac{1}{\sqrt{2}}\left(\frac{|\gamma|}{R_x} \pm \mathrm{sign}(\gamma) a R_x\right)\right].$$

This leads to Eq. (8), since the $\pm$ can be replaced by $+$ by extending the angle range to interval $0 \le \theta \le 2\pi$.

The double-scattering field is given by the expression

$$E^{(2)}(\mathbf{k}) = \frac{\hbar\Gamma}{id} \frac{e^{ik_0 r}}{r} \int \mathrm{d}^3\mathbf{r} \rho(\mathbf{r}) e^{-i\mathbf{k}\cdot\mathbf{r}} \int \mathrm{d}^3\mathbf{r}' \rho(\mathbf{r}') K(\mathbf{r}, \mathbf{r}') \beta^{(1)}(\mathbf{r}'). \tag{A3}$$

These integrals can be decoupled for a Gaussian density distribution, using the following change of variables

$$\mathbf{u} = \frac{\mathbf{r} - \mathbf{r}'}{\sqrt{2}}, \qquad \mathbf{w} = \frac{\mathbf{r} + \mathbf{r}'}{\sqrt{2}}, \tag{A4}$$

so that $\rho(\mathbf{r})\rho(\mathbf{r}') = \rho(\mathbf{u})\rho(\mathbf{w})$, and assuming that the quadratic terms in u^2 and v^2 can be neglected in the Zeeman term (approximation of small frequency shift $2\alpha^2\sigma^2 \ll 1$). Then we obtain

$$E^{(2)}(\mathbf{k}) = E_0 \frac{e^{ik_0 r}}{r} \int \mathrm{d}^3\mathbf{u} \rho(u) \frac{e^{i\sqrt{2}u}}{i\sqrt{2}u} e^{-i\mathbf{u}\cdot(\mathbf{k}_0 + \mathbf{k})/\sqrt{2}} \times \int \frac{\mathrm{d}^3\mathbf{w} \rho(w) e^{i\mathbf{w}\cdot(\mathbf{k}_0 - \mathbf{k})/\sqrt{2}}}{1 + i\sqrt{2}\alpha \mathbf{w}\cdot\hat{x}}. \tag{A5}$$

Similar to the single-scattering case, the second integral I_w in Eq. (A5) leads to

$$I_w(\theta) = \frac{\sqrt{\pi}}{2} \frac{N}{|\alpha|\sigma} \exp\left(\frac{1}{4\alpha^2\sigma^2} + \frac{\mathrm{sign}(\alpha)\sin\theta}{2|\alpha|} - \frac{\sigma^2}{4}(1 - \cos\theta)^2\right) \times \mathrm{erfc}\left(\frac{1}{2}\left(\frac{1}{|\alpha|\sigma} + \mathrm{sign}(\alpha)\sigma \sin\theta\right)\right). \tag{A6}$$

The first integral, I_u, in Eq. (A5) is calculated using spherical coordinates (u, θ_u, ϕ_u). The integral over ϕ_u leads to

$$\begin{aligned} I_u(\theta) &= \frac{N}{i2\sqrt{\pi}k_0 R^3} \int_0^\infty u e^{-u^2/2R^2 + i\sqrt{2}k_0 u} \mathrm{d}u \int_0^\pi \\ &\quad \times \sin\theta_u e^{-i\frac{k_0 u}{\sqrt{2}}(1+\cos\theta)\cos\theta_u} J_0\left(\frac{k_0 u \sin\theta \sin\theta_u}{\sqrt{2}}\right) \mathrm{d}\theta_u \\ &= \frac{N}{i\sqrt{2\pi}k_0^2 R^3 \cos\frac{\theta}{2}} \int_0^\infty e^{-u^2/2R^2 + i\sqrt{2}k_0 u} \sin\left(\sqrt{2}k_0 u \cos\frac{\theta}{2}\right) \mathrm{d}u \\ &= -\frac{b_0}{8\cos\frac{\theta}{2}} \left[\exp\left(-\sigma^2\left(1 + \cos\frac{\theta}{2}\right)^2\right) \right. \\ &\quad \times \mathrm{erfc}\left(-i\sigma\left(1 + \cos\frac{\theta}{2}\right)\right) - \exp\left(-\sigma^2\left(1 - \cos\frac{\theta}{2}\right)^2\right) \\ &\quad \left. \times \mathrm{erfc}\left(-i\sigma\left(1 - \cos\frac{\theta}{2}\right)\right)\right], \end{aligned} \tag{A7}$$

where we have introduced the optical thickness $b_0 = 2N/\sigma^2$.

ACKNOWLEDGMENTS

We acknowledge financial support from IRSES project COSCALI, from USP/COFECUB (projet Uc Ph 123/11), and from GDRI "Nanomagnetism, Spin Electronics, Quantum Optics, and Quantum Technologies." C. E. M., Ph. W. C., and R. B. acknowledge support from the Brazilian FAPESP and CNPq agencies.

REFERENCES

1. R. H. Dicke, "Coherence in spontaneous radiation processes," Phys. Rev. **93**, 99–110 (1954).
2. R. Friedberg, S. R. Hartmann, and J. T. Manassah, "Frequency shifts in emission and absorption by resonant systems of two-level Atoms," Phys. Rep. C **7**, 101179 (1973).
3. R. Röhlsberger, K. Schlage, B. Sahoo, S. Couet, and R. Rüffer, "Collective lamb shift in single-photon superradiance," Science **328**, 1248–1251 (2010).
4. J. Keaveney, A. Sargsyan, U. Krohn, I. G. Hughes, D. Sarkisyan, and C. S. Adams, "Cooperative lamb shift in an atomic vapor layer of nanometer thickness," Phys. Rev. Lett. **108**, 173601 (2012).
5. I. H. Deutsch, R. J. C. Spreeuw, S. L. Rolston, and W. D. Phillips, "Photonic band gaps in optical lattices," Phys. Rev. A **52**, 1394–1410 (1995).
6. M. Antezza and Y. Castin, "Fano–Hopeld model and photonic band gaps for an arbitrary atomic lattice," Phys. Rev. A **80**, 013816 (2009).
7. A. Schilke, C. Zimmermann, P. Courteille, and W. Guerin, "Photonic band gaps in one-dimensionally ordered cold atomic vapors," Phys. Rev. Lett. **106**, 223903 (2011).
8. M. Antezza and Y. Castin, "Photonic band gap in an imperfect atomic diamond lattice: penetration depth and effects of finite size and vacancies," Phys. Rev. A **88**, 033844 (2013).
9. M. Samoylova, N. Piovella, R. Bachelard, and P. Courteille, "Microscopic theory of photonic bandgaps in optical lattices," Opt. Commun. **312**, 94–98 (2014).
10. R. Röhlsberger, T. S. Toellner, W. Sturhahn, K. Quast, E. E. Alp, A. Bernhard, E. Burkel, O. Leupold, and E. Gerdau, "Coherent resonant x-ray scattering from a rotating medium," Phys. Rev. Lett. **84**, 1007–1010 (2000).
11. R. Röhlsberger, T. Toellner, K. Quast, W. Sturhahn, E. Alp, and E. Burkel, "The nuclear lighthouse effect: a new tool for high-resolution X-ray spectroscopy," Nucl. Instrum. Methods Phys. Res. Sect. A **467–468**, 1473–1476 (2001).
12. R. Röhlsberger, K. Quast, T. S. Toellner, P. L. Lee, W. Sturhahn, E. E. Alp, and E. Burkel, "Observation of the 22.5-keV resonance in (149)Sm by the nuclear lighthouse effect," Phys. Rev. Lett. **87**, 047601 (2001).
13. T. Roth, O. Leupold, H.-C. Wille, R. Rüffer, K. W. Quast, R. Röhlsberger, and E. Burkel, "Coherent nuclear resonant scattering by (61)Ni using the nuclear lighthouse effect," Phys. Rev. B **71**, 140401(R) (2005).
14. L. Karpa and M. Weitz, "A Stern–Gerlach experiment for slow light," Nat. Phys. **2**, 332–335 (2006).
15. L. Karpa and M. Weitz, "Nondispersive optics using storage of light," Phys. Rev. A **81**, 041802 (2010).
16. U. Schnorrberger, J. D. Thompson, S. Trotzky, R. Pugatch, N. Davidson, S. Kuhr, and I. Bloch, "Electromagnetically induced transparency and light storage in an atomic Mott insulator," Phys. Rev. Lett. **103**, 033003 (2009).
17. V. A. Sautenkov, H. Li, Y. V. Rostovtsev, and M. O. Scully, "Ultra-dispersive adaptive prism based on a coherently prepared atomic medium," Phys. Rev. A **81**, 063824 (2010).
18. T. Bienaime, M. Petruzzo, D. Bigerni, N. Piovella, and R. Kaiser, "Atom and photon measurement in cooperative scattering by cold atoms," J. Mod. Opt. **58**, 1942–1950 (2011).
19. A. Ishimaru, *Wave Propagation and Scattering in Random Media* (Academic, 1978), Vol **2**.
20. M. B. van der Mark, M. P. van Albada, and A. Lagendijk, "Light scattering in strongly scattering media: multiple scattering and weak localization," Phys. Rev. B **37**, 3575–3592 (1988).

21. T. M. Nieuwenhuizen, A. Lagendijk, and B. A. van Tiggelen, "Resonant point scatterers in multiple scattering of classical waves," Phys. Lett. A **169**, 191–194 (1992).
22. M.-T. Rouabah, M. Samoylova, R. Bachelard, P. W. Courteille, R. Kaiser, and N. Piovella, "Coherence effects in scattering order expansion of light by atomic clouds," J. Opt. Soc. Am. A **31**, 1031–1039 (2014).
23. M. Chalony, R. Pierrat, D. Delande, and D. Wilkowski, "Coherent flash of light emitted by a cold atomic cloud," Phys. Rev. A **84**, 011401R (2011).
24. S. E. Skipetrov and I. M. Sokolov, "Absence of Anderson localization of light in a random ensemble of point scatterers," Phys. Rev. Lett. **112**, 023905 (2014).
25. J. Pellegrino, R. Bourgain, S. Jennewein, Y. R. P. Sortais, S. D. Jenkins, J. Ruostekoski, and A. Browaeys, "Observation of suppression of light scattering induced by dipole-dipole interactions in a cold atomic ensemble," arXiv:1402.4167 (2014).
26. M. Scully, E. Fry, C. Ooi, and K. Wodkiewicz, "Directed spontaneous emission from an extended ensemble of N atoms: timing is everything," Phys. Rev. Lett. **96**, 010501 (2006).
27. E. Akkermans, P. E. Wolf, and R. Maynard, "Coherent backscattering of light by disordered media: analysis of the peak line shape," Phys. Rev. Lett. **56**, 1471–1474 (1986).
28. P.-E. Wolf and G. Maret, "Weak localization and coherent backscattering of photons in disordered media," Phys. Rev. Lett. **55**, 2696 (1985).
29. M. P. V. Albada and A. Lagendijk, "Observation of weak localization of light in a random medium," Phys. Rev. Lett. **55**, 2692–2699 (1985).
30. P. W. Courteille, S. Bux, E. Lucioni, K. Lauber, T. Bienaim, R. Kaiser, and N. Piovella, "Modification of radiation pressure due to cooperative scattering of light," Eur. Phys. J. D **58**, 69–73 (2010).
31. T. Chanelière, D. Wilkowski, Y. Bidel, R. Kaiser, and C. Miniatura, "Saturation-induced coherence loss in coherent backscattering of light," Phys. Rev. E **70**, 036602 (2004).
32. I. S. Gradshteyn and I. M. Ryzhik, *Table of Integrals, Series, and Products*, 7th ed. (Elsevier/Academic, 2007).

3.2 Spatial and temporal localization of light in two dimensions

PHYSICAL REVIEW A **92**, 062702 (2015)

Spatial and temporal localization of light in two dimensions

C. E. Máximo,[1] N. Piovella,[2] Ph. W. Courteille,[1] R. Kaiser,[3] and R. Bachelard[1,*]
[1]*Instituto de Física de São Carlos, Universidade de São Paulo, 13560-970 São Carlos, SP, Brazil*
[2]*Dipartimento di Fisica, Università degli Studi di Milano, Via Celoria 16, Milano I-20133, Italy*
[3]*Université de Nice Sophia Antipolis, CNRS, Institut Non-Linéaire de Nice, UMR 7335, F-06560 Valbonne, France*
(Received 24 August 2015; revised manuscript received 23 October 2015; published 1 December 2015)

Quasiresonant scattering of light in two dimensions can be described either as a scalar or as a vectorial electromagnetic wave. Performing a scaling analysis we observe in both cases long lived modes, yet only the scalar case exhibits Anderson localized modes together with extremely long mode lifetimes. We show that the localization length of these modes is influenced only by their position, and not their lifetime. Investigating the reasons for the absence of localization, it appears that both the coupling of several polarizations and the presence of near-field terms are able to prevent long lifetimes and Anderson localization.

DOI: 10.1103/PhysRevA.92.062702 PACS number(s): 42.25.Dd, 42.25.Fx, 42.25.Ja, 63.20.Pw

I. INTRODUCTION

Multiple scattering of waves has been the subject of intense debates in the context of disorder-induced Anderson localization [1]. Indeed, since the proposal to use electromagnetic waves in random media instead of electrons in solids exploiting the noninteracting properties of photons at low intensities [2], many experiments and theoretical studies have been performed. However, despite a decade-long research, the mere existence of Anderson localization of light [3–5] and its relation to another long predicted phenomenon, namely Dicke super- and subradiance [6], are still not clearly understood [7]. The advent of laser-cooled atoms and their use to study both localization and super- and subradiance motivated the development of *ab initio* models of interference effects in multiple scattering of light [8]. As most experiments are typically performed in a three-dimensional (3D) setting, models have also been focused on such 3D configurations. However, both numerical and fundamental aspects of localization strongly depend on the dimension of the explored system [9]. For this reason we have focused our efforts on a two-dimensional (2D) system, where a precise study of the eigenvalues and eigenmodes of the system is more efficient than in 3D, because larger "volumes" can be simulated for a given number of scatterers. One further advantage is that the reduced dimensionality allows for a direct comparison of eigenvalues and eigenvectors between two regimes of scattering, one of a scalar model of light, the other of a vectorial model of light where the wave polarization needs to be accounted for. This comparison recently revealed important differences observed for the eigenvalues of the relevant effective Hamiltonians [4,5,10].

In this work we investigate resonant scattering in a two-dimensional setup, i.e., the light scattering and propagation are confined to two dimensions. This configuration may be realized, e.g., with a disordered arrangement of scatterers in microwave cavities [11], in photonic crystals [12], near surface plasmons, or with laser-cooled atoms located in an off-resonance optical cavity. In this geometry, the polarization orthogonal to the plane, called s polarization, cannot couple through the scatterers to the planar (or p) polarizations, hence it is described by a scalar light model. The two p polarizations of the electromagnetic waves do couple, and this vectorial-like scattering includes near-field terms (see scheme in Fig. 1). Rotating the polarization of an incident wave allows us to switch between the scalar or vectorial regime, between the presence or the absence of polarization degrees of freedom and near-field terms, making it an ideal tool to investigate the role of polarization in localization and subradiance.

In Sec. II we present a detailed derivation of the linear differential equations that rule the population evolution of atomic transitions. The spectral properties of these equations are investigated in Sec. III, where scalar and vector scattering are compared via scaling analysis. Finally, we present our conclusions in Sec. IV highlighting uncorrelation between spatial and temporal localization of light.

II. MODEL

Two-dimensional light scattering was investigated in microwave cavities, where light with a polarization orthogonal to the plates approximately obeys the Helmholtz 2D scalar equation, and Anderson localization was observed [11]. Another possibility to emulate 2D light scattering is a cloud of cold atoms with no Doppler broadening located inside an off-resonant optical cavity made by two metallic disks whose diameter is much larger than their mutual distance. This system, which is closer to situations previously studied in 3D, constitutes the toy model system we will explore in this paper. Let us consider an homogeneous disk-shaped cloud of N motionless atoms sitting at randomly distributed positions $\mathbf{r}_j = (x_j, y_j, z_j)$ with $j = 1, \ldots, N$, for which nonradiative interactions are neglected. Instead, only virtual and real photons couple the atoms within the optical cavity (axis z) whose resonance frequency is significantly detuned from the atomic transition ω_a. The electric dipole transitions occur between one nondegenerate ground state $|g_j\rangle$, related to angular momentum $\ell = 0$ and a triply degenerate excited state $|e_j^m\rangle$, where $m = 0, \pm 1$ indicate the projections of the angular momentum $\ell = 1$ over the quantization axis z. We consider 2D scattering restricted to a radial direction in the (x, y) plane with a surface density of the atomic cloud $\rho = N/\pi R^2$, where R is the cloud radius.

*Corresponding author: bachelard.romain@gmail.com

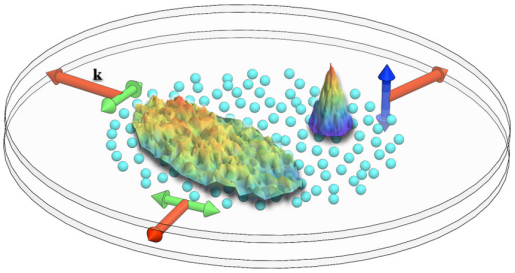

FIG. 1. (Color online) Two-dimensional scattering scheme: The radiation of wave number k close to the atomic transition $k_a = \omega_a/c \approx k$, is confined in the (x,y) plane, i.e., it has wave vectors of the form $\mathbf{k} = k(\cos\theta, \sin\theta, 0)$. Two eigenvectors are shown: a localized s-polarized mode in the upper right part and a extended p-polarized mode in the left part.

The interaction of the atoms with the radiation field is given by the following Hamiltonian:

$$\hat{H} = \frac{\hbar\omega_a}{2}\sum_{j=1}^{N}\hat{\sigma}_{z,j} + \hbar\sum_{\mathbf{k},s}\omega_{\mathbf{k}}\left(\hat{a}^{\dagger}_{\mathbf{k},s}\hat{a}_{\mathbf{k},s} + \frac{1}{2}\right) + \hbar\sum_{j=1}^{N}\sum_{m=-1}^{1}\sum_{\mathbf{k},s}(\hat{a}^{\dagger}_{\mathbf{k},s}e^{-i\mathbf{k}\cdot\mathbf{r}_j} + \hat{a}_{\mathbf{k},s}e^{i\mathbf{k}\cdot\mathbf{r}_j}) \times \left(g^{j,m}_{\mathbf{k},s}\hat{\sigma}^{(m)}_{j} + g^{j,m*}_{\mathbf{k},s}\hat{\sigma}^{\dagger(m)}_{j}\right), \tag{1}$$

with ω_a as the atomic transition frequency and $\hat{\sigma}_{z,j}$ as the atomic diagonal term, whereas $\hat{\sigma}^{(m)}_{j} = |g_j\rangle\langle e_{j,m}|$ and $\hat{\sigma}^{\dagger(m)}_{j} = |e_{j,m}\rangle\langle g_j|$ are the lowering and lifting atomic operators. $\hat{a}^{\dagger}_{\mathbf{k},s}$ and $\hat{a}_{\mathbf{k},s}$ refer to the creation and annihilation of a photon for mode $\mathbf{k}$, with frequency $\omega_{\mathbf{k}}$. The coupling coefficient reads $g^{j,m}_{\mathbf{k},s} = \hat{\mathbf{e}}_{\mathbf{k},s}\cdot\mathbf{d}_{j,m}\sqrt{\omega_{\mathbf{k}}/2\hbar\epsilon_0 V}$, with V as the quantization volume and $\mathbf{d}_{j,m} = \langle g_j|e\mathbf{r}_j|e_{j,m}\rangle$ as the dipole matrix element (with e as the electron charge). Thus, the two first terms in (1) are the free-energy contribution and the last term corresponds to the interaction with the vacuum modes.

We then use the commutation relations

$$\left[\hat{\sigma}^{\dagger(m)}_{j},\hat{\sigma}^{(m')}_{j'}\right] \approx -\mathbb{1}^{m'}_{j'}\delta_{j,j'}\delta_{m,m'}, \tag{2a}$$

$$[\hat{a}_{\mathbf{k},s},\hat{a}^{\dagger}_{\mathbf{k}',s'}] = \delta_{s,s'}\delta_{\mathbf{k},\mathbf{k}'}, \tag{2b}$$

$$\left[\hat{\sigma}^{(m)}_{j},\hat{\sigma}^{(m')}_{z,j'}\right] = 2\hat{\sigma}^{(m')}_{j'}\delta_{j,j'}\delta_{m,m'}, \tag{2c}$$

where the approximation in the first of these equations correspond to the linear optics regime $|e_{j,m}\rangle\langle e_{j,m}| - |g_j\rangle\langle g_j| \approx -\mathbb{1}^{m}_{j}$ (we eliminate the possibility of multiexcitation in the system), to obtain the Heisenberg equations for the operators:

$$\frac{d\hat{\sigma}^{(m)}_{j}}{dt} + i\omega_a\hat{\sigma}^{(m)}_{j} = -i\sum_{\mathbf{k},s}g^{j,m*}_{\mathbf{k},s}(\hat{a}_{\mathbf{k},s}e^{i\mathbf{k}\cdot\mathbf{r}_j} + \hat{a}^{\dagger}_{\mathbf{k},s}e^{-i\mathbf{k}\cdot\mathbf{r}_j}), \tag{3a}$$

$$\frac{d\hat{a}_{\mathbf{k},s}}{dt} + i\omega_{\mathbf{k}}\hat{a}_{\mathbf{k},s} = -i\sum_{j=1}^{N}\sum_{m=-1}^{1}\left(g^{j,m}_{\mathbf{k},s}\hat{\sigma}^{(m)}_{j} + g^{j,m*}_{\mathbf{k},s}\hat{\sigma}^{\dagger(m)}_{j}\right) \times e^{-i\mathbf{k}\cdot\mathbf{r}_j}. \tag{3b}$$

Equations (3a) and (3b) show a correlated dynamics between atomic levels and vacuum modes.

The radiation field plays the role of a reservoir for atoms and is composed of an infinite number of degrees of freedom $\mathbf{k},s$, so it is convenient to trace over these. Using the unitary transformations $\hat{\sigma}^{(m)}_{j} \to \hat{\sigma}^{(m)}_{j}e^{i\omega_a t}$ and $\hat{a}_{\mathbf{k},s} \to \hat{a}_{\mathbf{k},s}e^{i\omega_{\mathbf{k}}t}$, we obtain the reduced equation evolution for the atomic open system

$$\frac{d\hat{\sigma}^{(m)}_{j}}{dt} = -\sum_{l,n}\sum_{\mathbf{k},s}g^{j,m*}_{\mathbf{k},s}\int_0^t d\tau\left[g^{l,n}_{\mathbf{k},s}\hat{\sigma}^{(n)}_{l}(t-\tau)e^{i\omega_a\tau} + g^{l,n*}_{\mathbf{k},s}\hat{\sigma}^{\dagger(n)}_{l}(t-\tau)e^{i\omega_a(2t-\tau)}\right] \times (e^{i\omega_{\mathbf{k}}\tau + i\mathbf{k}\cdot\mathbf{r}_{jl}} - \text{c.c.}). \tag{4}$$

We can apply the rotating wave approximation and neglect the fast oscillating terms proportional to $e^{2i\omega_a t}$. Assuming that the photon transit time inside the atomic cloud is much shorter than the emission decay time, we can perform the Markov approximation $\hat{\sigma}^{(n)}_{l}(t-\tau) \approx \hat{\sigma}^{(n)}_{l}(t)$ so the atomic transitions evolves according to the closed set of equations

$$\frac{d\hat{\sigma}^{(m)}_{j}}{dt} = -\frac{1}{2}\sum_{n=-1}^{1}\sum_{l=1}^{N}K_{m,n}(\mathbf{r}_{jl})\hat{\sigma}^{(n)}_{l}, \tag{5}$$

where the scattering kernel is defined as

$$K_{m,n}(\mathbf{r}_{jl}) \equiv 2\int_0^{\infty}d\tau e^{i\omega_a\tau}\sum_{\mathbf{k},s}g^{j,m*}_{\mathbf{k},s}g^{l,n}_{\mathbf{k},s}(e^{-i\omega_{\mathbf{k}}\tau + i\mathbf{k}\cdot\mathbf{r}_{jl}} - \text{c.c.}), \tag{6}$$

with $\mathbf{r}_{jl} = \mathbf{r}_j - \mathbf{r}_l$, and where the upper limit in the above integral has been extrapolated to $t \to \infty$ according to the Markov approximation. The spontaneous emission processes are naturally three dimensional and the above scattering kernel *a priori* contains all light modes in 3D space, so all transitions may be coupled. Under the assumption of an effective two-dimensional scattering of light, we can perform in the continuous 3D density of modes the following approximation:

$$\sum_{\mathbf{k}} \to \frac{V}{(2\pi)^3}\int d^3\mathbf{k}\delta(\theta - \pi/2), \tag{7}$$

where θ corresponds to the azimuthal angle in spherical coordinates, and V now refers to the quantization volume delimited by the cavity. Observe we are treating the radiation field inside a volume, however the density of modes is practically parametrized in polar coordinates as $\mathbf{k} = k(\cos\phi, \sin\phi, 0)$. The usual relation for polarization vectors $\sum_s \hat{\mathbf{e}}^{\mu}_{\mathbf{k},s}\hat{\mathbf{e}}^{\nu}_{\mathbf{k},s} = \delta_{\mu,\nu} - \hat{\mathbf{k}}_{\mu}\hat{\mathbf{k}}_{\nu}$ (μ, ν the Cartesian components) here turns into

$$\sum_{s}g^{j,m*}_{\mathbf{k},s}g^{l,n}_{\mathbf{k},s} = \frac{kc}{2\hbar\epsilon_0 V}\left[\mathbf{d}^{z*}_{j,m}\mathbf{d}^{z}_{l,n} + \sum_{\mu,\nu\neq z}\mathbf{d}^{\mu*}_{j,m}\mathbf{d}^{\nu}_{l,n}(\delta_{\mu,\nu} - \hat{\mathbf{k}}_{\mu}\hat{\mathbf{k}}_{\nu})\right]. \tag{8}$$

Therefore, the 2D condition (7) decouples the component $\mathbf{d}^{z}_{j,m}$ of the dipole matrix elements from $\mathbf{d}^{x}_{j,m}$ and $\mathbf{d}^{y}_{j,m}$. This phenomena is absent in 3D scattering, where all components

of $\mathbf{d}_{j,m}$ are coupled, whereas at the other end, 1D case exhibits all components trivially uncoupled.

The single atom decay into two-dimensional vacuum modes is given by

$$K^{\mathrm{2D}}_{m,n}(\mathbf{r}_{jl}=0)=\mathbf{d}^{z*}_{j,m}\mathbf{d}^{z}_{l,n}\int_0^\infty\frac{ck^3dk}{(2\pi)^3\hbar\epsilon_0}\int_0^{2\pi}d\phi\int_0^\infty d\tau e^{i\omega_a\tau}(e^{-i\omega_{\mathbf{k}}\tau}-e^{i\omega_{\mathbf{k}}\tau})$$
$$+\sum_{\mu,\nu\neq z}\mathbf{d}^{\mu*}_{j,m}\mathbf{d}^{\nu}_{l,n}\int_0^\infty\frac{ck^3dk}{(2\pi)^3\hbar\epsilon_0}\int_0^{2\pi}d\phi(\delta_{\mu,\nu}-\hat{\mathbf{k}}_\mu\hat{\mathbf{k}}_\nu)\int_0^\infty d\tau e^{i\omega_a\tau}(e^{-i\omega_{\mathbf{k}}\tau}-e^{i\omega_{\mathbf{k}}\tau}),\tag{9}$$

where the index 2D applied on $K^{\mathrm{2D}}_{m,n}$ means the general kernel particularized to the two-dimensional scattering. The time integral present in Eq. (9) is solved by using the relation

$$\int_0^\infty d\tau e^{i(\omega_a\pm\omega_k)\tau}=\frac{\pi}{c}\delta(k\pm k_a)\pm iP\frac{1}{\omega_a\pm\omega_k},\tag{10}$$

where P refers to the Cauchy principal value. This term gives rise to the Lamb shift, a single atom energy shift which is due to its interaction with the radiation field. We will here neglect it, as it simply corresponds to a renormalization of the energy; remark that we do not neglect the so-called *collective* Lamb shift that rises from the interaction between the atoms via virtual photons, as it is still present in the final scattering kernel.

Using the relations

$$\mathbf{d}_{j,m}=d\left(i\frac{|m|}{\sqrt{2}},\frac{m}{\sqrt{2}},1-|m|\right),\tag{11a}$$

$$\int_0^{2\pi}d\phi(\delta_{m,n}-\hat{\mathbf{k}}_\mu\hat{\mathbf{k}}_\nu)=\pi\delta_{m,n},\tag{11b}$$

where the expression for $\mathbf{d}_{j,m}$ in (11b) includes choosing the quantization axis over z, and plugging (10) into (9), we obtain the two different decay rates:

$$\Gamma_0=K_{0,0}(\mathbf{r}_{jl}=0)=\frac{k_a^3d^2}{4\pi\hbar\epsilon_0},\tag{12a}$$

$$\Gamma_1=K_{\pm1,\pm1}(\mathbf{r}_{jl}=0)=\frac{k_a^3d^2}{8\pi\hbar\epsilon_0}=\frac{\Gamma_0}{2}.\tag{12b}$$

By looking at (10), one can see only the term $k=k_a$ contributes. Therefore, the uncoupling of $\mathbf{d}^z_{j,m}$ from the other components of $\mathbf{d}_{j,m}$ causes an anisotropy on the spontaneous emission process, since the lifetime of transition $e_{j,m=0}\to g_j$ is twice shorter than $e_{j,m=\pm1}\to g_j$. These decay rates will predict the coexistence of two scattering subsystems with different time scales, which vector nature of light will be crucial to select which subsystem is active.

Finally, we address the collective term by calculating the integrals describing the coupling between the atoms via the radiation field

$$K^{\mathrm{2D}}_{m,n}(\mathbf{r}_{jl}\neq0)=\mathbf{d}^{z*}_{j,m}\mathbf{d}^{z}_{l,n}\int_0^\infty d\tau e^{i\omega_a\tau}\int_0^\infty\frac{ck^3dk}{(2\pi)^3\hbar\epsilon_0}\int_0^{2\pi}d\phi(e^{-i\omega_{\mathbf{k}}\tau+i\mathbf{k}\cdot\mathbf{r}_{jl}}-\text{c.c.})$$
$$+\sum_{\mu,\nu\neq z}\mathbf{d}^{\mu*}_{j,m}\mathbf{d}^{\nu}_{l,n}\int_0^\infty d\tau e^{i\omega_a\tau}\int_0^\infty\frac{ck^3dk}{(2\pi)^3\hbar\epsilon_0}\int_0^{2\pi}d\phi(\delta_{\mu,\nu}-\hat{\mathbf{k}}_\mu\hat{\mathbf{k}}_\nu)(e^{-i\omega_{\mathbf{k}}\tau+i\mathbf{k}\cdot\mathbf{r}_{jl}}-\text{c.c.}).\tag{13}$$

Since the density of modes is nonzero only in the (x,y) plane, the z component of the atoms positions does not come into play, so in the relation

$$\hat{\mathbf{k}}_\mu\hat{\mathbf{k}}_\nu e^{\pm i\mathbf{k}\cdot\mathbf{r}_{jl}}=-\frac{\partial^2}{\partial x^\mu_{jl}\partial x^\nu_{jl}}e^{\pm i\mathbf{k}\cdot\mathbf{r}_{jl}},\tag{14}$$

where x^μ_{jl} actually spans only (x_{jl},y_{jl}). The angular integral then reads

$$\int_0^{2\pi}e^{\pm ikx_{jl}\cos\phi\pm iky_{jl}\sin\phi}d\phi=2\pi J_0(kr_{jl}),\tag{15}$$

where J_0 denotes the Bessel function of the first kind and of order 0, and $r_{jl}=\sqrt{x^2_{jl}+y^2_{jl}}$ is the Euclidean distance between each pair of atoms in the plane. Despite the integrands in (13) diverging in the limit $k\to\infty$, the modulus of the wave vectors k vary only slightly around $k=k_a$ (quasielastic scattering). We then apply the Wigner and Weisskopf approximation which approximates powers of k in the integral as k_a. Using the relation

$$\int_0^\infty d\tau e^{i\omega_a\tau}\int_0^\infty dk J_0(kr_{jl})\sin(kc\tau)=\frac{\pi i}{2c}H_0(k_ar_{jl}),\tag{16}$$

where H_α is the Hankel function of the first kind and of order α, we can calculate $K^{\mathrm{2D}}_{m,n}(\mathbf{r}_{jl}\neq0)$ from the action of the second order derivative of $H_0(k_ar_{jl})$ with respect to x^μ_{jl}. Practically, we get

$$K^{\mathrm{2D}}_{0,0}(\mathbf{r}_{jl}\neq0)=\Gamma_0H_0(k_ar_{jl}),\tag{17a}$$

$$K^{\mathrm{2D}}_{\pm1,\pm1}(\mathbf{r}_{jl}\neq0)=\Gamma_1H_0(k_ar_{jl}),\tag{17b}$$

$$K^{\mathrm{2D}}_{\pm1,\mp1}(\mathbf{r}_{jl}\neq0)=\Gamma_1H_2(k_ar_{jl})e^{\pm2i\varphi_{jl}}.\tag{17c}$$

These coefficients allow us to obtain the following set of equations for the atomic operators $\hat{\sigma}_j^{(m)}$:

$$\frac{d\hat{\sigma}_j^{(0)}}{dt} = -\frac{\Gamma_0}{2}\hat{\sigma}_l^{(0)} - \frac{\Gamma_0}{2}\sum_{l=1}^{N} H_0(kr_{jl})\hat{\sigma}_l^{(0)}, \tag{18a}$$

$$\frac{d\hat{\sigma}_j^{(\pm1)}}{dt} = -\frac{\Gamma_1}{2}\hat{\sigma}_j^{(\pm1)} - \frac{\Gamma_1}{2}\sum_{l\neq j}\left[H_0(kr_{jl})\hat{\sigma}_l^{(\pm1)} + e^{2i\varphi_{jl}}H_2(kr_{jl})\hat{\sigma}_l^{(\mp1)}\right], \tag{18b}$$

where $\tan\varphi_{jl} = (y_j - y_l)/(x_j - x_l)$. In both Eqs. (18a) and (18b) the atoms are coupled together through the same sublevel with a kernel term $H_0(kr)$ that scales as a 2D spherical wave $e^{ikr}/\sqrt{r}$ at large distances. This $1/\sqrt{r}$ scaling in 2D corresponds to long range coupling so we expect global coupling (or cooperative effects) to dominate over nearest neighbor coupling. In the vectorial case, the $m = \pm1$ sublevels are additionally coupled via a H_2 term which also scales as $e^{ikr}/\sqrt{r}$ at long range. However, with respect to global versus local interactions, H_0 diverges at the origin only as $\log(kr)$, so that the contribution of a small volume around the particle is finite $[\int_0^{r_0}\log(kr)2\pi r dr < \infty]$. Instead, the H_2 term diverges at the origin as $1/r^2$, which means that the interaction between the ±1 sublevels is dominated by the close neighbors or near-field terms at high densities $[\int_{r_-}^{r_0} 2\pi r dr/r^2 \underset{r_-\to 0}{\sim} -2\pi\log(r_-)]$.

Differently from the 3D case where scalar light is only an approximation for dilute systems, and where all sublevels are normally coupled, in 2D geometries scalar model holds for high densities. Yet, controlling the polarization of the injected light allows us to select either purely scalar or vectorial properties which make our approach quite versatile. In the end, two decoupled scattering subsystems appear: one involving a single sublevel of the excited state (the scalar case), the other one involving the remaining two sublevels (the vectorial case). As one can note the scalar and vector kernels are not decoupled through energy shifts like 3D work in Ref. [5], but rather by geometrical constraints. The microwave or optical cavity reshapes the density of electromagnetic modes into two dimensions.

The scattered field at a point $\mathbf{r} = (x, y)$ is calculated by a superposition of annihilation operators, namely

$$\hat{\mathbf{E}}(\mathbf{r}) = \sum_{\mathbf{k},s} \varepsilon_{\mathbf{k}}\hat{\mathbf{e}}_{\mathbf{k},s}a_{\mathbf{k},s}e^{-i\omega_{\mathbf{k}}t + i\mathbf{k}\cdot\mathbf{r}}, \tag{19}$$

where $\varepsilon_{\mathbf{k}} = \sqrt{\hbar\omega_{\mathbf{k}}/2\epsilon_0 V}$. With similar procedures used up to here, using (3b), it can be shown to lead to the following equation:

$$\hat{\mathbf{E}}(\mathbf{r}) = \hat{\mathbf{z}}\frac{\hbar\Gamma_0}{2di}\sum_{l=1}^{N}\left(H_0(k_a|\mathbf{r}-\mathbf{r}_l|) + \frac{i}{\pi k_a|\mathbf{r}-\mathbf{r}_l|}\right)\hat{\sigma}_l^{(0)} + \frac{\hbar\Gamma_1}{2d}\sum_{l=1}^{N}\sum_{m=\pm1}\mathbf{e}_m e^{-2mi\varphi_l}H_2(k_a|\mathbf{r}-\mathbf{r}_l|)\hat{\sigma}_l^{(m)} + \frac{\hbar\Gamma_1}{2d}\sum_{l=1}^{N}\sum_{m=\pm1}\mathbf{e}_m H_0(k_a|\mathbf{r}-\mathbf{r}_l|)\hat{\sigma}_l^{(-m)}, \tag{20}$$

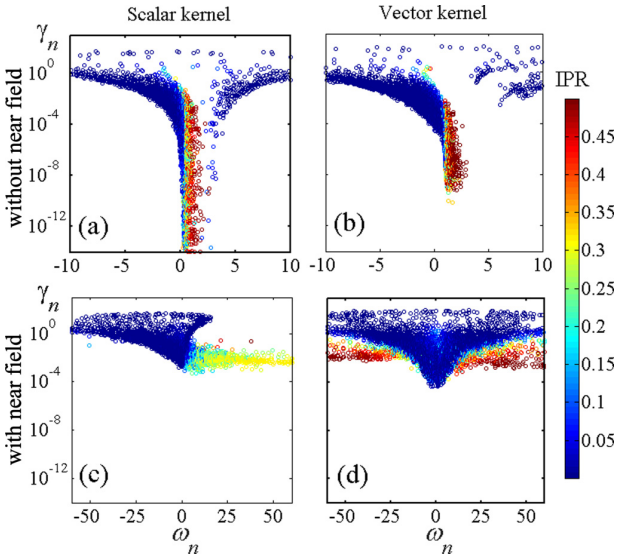

FIG. 2. (Color online) Inverse participation ratio of the scattering modes in the complex plane of the eigenvalues (γ_n, ω_n) for scalar light (a) without and (c) with near-field terms, in units of Γ_0, and vectorial light (b) without and (d) with near-field terms, in units of Γ_1, (a) and (d) being the physical cases. Simulations realized for a homogeneous disk cloud of $N = 5000$ particles with a homogeneous $\rho/k^2 = 1$ density.

with $\tan\varphi_l = (y - y_l)/(x - x_l)$ and $\mathbf{e}_\pm = (\hat{\mathbf{x}} \pm i\hat{\mathbf{y}})/\sqrt{2}$. The $m = 0$ sublevel is coupled only to light with polarization along z, whereas the $m = \pm1$ sublevels are coupled together through p polarizations.

III. SPECTRAL ANALYSIS OF THE LINEAR EQUATIONS

We now turn our attention to the spectral properties of the system. The scattering modes are the eigenmodes $\Psi^{(n)}$ of the linear equations (18a) and (18b), where n labels the eigenmodes. Their lifetime $1/\gamma_n$ and energy ω_n are given by the real and imaginary part of the associated eigenvalues, respectively. Defining $\psi_j^{(n)} = (\Psi^{(n)})_j$, the modes can also be characterized by their inverse participation ratio (IPR) $(\sum_j |\psi_j^{(n)}|^4)/(\sum_j |\psi_j^{(n)}|^2)^2$ that quantifies the (inverse) number of atoms substantially involved in the scattering mode. In the vectorial model we renormalize the IPR to remain 1/2 for pairs.

In the scalar case the eigenvalue distribution shown in Fig. 2(a) exhibits strongly subradiant modes, which we define as modes with very long lifetimes ($\gamma_n \ll \Gamma_0$). The distribution can be used to look for a single parameter scaling, by computing a spectral overlap function conveniently defined as $g = \langle 1/\gamma_n\rangle^{-1}/\langle\omega_n - \omega_{n-1}\rangle$, where the modes n are ordered by increasing energy. In line with the 3D results, we observe a monotonic decrease of g with the system size for scalar light [see Fig. 3(a)]. Consequently, the scaling function $\beta = \partial\ln g/\partial\ln(kR)$ is clearly negative for all values of g [see Fig. 3(b)], as expected for Anderson localization in 2D. We note that this function g is only one among several possibilities of defining a spectral overlap and has not been

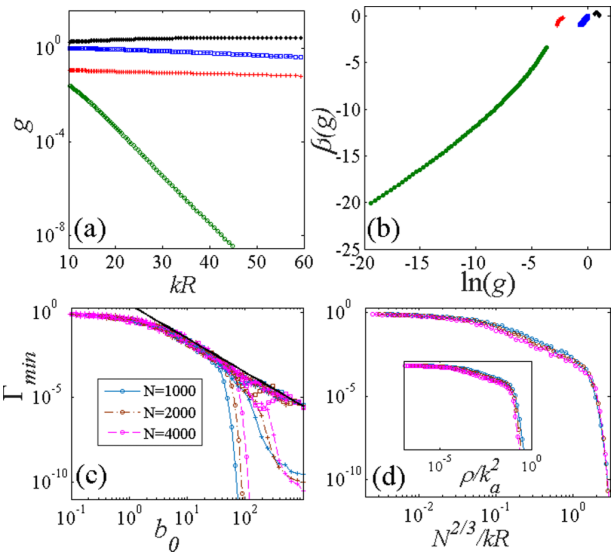

FIG. 3. (Color online) (a) Thouless number g as a function of the dimensionless system size kR, for density $\rho/k^2 = 0.3$ (b) scaling function β. Longest mode lifetimes for different number of particles (c) as a function of the optical thickness b_0 and for all four scattering models and (d) as a function of the dimensionless parameter $N^{2/3}/kR$ for scalar light. The circles are for scalar light, the squares for vectorial light, the stars for scalar light *with near field*, and the plus for vectorial light *without near field*. The black line in (c) stands for the $\sim 1/b_0^2$ curve of the radiation trapping lifetime. In (c) and (d) blue, brown, and magenta curves correspond, respectively, to simulations with $N = 1000$, 2000, and 4000 particles. The inset in (d) shows $\Gamma_{\min}$ as a function of atomic density, indicating that density is not the best scaling function for $\Gamma_{\min}$, even in the high density limit.

shown to be unequivocally related to transport properties of electromagnetic radiation.

The dimensionless scaling parameter g is defined in the scaling theory [13] as the ratio between the Heisenberg time and the Thouless time. The former corresponds to the time associated with the mean spacing between the energy levels, i.e., $\hbar/\langle E_n - E_{n-1}\rangle$, which in our case reads $1/\langle\omega_n - \omega_{n-1}\rangle$. The latter corresponds to the time necessary for a photon to escape from the sample, and in our open system with eigenmodes of lifetime $1/\gamma_n$, we define it as $\langle 1/\gamma_n\rangle$. Following this interpretation, the localization regime is characterized by a Thouless (diffusion) time that becomes larger than the Heisenberg one.

In the vectorial case exhibited in Fig. 2(d) we observe a dramatically different eigenvalue distribution. Indeed, even though long-lived modes ($\gamma_n \ll \Gamma_0$) exist, they are limited to values larger by several orders of magnitude compared to the scalar case. The corresponding spectral overlap also shows a distinct behavior, with g almost independent of the system size kR [see Fig. 3(a)], yielding a scaling function β close to zero, albeit slightly negative [see Fig. 3(b)]. This behavior of the scaling function β might make this vectorial case very interesting to study fine corrections of the atom-atom interactions as it seems to be close to the critical regime.

The above discussion is consistent with the conclusions drawn from the study of eigenvalues in 3D [4,10]. With the aim to pin down the essential ingredient of the difference between the scalar and vectorial model, we artificially introduced or removed short range terms in the two configurations. More specifically, we removed the near-field coupling from vectorial scattering by substituting $H_2(kr)$ by $H_2(kr) + 4i/\pi(kr)^2$, thus suppressing the near fields. The corresponding eigenvalue distribution is shown in Fig. 2(b). Despite the fact that the ± 1 sublevels remain coupled, the eigenvalue distribution of the vectorial case without near-field terms closely resembles that of the scalar case, even though the smallest values of γ_n do not reach the lowest limits obtained in the scalar case. Conversely, if we add a near-field term, which we choose as the one present in vectorial scattering $-4i/\pi(kr)^2$, to the scalar kernel $H_0(kr)$, the long lived modes of the purely scalar case disappear [see Fig. 2(c)]. The scaling analysis, as well as a thorough analysis of the spatial extension of the modes, confirm that Anderson localization is absent from these altered interactions.

Focusing on lifetimes, the study of the longest of them $\Gamma_{\min}$ first reveals that for low densities ($\rho < 0.3$), long lifetimes are caused by the radiation trapping $\sim 1/b_0^2$ [14], with b_0 the cloud optical depth [15] [see Fig. 3(c)]. However, for scalar light, the appearance of the localized modes for $\rho/k^2 > 0.3$ comes along with lifetimes much larger than those predicted by radiation trapping, see Fig. 3(c). These lifetimes are not simply a function of the density ρ/k^2 but appear to scale as $N^{2/3}/kR$ and to decay exponentially fast [see Fig. 3(d)]. This result is clearly beyond the standard Anderson localization, where quantities scale as N/R^2, or cooperative effects where it scales as N/R, and calls for new approaches. Finally, while scalar light *with near fields* exhibits lifetimes that always decay as $1/b_0^2$ [it is almost with the radiation trapping black curve in Fig. 3(c)], both vectorial light *with* and *without* near field exhibit lifetimes longer than that of radiation trapping: These come from atom pairs instead of localized modes, as reveals the analysis of the IPR and of the spatial profiles.

These results suggest that both the presence of near-field interaction terms [4] and coupling of different sublevels can break down long lifetimes and localization. We also found that removing the anisotropy present in vectorial scattering [$e^{\pm 2i\varphi_{jl}}$ in Eq. (18b)] does not restore localized modes.

Our 2D study, apart from the investigation of subradiance and localization in lower dimensions, allows for a more efficient numerical study of the eigenvectors of the dipole-dipole coupling. One aspect of the eigenvector analysis is already seen in Fig. 2, where the IPR of the eigenmodes allows, for instance, a clear identification of atomic pairs (red circles in Fig. 2 corresponding to an IPR close to 0.5, indicating atom pairs). In addition, the 2D configuration allows for an easy systematic study of the shapes of the eigenvectors: two typical eigenmodes are shown in Fig. 1. The localized mode is spatially well confined [inset in Fig. 4(a)] and has a clear exponential shape over several orders of magnitude [Fig. 4(a)]. Vectorial eigenvectors, on the other hand, are extended over almost the whole system size [inset in Fig. 4(b)], with no indication for an exponential decrease [Fig. 4(b)]. This observation is again in line with previous conclusions in 3D [4,10]. The scalar light *with* near fields and vectorial light *without* near fields do not exhibit any exponentially localized modes, but rather extended modes, as can be observed in Fig. 5. These scatterings, as well as the vectorial light *with* near fields,

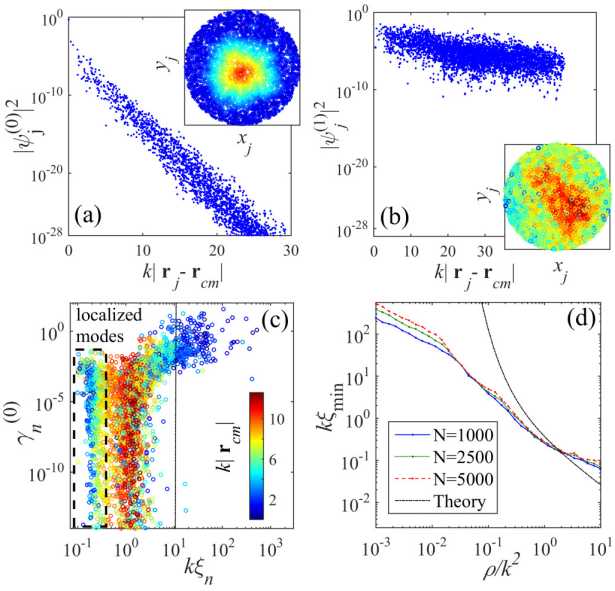

FIG. 4. (Color online) Spatial profile of the most subradiant nonpair mode for (a) scalar light (exponentially localized mode) and (b) vectorial light (delocalized mode), as a function of the distance to its center of mass $\mathbf{r}_{\text{c.m.}}$. The 2D profile is exhibited in the inset. (c) Inverse lifetime versus localization length of the modes for scalar light; the localization length ξ is obtained by exponential fit of the spatial profile of the mode [(a) for an example], so it is meaningful only for localized modes, within the dashed-bordered box. More specifically, the strongly subradiant modes lying outside of the box are extended, and so are the superradiant (ξ typically exceeds the system size for these, sign of a full delocalization). (d) Localization length for scalar light as a function of the normalized density, for different scatterer number. The "theory" line refers to the theoretical prediction $k\xi = (k^2/4\rho)\exp(\pi k^2/8\rho)$. (a) and (b) were realized for $N = 5000$ and $\rho/k^2 = 1$, so $kR \approx 40$; (c) is for $N = 5000$ and $\rho/k^2 = 10$, so $kR \approx 12.6$, as marked by the dash-dotted line.

may however present features of hybrid states where localized and extended subradiant features combine [16].

The localized nature of the strongly subradiant modes is thus confirmed by the analysis of their spatial profile. Furthermore, as long as the mode does not considerably extend over the edge of the atomic cloud, its localization length and lifetime are uncorrelated [uniform filling of the box in Fig. 4(c) with modes]. There is however a correlation between the position of the mode (indicated by the color code, where blue points mark modes at the center of the system) and its localization length. Some modes even mix to surface (whispering gallery) modes that have a much larger spatial extend. Yet there is no correlation between the position of the mode (at the center or near the edge of the cloud) and its lifetime. The absence of correlation between the lifetime of the modes and their localization length calls for a differentiation between spatial and temporal localization. Although all spatially localized modes are subradiant, the shortest localization length may not be associated with the longest lifetimes. This corroborates studies on photon escape rates that failed to observe the localization phase transition [7], and is also highlighted by the fact that spatial localization is affected by boundary effects while temporal localization, surprisingly, does not seem to be. Finally, as can be seen in Fig. 4(d), for densities above $\rho/k^2 \sim 0.05$ the localization length no longer depends on the system size, but only on the spatial density. These curves are not in agreement with the prediction of localization length from the perturbative approach in the weak disordered regime [17].

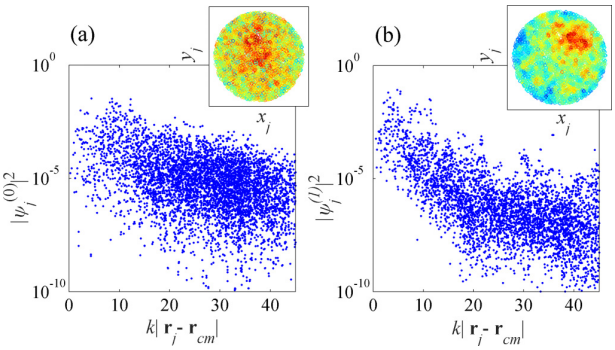

FIG. 5. (Color online) Spatial profile of the most subradiant nonpair mode for (a) scalar light *with* near fields and (b) vectorial light *without* near fields. Simulations realized for an homogeneous disk cloud of $N = 5000$ particles with an homogeneous $\rho/k^2 = 1$ density.

We have also verified [see Fig. 3(a)] that the corresponding spectral overlap g and the scaling function β for the altered interactions are qualitatively similar to the one of the purely vectorial case, i.e., they deviate only slightly from zero. Similarly, inspection of the eigenvalues did not reveal any spatially localized mode. Together with the above results on lifetimes, this observation suggests that extremely long lifetimes of modes, well beyond radiation trapping ones, come along with spatial localization, i.e., subradiance may be a condition necessary to localization.

IV. CONCLUSIONS

In conclusion, we explored 2D scattering by point scatterers in a scalar and a vectorial limit. Even though our eigenvalue analysis is consistent with previous results and interpretations of localization, our procedure of artificially introducing or removing near-field terms combined with a spatial analysis of the eigenfunctions support that very long lifetimes come along with Anderson localization, but both near-field terms and the coupling of polarizations may prevent their emergence. Furthermore, we reported an absence of correlations between lifetime and localization length of localized modes, pointing at the difference between spatial and temporal localization. An important task for the future will be to relate both the 2D and 3D studies to transport properties of electromagnetic waves and to compute observables that can be tested in experiments.

ACKNOWLEDGMENTS

We acknowledge financial support from the Research Executive Agency (program COSCALI, Grant No. PIRSES GA-2010-268717) project COSCALI, from ANR (project LOVE, ANR-14-CE26-0032), from GDRI NSEQO, from CNPq (project PVE 400228/2014-9), and FAPESP. We thank E. Akkermans, D. Delande, and S. Skipetrov for stimulating discussions.

[1] P. W. Anderson, Phys. Rev. **109**, 1492 (1958).
[2] S. John, Phys. Rev. Lett. **58**, 2486 (1987).
[3] A. Figotin and A. Klein, Commun. Math. Phys. **184**, 411 (1997).
[4] S. E. Skipetrov and I. M. Sokolov, Phys. Rev. Lett. **112**, 023905 (2014).
[5] S. E. Skipetrov and I. M. Sokolov, Phys. Rev. Lett. **114**, 053902 (2015).
[6] R. H. Dicke, Phys. Rev. **93**, 99 (1954).
[7] E. Akkermans, A. Gero, and R. Kaiser, Phys. Rev. Lett. **101**, 103602 (2008).
[8] P. W. Courteille, S. Bux, E. Lucioni, K. Lauber, T. Bienaim, R. Kaiser, and N. Piovella, Eur. Phys. J. D **58**, 69 (2010).
[9] E. Abrahams, P. W. Anderson, D. C. Licciardello, and T. V. Ramakrishnan, Phys. Rev. Lett. **42**, 673 (1979).
[10] L. Bellando, A. Gero, E. Akkermans, and R. Kaiser, Phys. Rev. A **90**, 063822 (2014).
[11] D. Laurent, O. Legrand, P. Sebbah, C. Vanneste, and F. Mortessagne, Phys. Rev. Lett. **99**, 253902 (2007).
[12] K. Busch, G. von Freymann, S. Linden, S. Mingaleev, L. Tkeshelashvili, and M. Wegener, Phys. Rep. **444**, 101 (2007).
[13] J. T. Edwards and D. J. Thouless, J. Phys. C **5**, 807 (1972).
[14] T. Holstein, Phys. Rev. **72**, 1212 (1947).
[15] The resonant optical depth is defined as $b_0 = \sigma_s \int \rho(0,y)dy$, with $\sigma_0 = 4/k$ $(8/k)$, the resonant scattering cross section for scalar (vectorial) light. For an homogeneous disk distribution, one gets $b_0 = 8N/\pi kR$ $(16N/\pi kR)$.
[16] A. Biella, F. Borgonovi, R. Kaiser, and G. L. Celardo, Europhys. Lett. **103**, 57009 (2013).
[17] P. A. Lee and T. V. Ramakrishnan, Rev. Mod. Phys. **57**, 287 (1985).

3.3 Coherent backscattering of inelastic photons from atoms and their mirror images

PHYSICAL REVIEW A **94**, 053806 (2016)

Coherent backscattering of inelastic photons from atoms and their mirror images

P. H. Moriya,[1] R. F. Shiozaki,[1,2] R. Celistrino Teixeira,[1,2] C. E. Máximo,[1] N. Piovella,[3] R. Bachelard,[1] R. Kaiser,[4] and Ph. W. Courteille[1,*]

[1]*Instituto de Física de São Carlos, Universidade de São Paulo, C.P. 369, 13560-970 São Carlos, SP, Brazil*

[2]*Departamento de Física, Universidade Federal de São Carlos, Rod. Washington Luís, km 235 - SP-310, 13565-905 São Carlos, SP, Brazil*

[3]*Dipartimento di Fisica, Università degli Studi di Milano, Via Celoria 16, I-20133 Milano, Italy*

[4]*Institut Non Linéaire de Nice, UMR 6618 CNRS, 1361 route des Lucioles, 06560 Valbonne, France*

(Received 12 April 2016; published 7 November 2016)

Coherent backscattering is a coherence effect in the propagation of waves through disordered media involving two or more scattering events. Here we report on the observation of coherent backscattering from individual atoms and their mirror images. This system displays two important advantages: First, the effect can be observed at low optical densities, which allows us to work in very dilute clouds or far from resonance. Second, due to the fact that the radiation of an atom interferes constructively with that of its own image, the phenomenon is much more robust to dephasing induced by strong saturation. In particular, the contribution of inelastically scattered photons to the interference process is demonstrated.

DOI: 10.1103/PhysRevA.94.053806

I. INTRODUCTION

Light propagating in an optically thick sample is subject to multiple scattering. Although part of the propagation can be described by a diffusion equation neglecting interferences, wave effects can alter the distribution of scattered light. In particular, disorder in the sample may lead to an enhanced scattering into the backward direction. The effect is known as coherent backscattering (CBS) in mesoscopic physics, and has been studied extensively with classical scatterers [1–7]. The advent of laser-cooling techniques allowed us to manipulate and control atomic gases, thus enabling their use as resonant and quantum scatterers. This triggered the study of coherent multiple scattering in a regime where the quantum internal structure, the wave-particle duality, and quantum statistical aspects play a role [8–12].

CBS is understood as resulting from the constructive interference between a scattering path involving two or more scatterers and the reciprocal (time-reversed) path (see Ref. [13], and paths (i) and (ii) in Fig. 1). The interference of reciprocal paths is actually robust when summed up over a large disordered sample, which was one of the surprising features in the first observation of CBS in the 1980s [1–3]. More specifically, some paths add up incoherently and result in a background radiation, whereas reciprocal paths lead to an enhanced intensity in the backward direction. However, the quantum nature of the atoms leads to deviations in the behavior of CBS as compared to classical scatterers. For example, the presence of a Zeeman structure can break the symmetry between the two reverse paths and reduces the contrast between the enhanced peak of radiation and the background [8,14]. The time-reversal symmetry of the reciprocal multiple scattering paths is also broken in the strong driving regime, as a which-path information becomes available through the inelastically scattered photons [9,12,15]. Such saturation-induced loss of coherence in CBS was reported with a cold strontium gas [11] and a cold rubidium gas [12,15]. Unfortunately, the theoretical treatment of saturation in multiple scattering is very challenging [13,16–23] and has not been solved in full generality.

Interestingly in a different geometrical configuration coherence effects on the backscattered light can also be observed in optically thin samples, where multiple scattering is too weak to produce observable signatures. Indeed the introduction of a reflective interface—a dielectric mirror for example—allows for the radiation of the image scatterer to interfere constructively with that of the original scatterer, eventually resulting in a coherent backscattering process [24]. This single scattering regime here involves four processes for each atom (depicted in Fig. 1), accounting for the real atom and its mirror image, as well as the laser and its image. Let us call $\mathbf{k}_0$ the incident wave vector, $\mathbf{k}$ the scattered wave vector, and $\hat{z}$ the normal to the mirror. For a single atom, all four processes sum up coherently, and the resulting scattered light pattern presents full interference contrast. When the radiation of all atoms is disorder averaged, though, all interference fringes disappear, except at wave vectors $\mathbf{k}$ such that $\mathbf{k}_0 \cdot \hat{z} = -\mathbf{k} \cdot \hat{z}$, because at these specific directions processes (i) and (ii) have the same optical path for all atoms in the cloud. The resulting interference fringes present a circular symmetry around the mirror's normal direction, with a number of maxima depending on the spatial extension of the atomic cloud. This effect, which will henceforth be referred to as mirror-assisted coherent backscattering (m-CBS), has been observed for classical scattering media [25].

In this work we report on the experimental observation of m-CBS from a laser-cooled gas of strontium atoms in the presence of a dielectric mirror. A series of circular fringes predicted by the theory are experimentally observed and quantitatively analyzed. The period and envelope of the interference fringes allow us, respectively, to precisely determine the position and longitudinal size of the atomic cloud. We show that in the strong field regime, where the atoms are fully saturated, the comparison between theory and experimental results allows us to show that, in contrast to CBS, inelastic photons fully contribute to m-CBS.

*philippe.courteille@ifsc.usp.br

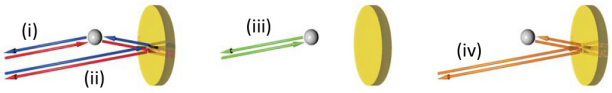

FIG. 1. Four processes contributing to m-CBS. In the low intensity limit, reciprocal paths (i) and (ii) contribute to the m-CBS fringes, whereas paths (iii) and (iv) yield a smooth background intensity.

II. EXPERIMENTAL SETUP

We prepare our atomic sample in a typical strontium apparatus, which we briefly describe in the following. A collimated atomic beam emerges from an array of microtubes located at the output of an oven heated to 550 °C. The atomic beam is then decelerated in a 28-cm-long Zeeman slower in spin-flip configuration by a counterpropagating laser beam of power ∼40 mW tuned 500 MHz to the red of the 461 nm resonance. The Zeeman slower beam has a $1/e^2$ radius of 4 mm at the entrance of the experimental apparatus, being focused onto the oven output after propagation through the whole system (about 90 cm long). The cooled strontium beam is captured in the science chamber by a magneto-optical trap (MOT) generated by three pairs of counterpropagating collimated 461 nm laser beams and a quadrupole magnetic field; the latter is produced by a pair of coils in anti-Helmholtz configuration (axial magnetic gradient $|\nabla B| = 70$ G/cm). Each laser beam has a $1/e^2$ radius of 5 mm and is detuned by −40 MHz from resonance. A repumping laser addressing the 497 nm $^3P_2 \rightarrow {}^3D_2$ transition is used to recycle atoms that have decayed to the metastable state $^3P_2$. In this way we are able to generate cold gases with $\sim 10^8$ ^{88}Sr atoms at a temperature below 10 mK after a 2s loading time. Resonant absorption imaging reveals an approximate Gaussian density profile with a $1/\sqrt{e}$ radius of 0.9(1) mm.

The setup for the m-CBS experiment is sketched in Fig. 2. The scattering medium is a cold gas of ^{88}Sr atoms in its ground state $^1S_0$, and the transition $^1S_0 \rightarrow {}^1P_1$ [at $\lambda = 2\pi/k = 461$ nm with a linewidth of $\Gamma = (2\pi)30.5$ MHz] is used for the resonant scattering. The 461 probe laser beam (the m-CBS beam) has a waist of 1.5 mm and linear polarization. It first passes through a 50-50 nonpolarizing wedged beamsplitter before reaching the atoms. A combination of two lenses with focal distances $f = 15$ cm and separated by a distance of $2f = 30$ cm creates a virtual image of a real mirror, placed at a distance d after the last lens, at a distance $2f - d$ before the first lens. This configuration has been used to study Talbot physics and even allows negative distances to be realized [26,27]. The m-CBS beam is reflected with an angle $\theta_0 \sim 1^\circ$ compared to the mirror's normal direction. Having crossed again the atomic cloud, the beam is partially reflected by the beamsplitter onto a 200 mm lens. A CCD camera placed at the focal plane of the lens allows for the detection of the angular radiation pattern. To avoid the direction of the reflected m-CBS beam, which would saturate its pixels, the CCD camera only captures part of the circular pattern. An experimental measurement of such fluorescence pattern is shown in the top right area of Fig. 2.

After turning off the MOT cooling beams, we wait 200 μs and shine the m-CBS beam pulse of 200 μs duration onto the atomic cloud, capturing an image in the presence of atoms. After 1 s we record a background image in the absence of atoms. We run this sequence ≈ 200 times for the same parameters to obtain a disorder-averaged final image as shown in Fig. 2.

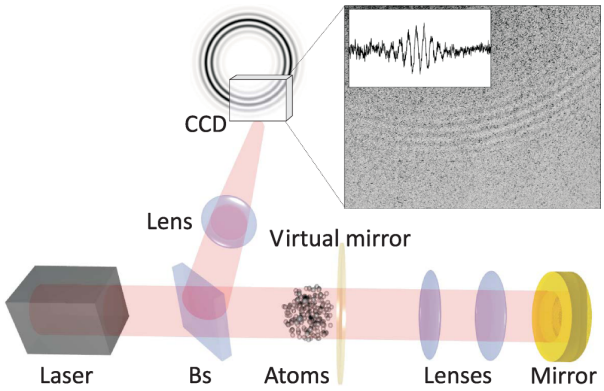

FIG. 2. Experimental setup: A laser beam passes through a beamsplitter (BS) before illuminating the atomic cloud a first time. It is then reflected on a virtual mirror (VM), created by two lenses and a physical mirror, at a small angle of $\theta_0 \sim 1^\circ$ with the normal of the mirror. After being reflected, it crosses the cloud again, before being sent by the beamsplitter, to a CCD camera detecting the angular distribution of the light in the focal plane of a lens. The top right picture shows an interference pattern obtained in our experimental setup, exhibiting the predicted circular symmetry. The inset is an azimuthal angular average of the picture.

III. LINEAR REGIME

The interference phenomenon of m-CBS is best understood in the linear regime, i.e., for a saturation parameter $s = 2\Omega_0^2/(\Delta^2 + \Gamma^2/4) \ll 1$, where Ω_0 is the Rabi frequency due to the incident laser and Δ is the laser detuning from the atomic resonance. In this limit the atoms behave as classical linear scatterers and the total fluorescence is a linear combination of four processes depicted in Fig. 1. The reciprocity of processes (i) and (ii) requires us to add up the corresponding field amplitudes for each atom, whereas paths (iii) and (iv) have no reciprocal counterpart, and so the corresponding scattering intensities contribute, after disorder averaging, to an incoherent background. In this low saturation limit ($s \ll 1$), the intensity radiated by a Gaussian cloud of atoms and its mirror image reads (see Appendix B)

$$I(\theta) \propto s\left\{1 + \tfrac{1}{2} e^{-2(\theta_0 k\sigma_z)^2(\theta-\theta_0)^2} \cos[2\theta_0 kh(\theta - \theta_0)]\right\}, \quad (1)$$

where h is the distance between the virtual mirror and the center of the atomic cloud and σ_z is the longitudinal cloud radius at $1/\sqrt{e}$. To obtain Eq. (1), a small angle approximation has been applied ($\theta_0 \ll 1$ and $|\theta - \theta_0| \ll \theta_0$). The second term in the bracket on the right-hand side of Eq. (1) corresponds to the single scattering interference of m-CBS, surviving averaging over the atomic spatial Gaussian distribution within a Gaussian angular envelope of half-width at $1/e^2$ given by $\Phi = 1/\theta_0 k\sigma_z$. Since the fringes have an angular period $\Theta_f = \pi/\theta_0 kh$, one typically expects to detect a number

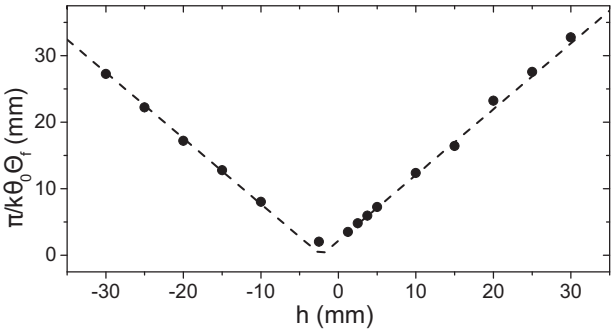

FIG. 3. Mirror position expected from m-CBS theory (i.e., $h_{\rm thr} = \pi/k\theta_0\Theta_f$) as a function of the experimental mirror position. This measurement allowed us to detect an initial experimental misalignment of $x_0 = 2.1(1)$ mm, which corresponds to the shifted minimum of the fit $h_{\rm thr} = |Ah + x_0|$ (dashed line); we obtained $A = 0.988(12)$. The error bars associated with the experimental data are smaller than the symbol size.

$\sim h/\pi\sigma_z$ of fringes on the scattered light. Together, both terms yield an ideal contrast of m-CBS of $C = 1$, defined as $C = (I_{\rm max} - I_{\rm min})/I_{\rm background}$. The fringes' period depend on the inverse of the distance of the cloud to the mirror ($\Theta_f = \pi/\theta_0 kh$), so the position of the mirror can in principle be evaluated from the fringes' pattern. To confirm this effect, the (virtual) mirror position h was varied for about 6 cm around the center of the cloud, and for each position an interference pattern similar to that of Fig. 2 was extracted. Note that we are able to place the virtual mirror at negative distances (i.e., the light first passes through the virtual mirror and then the atoms), and still have the m-CBS effect. Figure 3 shows the measured dependence of the fringes' period Θ_f (or, equivalently, of the deduced mirror distance $\pi/k\theta_0\Theta_f$) as a function of h. The excellent linear behavior not only shows a good agreement with theory, but also indicates that the initial experimental positioning was misaligned by 2.1(1) mm.

IV. SATURATED REGIME

In the saturated regime, the atomic dipole moment has a nonlinear response to the applied radiation field. It is then no longer possible to add up linearly the amplitudes of four independent processes. In order to better understand how the contrast of m-CBS depends on the saturation parameter, we turn to an alternative picture, valid for all saturation, including the low and large saturation limits. In this new picture, we first consider the total fluorescence of a single atom and its mirror image. This fluorescence is a coherent superposition of the light scattered by the atom and its mirror image, which have the same amplitude and are strongly correlated. This leads, for a single atom, to an undamped far field fringe pattern with full contrast. Furthermore, different atoms located at different distances from the virtual mirror are exposed to different local amplitudes of the standing wave created by the superposition of the incoming and reflected m-CBS beams [see Eq. (B1) of Appendix B]. For a mirror of perfect reflectivity, and neglecting the attenuation of the m-CBS beam after its passage through the atomic cloud, both the incoming and reflected m-

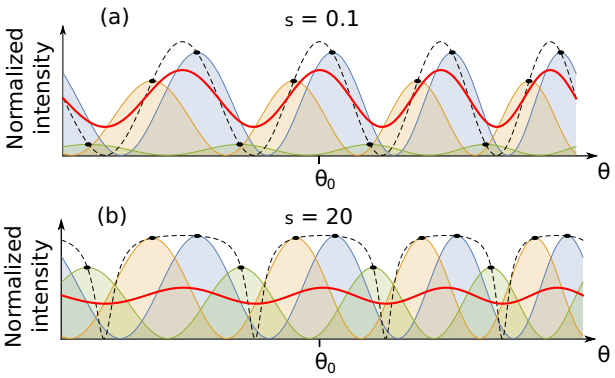

FIG. 4. Single-atom [colored (shaded) areas] and cloud-averaged [red (gray) thick line] fringe patterns in the linear (a) and saturated (b) regime. The reason for the periodic modulation of the fringes' maxima for different atoms is explained in the main text; the black dashed line denotes the maximum amplitude of individual atomic fluorescence fringes, as a function of the maxima position. The maxima of all single-atom curves are identified by a black dot. In the saturated regime, the saturation of the atoms reduces the amplitude modulation, and the contrast of the averaged fringes decreases.

CBS beams have equal intensity, and the standing wave created has perfect nodes and antinodes. The absolute amplitude of the far field fluorescence fringes of a single atom is thus a function of the local light intensity at its position, which presents the nonhomogeneous distribution of the standing wave. Atoms at the maxima of the standing wave will thus have their far field fluorescence pattern with maximum amplitude (see blue line in Fig. 4), compared to other atoms within the atomic cloud (e.g., yellow or green lines in Fig. 4). Within the previous description based on four different processes, valid at low s, these atoms at the maxima of the standing wave are those that have all four processes summed up constructively, with a maximum of the scattered intensity at $\theta = \theta_0$. On the other hand, for different atomic positions in the standing wave, while the reciprocal processes (i) and (ii) have always constructive interference at $\theta = \theta_0$, the angular position of the maximum of the fluorescence for processes (iii) and (iv) varies and do not always cooperate to produce a maximum intensity at $\theta = \theta_0$. Hence, adding up coherently all four amplitudes for a single atom creates angular fringes which are a function of the atomic position, with different amplitudes, and maxima at different angles. An illustration of some of these single-atom angular fluorescence patterns are shown in Fig. 4 by the colored, filled curves. The black dashed curve shows the dependence of the amplitude of all possible single-atom fluorescence fringes as a function of the position of the maxima of the fringes. Considering an extended atomic sample leads to the superposition of shifted fringes with different amplitudes. Then, averaging over various disorder configurations leads to a fluorescence pattern with contrasted fringes around $\theta = \theta_0$ (shown by the thick red curve).

As expected, for low saturation ($s \ll 1$) this interpretation yields the same contrast $C = 1$ as the interpretation based on reciprocal paths and an incoherent background. However this alternative interpretation of m-CBS allows us to go beyond the linear response theory and obtain quantitative predictions

for the saturated m-CBS regime, which is illustrated by Figs. 4(a) and 4(b). For $s = 20$, the position of the maxima of each individual atomic fringe is the same as for $s \ll 1$. Except for atoms in an ever narrower slice around the nodes of the standing wave produced by the incident laser, though, the amplitude of these individual fringes all saturate now to the same value. After averaging over all atoms, the contrast of the total detected intensity pattern, as illustrated by the red lines in Fig. 4(b), is reduced. Note that for the sake of simplicity, the calculation shown in Fig. 4 is done for atoms distributed over a small region of size of the order of a few wavelengths, and the envelope of the fringes [as expressed by the exponential function in Eq. (1)] is thus not visible.

In the discussion of the reduced contrast of CBS, another important argument has been the role of the inelastically scattered light, also known as the Mollow triplet. In the single scattering regime considered here, one can solve the optical Bloch equations of independent atoms, and then sum their (independent) scattered field. For each atom, one computes the field scattered by the oscillating dipole as being proportional to the optical coherence. In the limit of vanishing saturation, this allows us to compute the total scattered intensity, as all light is elastically scattered. For larger saturation however, the optical coherence saturates and even decreases to zero for very large values of s. In contrast, the excited state population saturates to a nonzero value and allows us to compute the total scattered intensity. The difference between the light scattering computed from the atomic coherence or the excited state population corresponds to inelastically scattered light (sometimes interpreted as being stimulated by vacuum fluctuations). For atoms separated by more than one wavelength, emission of such inelastic photons corresponds to randomly oscillating dipoles and are thus assumed not to preserve complete phase coherence with the incident laser, resulting in a reduction of the CBS contrast, in addition to the nonlinear response. In m-CBS however, the two atoms contributing to the fringes (i.e., the atom and its mirror image) have strongly correlated oscillations, which preserve the relative phase, even when randomly oscillating. Thus, inelastic scattering is expected to fully contribute to the m-CBS effect, leading to a lower reduction of the contrast for increasing saturation, as compared to CBS. As detailed in Appendix B we have derived a prediction for the m-CBS contrast based on the elastically scattered light alone [see Eq. (B11)] or based on the light scattered using the excited state population [see Eq. (B10)]. The resulting predictions are indicated in Fig. 5 by "elastic scattering only" and "elastic and inelastic scattering," respectively. We note that, for CBS, self-interference of inelastic photons has been identified to lead to a finite contrast even in the very large saturation limit [19]. We also note that another different, hitherto unexplained scaling for CBS with rubidium has been reported in [12] and might be due to a modification of the internal states of the rubidium atoms [18]. In any case, our model including elastic and inelastic scattering predicts m-CBS to be much more robust against saturation than CBS.

A precise measurement of the contrast and its dependence on the saturation parameter requires a careful data treatment in order to fully eliminate the undesired additional signal at the camera created by the reflected m-CBS beam scattered from all the optical elements. The procedure for extracting

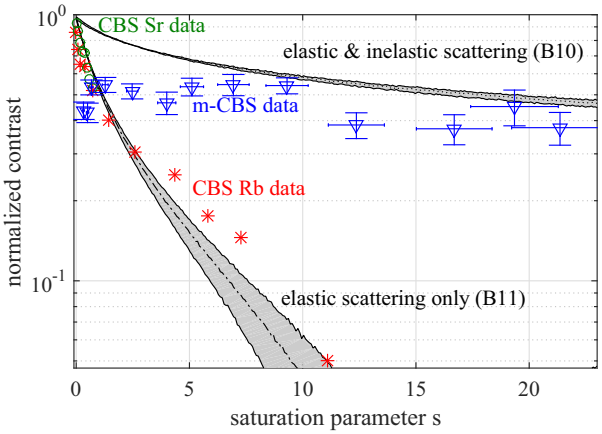

FIG. 5. Experimental m-CBS contrast (blue triangles), compared to the normalized CBS one from a strontium cloud [11] (green circles) and from a rubidium cloud [15] (red stars). The gray areas for the theoretical predictions {for both the elastic scattering only, and the elastic and inelastic scattering [see main text and Eqs. (B11) and (B10) of Appendix B)]} account for the precision within which our experimental parameters are known: $h = 8 \pm 0.5$ mm and $\sigma_z = 0.9 \pm 0.1$ mm. The data are presented as a function of the saturation parameter s at the center of the probe beam.

the fluorescence signal out of our raw data is detailed in Appendix A. For a given mirror position [$h = 8.0(5)$ mm] and cloud size [$\sigma_z = 0.9(1)$ mm], we have repeated the experimental sequence described before for several different intensities of the m-CBS beam. This allowed us to obtain a series of curves from which the absolute fringe contrast could be extracted. Figure 5 confronts the saturation behavior of the enhancement factor measured in our m-CBS setup and conventional CBS measured by other groups, as a function of the saturation parameter s at the center of the m-CBS beam. Note that we used the same definition for the contrast of CBS as we did for m-CBS before. The CBS data with strontium atoms from [11] have been obtained with a probe beam on resonance, and exhibit almost the maximum CBS contrast of 1 in the low saturation regime. CBS was also reported with rubidium atoms which, due to their nontrivial internal structure, exhibit an overall lower contrast, even at low saturation parameter [8]. We have chosen, then, to present normalized values of the contrast for CBS rubidium data. Note that in order to observe CBS, a high optical thickness ($b > 1$) is necessary to reach a significant contrast, whereas in the m-CBS setup, the maximum contrast is achieved at low optical densities.

V. DISCUSSION AND CONCLUSION

The comparison between CBS and m-CBS data shows a completely different scaling for the contrast as a function of the saturation parameter. The m-CBS contrast follows the same scaling that we would expect from our model including elastic and inelastic scattering, allowing us to conclude that all photons contribute to m-CBS, whereas CBS interference is severely reduced in the presence of inelastic scattering. The remaining small discrepancy between theory and experiment might be explained by at least two different effects. The

first one is the small, but nonzero, optical thickness of our cloud ($b \sim 0.6$ at its center). At small saturation parameters, the partial reabsorption of the fluorescence light by other atoms from the cloud will change the relative amplitude of the paths of Fig. 1 that have otherwise equal amplitude, thus reducing the overall contrast. This is responsible for the large discrepancy between experimental data and the inelastic theoretical curve at small s. On the other hand, at high saturation parameters the spectral broadening of the atomic fluorescence (known as the Mollow triplet) may also reduce the m-CBS contrast, which is not accounted for in our model. The spectrum of inelastically scattered photons from a resonant probe beam presents sidebands displaced by $\pm\Omega_0$ from the atomic resonance [28]. Since the optical path for the light scattered by the atoms is different from the optical path for the light scattered by their mirror images by twice the distance from the atomic cloud to the real mirror ($\Delta l \approx 1.2$ m in our case), the inelastic broadening will cause a relative dephasing between both when the spectral width becomes comparable to, or bigger than, $(2\pi)c/\Delta l \approx (2\pi)250$ MHz. For our highest experimental saturation parameter $s = 20$, the separation in frequency between the Mollow sidebands is equal to $2\Omega_0 = 2\sqrt{s}\,\Gamma \sim (2\pi)273$ MHz, so the loss of optical coherence in the interference process is already expected to affect the m-CBS contrast. The role of the inelastic spectral broadening in the interference of the light emitted by the atoms and their mirror images will be studied in a future work.

In conclusion, we have observed coherent backscattering from a cloud of cold atoms and its mirror image. Investigating the saturated regime allowed us to identify the important contribution of inelastic photons to the interference process, at odds with CBS. Because this coherence effect appears in completely different regimes as compared to CBS, such as low optical densities and high saturation parameters, it can represent a very important tool for probing coherences in the atomic scattered light where CBS is not observable anymore. In particular, by an appropriate use of waveplates and different polarization channels, the m-CBS setup should allow us to select specific interference paths, which is not possible for CBS. More generally, the atom and its mirror image are strongly correlated, which allows this situation to probe nonclassical light effects [29–33].

ACKNOWLEDGMENTS

We appreciate helpful insights from Thibaut Jonckheere and Dominique Delande. We thank William Guérin for his critical reading of the manuscript. This work has received financial support from FAPESP, CNPq (PVE 400228/2014-9), and CAPES Brazilian agencies.

APPENDIX A: DATA ANALYSIS: SUBTRACTION OF THE LASER LIGHT

As described in the main text, at each experimental run we obtain two images: The first one is registered while the m-CBS beam impinges on the atomic cloud, and the second one is done in the same conditions, but with no atoms captured in our trap. The m-CBS reflected beam, after traversing all optical elements, creates an angular light profile on directions close to its propagation direction. The image registered in absence of atoms shows exclusively this light pattern. The image with atoms has this pattern superposed to the atomic fluorescence, that we want to extract. All the difficulty in extracting it stems from the fact that when the atoms are also present, the m-CBS beam is partially absorbed by them, which results in a smaller signal on the camera when compared to its effect without absorption. We can thus write the azimuthal-averaged profile of the light intensity in the presence of atoms as

$$I_a(\theta) = T\, I_{\rm las}(\theta) + I_f(\theta), \tag{A1}$$

where $T = e^{-2b}$ stands for the average transmission of the cloud after the double passage of the reflected m-CBS beam, and $I_{\rm las}$ and I_f for, respectively, the intensity of the laser light in the absence of atoms, and the intensity of the atomic fluorescence only. From $I_f(\theta)$, the absolute contrast can thus be extracted. Out of the fringes' envelope (or, to a good approximation, for $|\theta - \theta_0| > 2\Phi$), and since we are monitoring the intensity in a narrow angle of 10 mrad, the fluorescence background is isotropic to an excellent approximation. We can write then

$$I_a(\theta, |\theta - \theta_0| > 2\Phi) = T\, I_{\rm las}(\theta) + I_{\rm fluo}, \tag{A2}$$

where $I_{\rm fluo}$ is the constant incoherent atomic background. Then the laser light profile is determined by finding the linear combination of $I_a(\theta)$ (measured with the atoms) and $I_{\rm las}(\theta)$ (measured without the atoms) that satisfies Eq. (A2) outside of the fringes region. An example is provided in Fig. 6(a), where the measured intensity profile with and without the atoms is presented, as well as the extracted atomic fluorescence. Figures 6(b) and 6(c) show the fitted parameters T and $I_{\rm fluo}$, respectively, as a function of the saturation parameter s at the

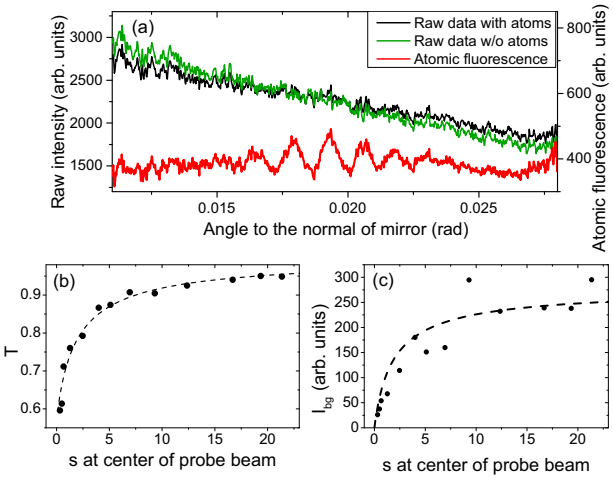

FIG. 6. (a) Angular intensity profile in the presence (middle black curve) and in the absence [top green (gray) curve] of the atomic cloud. The deduced atomic fluorescence after the laser light weighted subtraction (see text) $I_f(\theta)$ [lower red (gray) curve, right vertical axis] presents a locally isotropic background, plus an interference pattern at the center. (b) Transmission coefficient T and (c) background intensity $I_{\rm fluo}$ deduced from the fit [see Eq. (A2) and the main text], as a function of the on-axis saturation parameter s. The dashed curves are calculated with a simple model for the interaction between our saturated Gaussian laser beam and our Gaussian atomic cloud.

center of the atomic beam (black circles). The dashed lines correspond to a simple model for the interaction between our saturated Gaussian laser beam and our Gaussian shaped atomic cloud, with the optical density at the center as the only free parameter. The good agreement gives us confidence in the fitting procedure for extracting the pure atomic fluorescence out of our raw data.

APPENDIX B: SINGLE-SCATTERING THEORY

In the following we outline the theoretical approach used to obtain the radiated intensity pattern in the linear and saturated regimes. Since we are focusing on the single scattering regime, it is sufficient to study the behavior of single atoms, and then sum their radiation independently. Let us thus consider a two-level atom at position $\mathbf{r} = (x,y,z)$ driven by a field of wave vector $\mathbf{k}_0 = k(0, \sin\theta_0, -\cos\theta_0)$.

Without loss of generality, we assume that the (virtual) dielectric mirror lies in the plane $z = 0$ and choose the initial polarization along the $\hat{\mathbf{x}}$ axis. The incident field plus its mirror generate a standing wave in the z axis and a propagating one in the y direction:

$$\Omega(\mathbf{r}) = \Omega_0 \cos(kz\cos\theta_0)e^{-iky\sin\theta_0}. \tag{B1}$$

Note that we have here assumed high quality mirrors that possess unity reflection coefficients.

The single-atom equations are then used to determine the radiation of each atom. Calling σ, $\sigma^\dagger$, and σ^z the atomic operators, in the semiclassical limit the atomic dynamics is described by the following set of equations [34]:

$$\frac{d\hat{\sigma}}{dt} = \left(i\Delta - \frac{\Gamma}{2}\right)\hat{\sigma} + i\Omega(\mathbf{r})\hat{\sigma}^z, \tag{B2}$$

$$\frac{d\hat{\sigma}^z}{dt} = 2i[\Omega^*(\mathbf{r})\hat{\sigma} - \Omega(\mathbf{r})\hat{\sigma}^\dagger] - \Gamma(\hat{\sigma}^z + 1), \tag{B3}$$

with the commutation relations $[\hat{\sigma},\hat{\sigma}^z] = 2\hat{\sigma}, [\hat{\sigma}^\dagger,\hat{\sigma}] = \hat{\sigma}^z$, and $\hat{\sigma}^z\hat{\sigma} = -\hat{\sigma}$.

By imposing the time derivatives to be zero, one obtains the steady state (ss) expectation values of the optical coherence and excited population for an atom at position $\mathbf{r}$:

$$\langle\hat{\sigma}\rangle_{ss}(\mathbf{r}) = \frac{\Delta^2 + \Gamma^2/4}{\Delta + i\Gamma/2}\frac{\Omega(\mathbf{r})}{\Delta^2 + \Gamma^2/4 + 2|\Omega(\mathbf{r})|^2}, \tag{B4}$$

$$\langle\hat{\sigma}^\dagger\hat{\sigma}\rangle_{ss}(\mathbf{r}) = \frac{|\Omega(\mathbf{r})|^2}{\Delta^2 + \Gamma^2/4 + 2|\Omega(\mathbf{r})|^2}. \tag{B5}$$

In the far field limit, the field radiated by a single atom in a direction $\mathbf{k} = k\hat{\mathbf{n}}$ and at a distance r reads [35]

$$\hat{\mathbf{E}}(\mathbf{k},t) = -\hat{\sigma}(t)\frac{dk^2}{4\pi\epsilon_0 r}[\hat{\mathbf{n}}(\hat{\mathbf{x}}\cdot\hat{\mathbf{n}}) - \hat{\mathbf{x}}]e^{-i\mathbf{k}\cdot\mathbf{r}}, \tag{B6}$$

where d refers to the dipole coupling element and ϵ_0 to the vacuum permittivity.

The measured field in the m-CBS experiment actually contains two contributions from each atom, since the radiation of the latter may be reflected or not by the mirror [see Fig. 1, with processes (i) and (iv) that yield mirror reflection after scattering]. Thus the total scattered electric field $\mathbf{E}_s$ in a direction $\mathbf{k}$ comes from the superposition

$$\mathbf{E}_s(\mathbf{k}) = \mathbf{E}(k_x,k_y,k_z) + \mathbf{E}(k_x,k_y,-k_z). \tag{B7}$$

In general, the different components of the field may play an important role in the intensity profile. However, our experiment was carried out within observation angles $\theta \ll 1$, where only the E_x component is significant. Hence we obtain for the steady-state fields the following expression:

$$\langle E_s\rangle \sim \sqrt{\alpha}\langle\sigma\rangle_{ss}\cos(kz\cos\theta)e^{-ik_y y - ik_x x}, \tag{B8}$$

$$\langle E_s^\dagger E_s\rangle \sim \alpha\langle\sigma^\dagger\sigma\rangle_{ss}\cos^2(kz\cos\theta), \tag{B9}$$

where the prefactor $\alpha = d^2k^4/(4\pi^2\epsilon_0^2 r^2)$ is unimportant to the determination of the contrast. Equation (B8) corresponds to the optical coherence, and thus to the *elastically scattered* light. On the contrary Eq. (B9) describes the *total* intensity, that is, both elastic and inelastic photons [34].

Moving to the m-CBS by a macroscopic cloud of N atoms with positions $\mathbf{r}_j$, the radiation pattern is computed as the sum of the single-atom intensities:

$$\frac{I_{\rm tot}}{I_0} = \frac{4s}{N}\sum_{j=1}^{N}\frac{\cos^2(kz_j\cos\theta_0)\cos^2(kz_j\cos\theta)}{1 + s\cos^2(kz_j\cos\theta_0)}, \tag{B10}$$

where we have introduced the saturation parameter $s = 2\Omega_0^2/(\Delta^2 + \Gamma^2/4)$ and $I_0 = c\epsilon_0 N\alpha/8$. Equation (B10) relies on the simplifying hypothesis that all the scattered light (elastic *and* inelastic) has the same phase after the scattering, at any time. More precisely, the coherence length of the light is much larger than the distance between the (real) mirror and the cloud, so the inelasticity of the photons may not play a role. We note that, in the case of a uniform intensity distribution of the laser beam, the spatial distribution of the atoms in the plane of the mirror (x,y) does not play any role in this setup.

Nevertheless, if one was to assume that only elastically scattered light contributes to the fringes pattern, the following expression for the intensity would be obtained:

$$\frac{I_{\rm ela}}{I_0} = \frac{4s}{N}\sum_{j=1}^{N}\frac{\cos^2(kz_j\cos\theta_0)\cos^2(kz_j\cos\theta)}{[1 + s\cos^2(kz_j\cos\theta_0)]^2}. \tag{B11}$$

Let us first focus on the linear regime, which is that of elastic scattering ($I_{\rm tot} \approx I_{\rm ela}$), and that is obtained by taking $s \ll 1$. We obtain the following expression for the microscopic system:

$$\frac{I_{\rm ela}(\theta)}{I_0} \approx \frac{s}{N}\sum_{j=1}^{N}\{\cos[kz_j(\cos\theta - \cos\theta_0)] + \cos[kz_j(\cos\theta + \cos\theta_0)]\}^2. \tag{B12}$$

At this point it must be noted that a single atom will exhibit full contrast, with fringes that are not damped. However, in the many-body case, the superposition of atoms with different fringes phase (see Fig. 4) results in an interference pattern with a reduced contrast, over a finite envelope. This sum over a macroscopic cloud (i.e., much larger than the wavelength) is well captured by substituting the sum over the atoms by an integral over the typical atomic distribution $\sum_{j=1}^{N} \to \int d\mathbf{r}\rho(\mathbf{r})$. The first term in the sum in Eq. (B12) provides a *coherent* contribution in the $\theta = \theta_0$ direction, whatever the

position z of the atom, whereas the second term averages to 0. The decay of the envelope is then provided by the finite size of the cloud. For a Gaussian distribution such as those produced in our trap, one obtains Eq. (1). That equation predicts an alternation of constructive and destructive interferences with period $\pi/(kh\theta_0)$, which leads to the observed fringes, see Fig. 7.

Remark that the elastic contribution Eq. (B11) decreases as $1/s$ for increasing saturation parameter s, whereas the total radiation converges to

$$\lim_{s\to\infty} \frac{I_{\rm tot}(\theta)}{I_0} = \frac{4}{N}\sum_{j=1}^{N} \cos^2(kz_j\cos\theta). \qquad \text{(B13)}$$

Integrating over a Gaussian distribution as before, in the small angle and large cloud limits, we obtain $I_{\rm tot} = 2I_0$, i.e., the fluorescence converges to a finite value for very large saturation parameters. Thus the ratio between the elastically scattered intensity to the total one scales as $1/s$, which explains the fast decay of the contrast of the "elastic" theory.

In the saturated regime, atoms that are not close to a zero of the standing wave saturate. As s increases, the proportion of scatterers that contribute to the grating decreases as $1/\sqrt{s}$, whereas the others produce an isotropic fluorescence radiation pattern. This explains the rather slow decay of the contrast in the "inelastic theory." In the present work, the intensity pattern for large values of s was computed numerically using the microscopic formula (B10), for random Gaussian distributions of one hundred thousands of atoms (see Fig. 5).

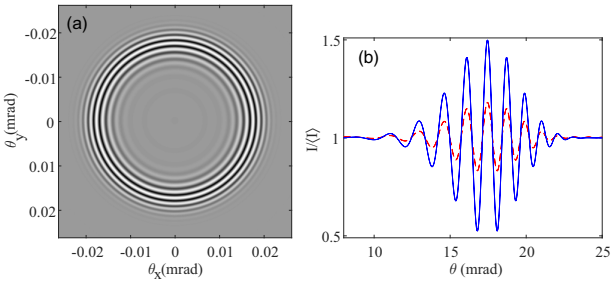

FIG. 7. (a) Intensity pattern in the nonlinear regime [Eq. (B10)], with $s = 20$. The intensity pattern in the linear regime is virtually identical, up to a scaling factor. (b) Azimuthal average of the intensity pattern normalized to the background intensity, in the linear ($s = 0.01$, blue continuous line) and nonlinear ($s = 20$, red dashed line) regimes, showing the fringes profile. The figures can be compared to the measurement presented in Fig. 2 of the main text.

[1] Y. Kuga and A. Ishimaru, J. Opt. Soc. Am. A **1**, 831 (1984).
[2] M. P. Van Albada and A. Lagendijk, Phys. Rev. Lett. **55**, 2692 (1985).
[3] P.-E. Wolf and G. Maret, Phys. Rev. Lett. **55**, 2696 (1985).
[4] D. S. Wiersma, M. P. van Albada, B. A. van Tiggelen, and A. Lagendijk, Phys. Rev. Lett. **74**, 4193 (1995).
[5] K. M. Yoo, G. C. Tang, and R. R. Alfano, Appl. Opt. **29**, 3237 (1990).
[6] M. I. Mishchenko, Astrophys. J. **411**, 351 (1993).
[7] A. Tourin, A. Derode, P. Roux, B. A. van Tiggelen, and M. Fink, Phys. Rev. Lett. **79**, 3637 (1997).
[8] G. Labeyrie, F. de Tomasi, J.-C. Bernard, C. A. Müller, C. Miniatura, and R. Kaiser, Phys. Rev. Lett. **83**, 5266 (1999).
[9] Y. Bidel, B. Klappauf, J. C. Bernard, D. Delande, G. Labeyrie, C. Miniatura, D. Wilkowski, and R. Kaiser, Phys. Rev. Lett. **88**, 203902 (2002).
[10] D. V. Kupriyanov, I. M. Sokolov, P. Kulatunga, C. I. Sukenik, and M. D. Havey, Phys. Rev. A **67**, 013814 (2003).
[11] T. Chanelière, D. Wilkowski, Y. Bidel, R. Kaiser, and C. Miniatura, Phys. Rev. E **70**, 036602 (2004).
[12] D. V. Kupriyanov, I. M. Sokolov, C. I. Sukenik, and M. D. Havey, Laser Phys. Lett. **3**, 223 (2006).
[13] T. Wellens, B. Grémaud, D. Delande, and C. Miniatura, Phys. Rev. A **70**, 023817 (2004).
[14] T. Jonckheere, C. A. Müller, R. Kaiser, C. Miniatura, and D. Delande, Phys. Rev. Lett. **85**, 4269 (2000).
[15] G. Labeyrie, Mod. Phys. Lett. **22**, 73 (2008).
[16] K. Totsuka and M. Tomita, Phys. Rev. B **59**, 11139 (1999).
[17] T. Wellens, B. Grémaud, D. Delande, and C. Miniatura, Phys. Rev. E **71**, 055603 (2005).
[18] S. Balik, P. Kulatunga, C. I. Sukenik, M. D. Havey, D. V. Kupriyanov, and I. M. Sokolov, J. Mod. Opt. **52**, 2269 (2005).
[19] V. Shatokhin, C. A. Müller, and A. Buchleitner, Phys. Rev. Lett. **94**, 043603 (2005).
[20] B. Grémaud, Th. Wellens, D. Delande, and Ch. Miniatura, Phys. Rev. A **74**, 033808 (2006).
[21] T. Wellens, B. Grémaud, D. Delande, and C. Miniatura, Phys. Rev. A **73**, 013802 (2006).
[22] J. R. Ott, M. Wubs, P. Lodahl, N. A. Mortensen, and R. Kaiser, Phys. Rev. A **87**, 061801(R) (2013).
[23] A. Ketterer, A. Buchleitner, and V. N. Shatokhin, Phys. Rev. A **90**, 053839 (2014).
[24] J.-J. Greffet, Waves Random Media **1**, S65 (1991).
[25] G. Labeyrie, C. A. Müller, D. S. Wiersma, C. Miniatura, and R. Kaiser, J. Opt. B **2**, 672 (2000).
[26] E. Ciaramella, M. Tamburrini, and E. Santamato, Appl. Phys. Lett. **63**, 1604 (1993).
[27] G. Labeyrie *et al.*, Nat. Photon. **8**, 321 (2014).
[28] B. R. Mollow, Phys. Rev. **188**, 1969 (1969).
[29] I. Steiner and P. E. Toschek, Phys. Rev. Lett. **74**, 4639 (1995).
[30] J. Eschner, Ch. Raab, F. Schmidt-Kaler, and R. Blatt, Nature (London) **413**, 495 (2001).
[31] M. A. Wilson, P. Bushev, J. Eschner, F. Schmidt-Kaler, C. Becher, R. Blatt, and U. Dorner, Phys. Rev. Lett. **91**, 213602 (2003).
[32] G. Hetet, L. Slodicka, M. Hennrich, and R. Blatt, Phys. Rev. Lett. **107**, 133002 (2011).
[33] I.-C. Hoi, A. F. Kockum, L. Tornberg *et al.*, Nat. Phys. **11**, 1045 (2015)
[34] M. O. Scully and M. S. Zubairy, *Quantum Optics* (Cambridge University Press, Cambridge, 1997).
[35] T. Bienaime, M. Petruzzo, D. Bigerni, N. Piovella, and R. Kaiser, J. Mod. Opt. **58**, 1942 (2011).

4 OPTICAL BINDING WITH COLD ATOMS

4.1 Same text of the paper preview in letter format

The interaction of light with atoms, from the microscopic to the macroscopic scale, is one of the most fundamental mechanisms in nature. After the advent of the laser, new techniques were developed to manipulate precisely objects of very different sizes with light, up to the atomic scale. In this context, two optical forces are of fundamental importance: The radiation pressure force, which pushes the particles in the direction of the light propagation,[60] and the dipole force, which tends to trap them into intensity extrema, as for example in optical lattices.[61] Beyond single-particle physics, one must consider that the multiple scattering of light plays an important role in modifying these forces. For instance, the radiation pressure force compresses optically thick atomic clouds, as a result of intensity attenuation in the propagation direction,[62] whereas the dipole force can be self-induced as plane-wave waves suffer diffraction on the scatterers, for example on matter waves.[63]

In a many-scatterer system, multiple scattering results in mutual optical forces between all of them: These forces in turn may promote long-range spatial reorganization of the system in regions of the order of the light wavelength, an effect called Optical Binding (OB).[64] Since the first OB demonstrations,[65,66] experiments have been realized with pairs of dielectric microsized-spheres interacting with intense light fields within dissipative fluids, the bistability properties of one-dimensional configurations were studied[67] and optically restoring forces were demonstrated.[68] Theoretical approaches have focused on the one-[69] (1D) and two-dimensional[70,71] (2D) stability of spheres arrays, using numerically approaches. In particular, the existence of a friction threshold above which bounded motion occurs was discussed in Ref.[72]

In this letter, we demonstrate theoretically the existence of optically bounded motion for a pair of cold atoms in the absence of non-radiative friction. The two atoms are confined in 2D by counterpropagating lasers, and the resulting undamped angular momentum becomes a conserved quantity. This system allows for the study of rotating bound states rotation, and their dynamical stability properties. Thus, we identify an unbound-bound phase transition as the pump strength and laser-atomic transition detuning are tuned, which has the particularities to be asymmetric with respect to the atomic transition: Red-detuned states exhibit pure OB, whereas blue-detuned one present only metastable OB, with a stability time that grows exponentially with the detuning.

Our system is composed of two non-relativistic atoms of mass m which interact with a classical radiation field. Using the the dipole approximation $H = -\sum_{j=1}^{2} \mathbf{D}_j \cdot \mathbf{E}(\mathbf{r}_j)$,

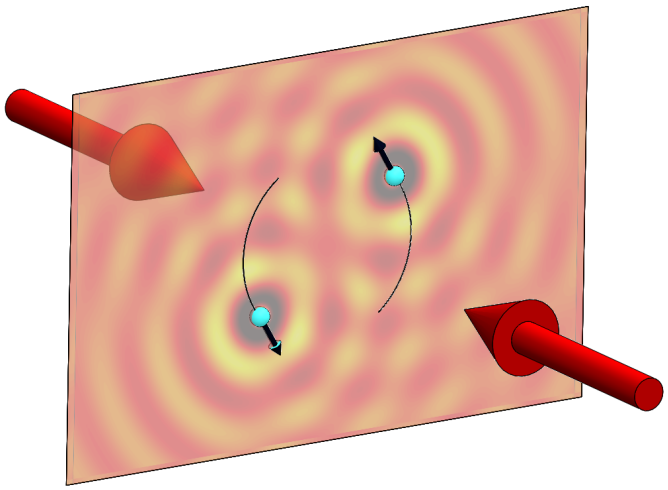

Figure 3 – Two atoms evolve in the $z = 0$ plane, trapped in 2D by counter-propagating plane-waves, with wave vector orthogonal to that plane. The light exchange between the atoms induces the 2D two-body optically coupled dynamics.

Source: By the author.

with $\mathbf{D}_j$ the dipole operator and $\mathbf{E}(\mathbf{r}_j)$ the electric field calculated at the center-of-mass $\mathbf{r}_j$ of the atoms. The Hamiltonian H is valid when the light wavelength is much larger than the atom size, so the center-of-mass motion of the atoms can be described rightly by classical trajectories. Considering the scalar linear optics regime,[33] the Heisenberg equations of motion for the dipoles leads to the classical analogue

$$\dot{\beta}_j = \left(i\Delta - \frac{\Gamma}{2}\right)\beta_j - i\Omega - \frac{\Gamma}{2}G\left(|\mathbf{r}_j - \mathbf{r}_l|\right)\beta_l, \tag{4.1}$$

$$\ddot{\mathbf{r}}_j = -\frac{\hbar\Gamma}{m}\mathrm{Im}\left[\nabla_{\mathbf{r}_j}G\left(|\mathbf{r}_j - \mathbf{r}_l|\right)\beta_j^*\beta_l\right], \quad l \neq j, \tag{4.2}$$

which can be also derived from the standard Maxwell equations.[26,27] Two counter-propagating plane waves, of Rabi frequency Ω and wavenumber k, drive two-level transitions, of linewidth Γ and detuning Δ between the laser frequency and the atomic transition. As these lasers trap the two atoms in a field maximum plane ($z = 0$), which is perpendicular to the light propagation, the laser cooling process plays no role in the z direction (see Fig.3). Therefore, a frictionless 2D motion emerges, where the only dissipation present is the spontaneous emission from the dipoles into the vacuum modes (see Eq.(4.1)). Note that while the dipoles probability amplitude β_j respond linearly to the light fields, their coupling with the centers-of-mass $\mathbf{r}_j$ is responsible for the nonlinearity of Eqs.(4.1)–(4.2).

The light-mediated long-range interaction between the atoms is given, in the scalar light approximation, by the Green function

$$G\left(|\mathbf{r}_j - \mathbf{r}_l|\right) = \frac{e^{ik|\mathbf{r}_j - \mathbf{r}_l|}}{ik\,|\mathbf{r}_j - \mathbf{r}_l|}, \tag{4.3}$$

which is obtained from the Markovian integration over the vacuum modes of the electromagnetic field.[33] The gradient of the modulus of G is responsible for the radial dipolar force between the atoms, whereas the gradient of its phase gives rise to the radiation pressure force.[60] This coupled dipole model, has been shown to provide an accurate description of many phenomena based on cooperative light scattering, such as the observation of a cooperative radiation pressure force,[28,29] superradiance[30] and subradiance[15] in dilute atomic clouds, linewidth broadening and cooperative frequency shifts.[31,79]

Central force problems, as the one described by Eqs.(4.1)-(4.2), are best studied in the relative coordinate frame, so we define the average (and differential) positions and dipoles of the atoms (see Supp. Mat.). After a transient of order $1/\Gamma$, the two atomic dipoles synchronize and their relative position $\mathbf{r} = \mathbf{r}_1 - \mathbf{r}_2$ gets coupled only to the average dipole, i.e., the center-of-mass motion and the dipoles difference play no role in this setup. The angular momentum $L = mrv_\perp$ of the system is a conserved quantity, with $v_\perp$ the magnitude of the velocity perpendicular to the inter-particle separation $\mathbf{r} = r\hat{\mathbf{r}}$. This is a fundamental difference with other OB systems where the angular momentum is quickly driven to zero by friction. Note that the stochastic heating due to the random atomic recoil which comes from spontaneous emission recoils is here neglected.

Bound states (BS) are found around the stable equilibrium points of the system. Here they are given by the zeros of the equation

$$\frac{\ell^2}{k^3 r^3} = \frac{\Omega^2}{\Gamma^2} \frac{\frac{\sin kr}{kr} + \frac{\cos kr}{k^2 r^2}}{\left(1 + \frac{\sin kr}{kr}\right)^2 + \left(2\delta + \frac{\cos kr}{kr}\right)^2}, \tag{4.4}$$

as derived in the supplemental material. Note that Eq.(4.4) depends on the dimensionless angular momentum $\ell \equiv Lk/\sqrt{8\Gamma m\hbar}$, pump strength Ω/Γ and detuning $\delta \equiv \Delta/\Gamma$, and it includes both stable and unstable equilibrium points. For the particular case $\ell = 0$, the equilibrium points are given by the simplified condition $\tan kr = -1/kr$ which does not depend on the light matter coupling, only on the atoms mutual distance. The details of the light-matter interaction will however come into play when the stability of these equilibrium points is considered.

As pointed out in Ref.,[72] linear stability may not be sufficient to provide a phase diagram with BS. We here instead choose to study its stability by integrating numerically the dynamics, starting with a pair of atoms with initial velocities, and moving around the equilibrium separation $r \approx \lambda$. We first focus on states without angular momentum, so the atoms are chosen with opposite radial velocities $v_\parallel$, parallel to the vector distance between the atoms. The escape time τ, at which the atoms start to evolve as free-particles, is computed by integrating the 1D dynamics.

Fig.4(a) presents the stability diagram of the $r \approx \lambda$ equilibrium point. In the lower part of the diagram (low pump strength), free-particle states are always observed after

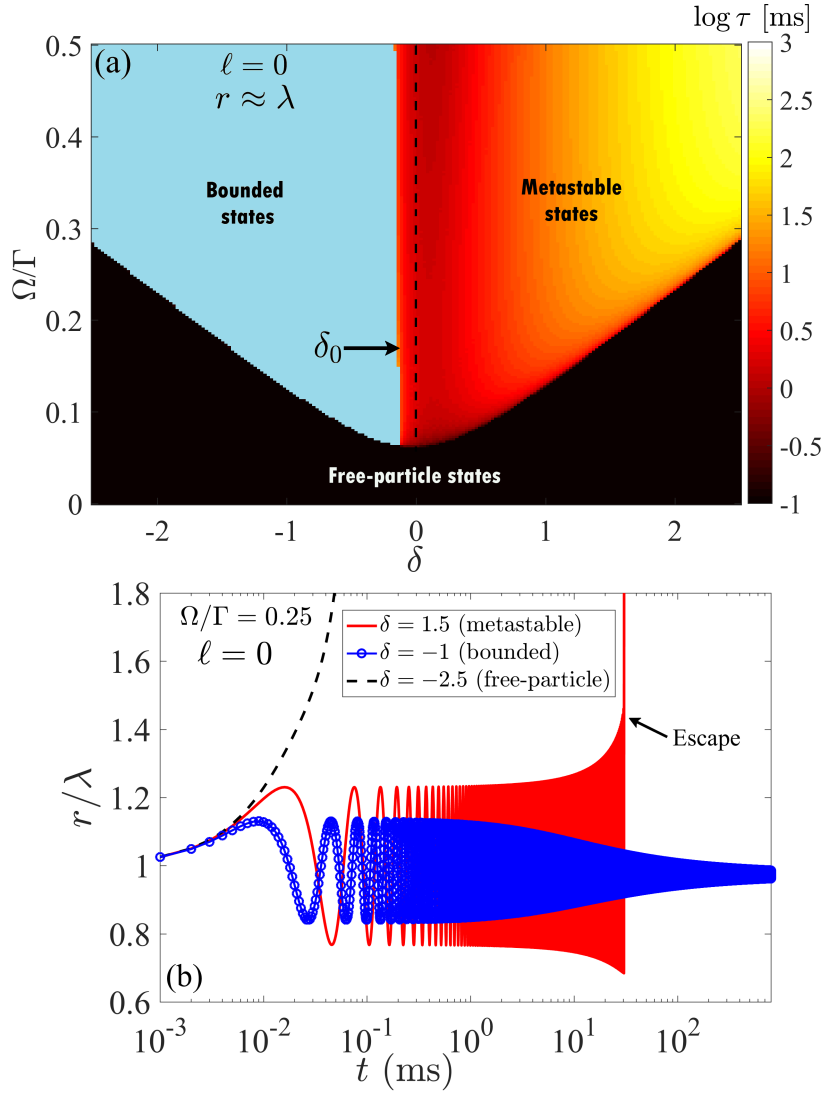

Figure 4 – (a) Stability diagram around the equilibrium point $r \approx \lambda$ for the 1D dynamics with $\ell = 0$. Free-particle states are found for low pump intensity, over the black region, BS on the red-detuned side (light blue area) and metastable states on the blue-detuned side (color gradient). (b) Typical dynamics of of free-particle, bounded and metastable states. Simulations realized with particles with an initial temperature $T = 1\mu K$, where the conversion between temperature and velocity was realized using the ^{87}Rb atom mass $m = 1.419 \times 10^{-25}$ Kg.

Source: By the author.

a short transient $\tau \approx 0.1$ ms, which means that the optical forces are unable to bind the atoms (see trajectory for $\delta = -2.5$ in Fig.4(b)). For δ smaller than a phase shift δ_0 (discussed later), a free-particle to bounded motion phase transition occurs as the pumping strength Ω/Γ is increased. In the stable phase (BS), the atoms mutual distance r converges oscillating to $r \approx \lambda$, as displayed in the circles curve of Fig.4(b). We verified that these BS, characterized by an infinite τ, occur around the equilibrium points $r = n\lambda$, with

$n \in \mathbb{N}$. The unstable equilibrium points are found around $(n + 1/2)\lambda$ and contains only free-particle states (see supp. mat.).

For $\delta > \delta_0$, a free-particle to BS phase transition occurs as well, symmetric to the previous one (see Fig.4(a)). Yet the BSs appear to be only metastable, with the pair of atoms which separates on large time scales (see Fig.4(b)). The binding time is indeed observed to grow exponentially with the normalized detuning δ, reaching milliseconds for a few units of Γ already. This is different from the previous works on dielectric spheres, which have reported on detuning-symmetric situations.[64]

Studying the conditions of existence of BS, we identified that the transition from the free-particle to BS is characterized by the following scaling law (see Suppl. Mat. for more details)

$$\frac{T_c}{T_{rec}} \approx \alpha \frac{\Omega^2}{\Delta^\beta} \frac{1}{(kr)^{0.9}}, \tag{4.5}$$

with $\alpha \approx 58.997 \pm 2.3\%$, $\beta \approx 2.004 \pm 1.1\%$ and $T_{rec} = \hbar^2 k^2 / 2mk_B$ the recoil temperature. This law represents a cooperative correction to the optical potential barrier which can be estimated for large detunings, as done for dielectrics.[65] Note that in the present case, the temperature scales as $1/\Delta^2$, rather than $1/\Delta^4$ as for dielectrics: This important difference originates in the fact that two-atom OB relies on double scattering instead of the usual dipole force.[80] Note that here, since we are considering at first a zero angular motion dynamics, the temperature is associated to the parallel (radial) velocity of the two atoms ($k_B T = m\langle v_\parallel^2 \rangle$), where the ^{87}Rb atom mass was used.

The free-particle to BS transition in Fig.4(a) is approximately delimited by a shift δ_0, which is composed of two terms. First, considering that the atoms separation is almost constant for a given BS ($r \approx \lambda$ in Fig.4(b), for example), the state composed of two synchronized dipoles has an energy $\cos(kr)/2kr$ (see supp. mat.). The second contribution comes from the average Doppler shift

$$\delta_0 \approx -\frac{\cos kr}{2kr} - \frac{k v_\parallel(\tau)}{\Gamma}. \tag{4.6}$$

The first term of Eq. (4.6) represents a cooperative energy shift that depends on the atoms separation r and, the second term, is the Doppler shift due to the atoms free-particle separation velocity $v_\parallel(\tau)$. Therefore, this shift precludes BS from the resonance line when the angular momentum is absent.

The frictionless nature of the cold atom system introduces a new degree of freedom. As mentioned earlier, the angular momentum l is conserved during the dynamics, which gives rise to rotating BS. Examples of such states are shown in Fig.5: The pair of atoms can reach a rotating BS with fixed inter-particle distance on resonance (see Figs.5 (a) and (b)), but it may also support stable oscillations along the two-atom axis far from resonance (see Figs.5 (c) and (d)), analogue to a molecule vibrational mode. As in the 1D case, the

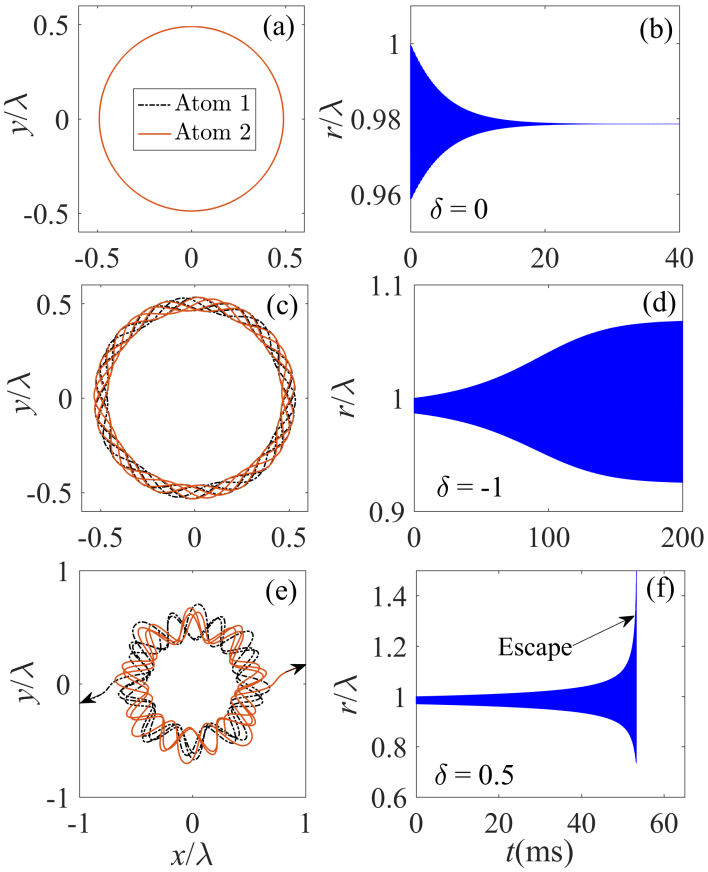

Figure 5 – Rotating states for the pair of atoms for (a–b) Fixed inter-particle distance, (c–d) Vibrational mode and (e–f) Metastable state. As the orbits of both atoms coincides in (a), only a single orbit appears displayed. Simulations realized with $\ell = 0.13$, $\Omega/\Gamma = 0.25$ and $T = 1\mu K$, where the ^{87}Rb atom mass was adopted.

Source: By the author.

atoms may remain coupled for long times, before eventually separating (see Figs.5 (e) and (f)). As can be seen in Eq.(4.4), for $\ell \neq 0$ the stationary points are circular orbits in the plane $z = 0$ instead of fixed points, which now depend on all control parameters (see Eq. (4.4)).

High values of angular momentum ℓ strongly modifies the equilibrium point landscape, suppressing the low-r equilibrium points (see Suppl. Mat.). Considering as before the $r \approx \lambda$ equilibrium point, with an initial temperature $T = 1\mu K$ which is now associated to a transverse initial velocity, we obtain $\ell \approx 0.13$. This value presents an equilibrium landscape mostly unchanged, although the stability of these points may be altered, so we proceed on comparing the associated phase diagram to that of the $l = 0$ case.

Rotating BS are characterized by both radial $v_{\parallel}$ and tangential $v_{\perp}$ velocities, the latter being associated to the conserved angular momentum. For simplicity, we focus on initial states of atoms with purely tangential and opposite velocities. In other words,

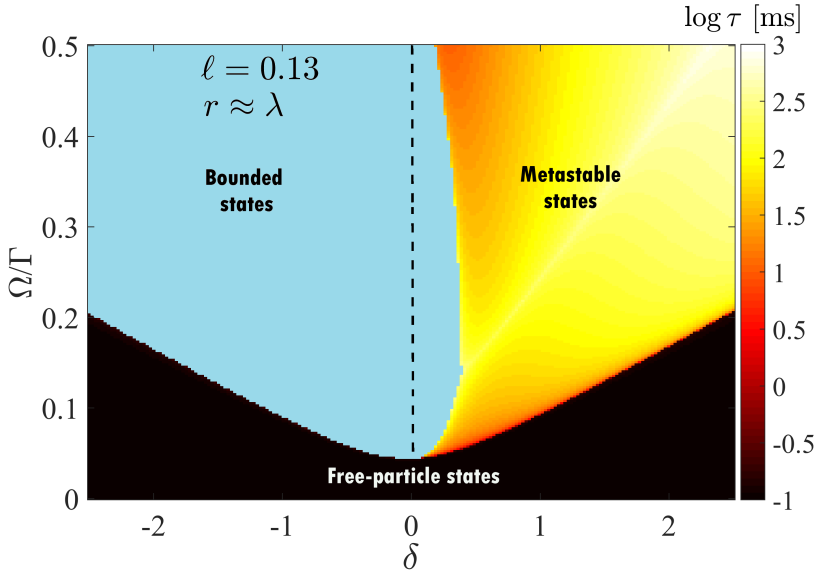

Figure 6 – Stability diagram around the equilibrium point $r \approx \lambda$ for $\ell = 0.13$. Free-particle states are found for low pump intensity (black region), BS on the red-detuned side (light blue) and metastable states in the blue-detuned side, where the color gradient denotes the state lifetime. Simulations realized with particles with an initial temperature $T = 1\mu K$, where the conversion between temperature and velocity was realized using the Rb atom mass.

Source: By the author.

no initial radial velocity is considered, although it may appear dynamically. A phase diagram for the $r \approx \lambda$ and $\ell = 0.13$ states is presented in Fig.6, where the escape time τ has been computed following the same procedure as before. Let us first remark that the purely-bounded to metastable transition is not delimited by a sharp transition anymore, oppositely to the $\ell = 0$ case. For $\ell \neq 0$, this energy shift varies nonlinearly according to the field pump strength Ω/Γ, allowing dynamically stable BS for $\delta > \delta_0$, including the resonant line. The stable-metastable phase transition for $\ell \neq 0$ covers a larger part of the phase diagram, so the introduction of an angular momentum in the system allows to reach BS for ranges of parameters where they do not exist at $\ell = 0$.

Investigating the long-term stability of states with different angular momentum and inter–particle distance, a similar scaling law to that representing the $\ell = 0$ (see Eq.(4.5)) can be obtained,

$$\frac{T_c}{T_{rec}} \approx \alpha \frac{\Omega^2}{\Delta^\beta} \frac{1}{(kr)^{0.2}}, \tag{4.7}$$

with $\alpha \approx 30.687 \pm 1.9\%$ and $\beta \approx 2.003 \pm 0.8\%$, where the temperature is now related to the tangential velocity as $Tk_B = m\langle v_\perp^2 \rangle$. Interestingly, Eq.(4.7) shows that the stability of rotating BS depends little on the inter–particle distance. Moreover, when one compares the diagrams of the $\ell = 0$ and $\ell \neq 0$ cases, it can be clearly noted that the escape time

is significantly larger for rotating BSs, so angular momentum appears to promote the stability of BSs.

In conclusion, we have shown that pairs of cold atoms can exhibit optically BS in vacuum. The absence of non-radiative damping in the motion allows for a new class of dynamically BS – a phenomenon not present in other OB setups. Furthermore, while red-detuned light presents OB above a given threshold, blue-detuned light presents only metastable states, whose lifetime increases with both detuning and angular momentum. While this demonstration of optical binding for a pair of particles paves the way for the study of this phenomenon on larger atomic systems, the generalization of these peculiar stability properties will be an important issue to understand the stability of large clouds.

4.2 Supplemental Material

4.2.1 Effective two-dimensional dynamics and cooperative shift

Eqs. (4.1)-(4.2) of the main text can be rewritten in a more convenient form through the following variables transformation:

$$b = \beta_1 - \beta_2, \tag{S-1}$$
$$B = \frac{\beta_1 + \beta_2}{2}, \tag{S-2}$$
$$\mathbf{r} = \mathbf{r}_1 - \mathbf{r}_2, \tag{S-3}$$
$$\mathbf{R} = \frac{\mathbf{r}_1 + \mathbf{r}_2}{2}. \tag{S-4}$$

where B and b are the average and differential dipoles, and R and r the average and differential positions. As the motion is restricted to two dimensions, we choose the polar coordinates parametrization $\mathbf{r} = r\,(\cos\phi, \sin\phi)$, which yields the following dynamical equations:

$$\dot{b} = -\frac{\Gamma}{2}\left[1 - \frac{\sin kr}{kr} - i\left(2\delta - \frac{\cos kr}{kr}\right)\right] b, \tag{S-5}$$
$$\dot{B} = -\frac{\Gamma}{2}\left[1 + \frac{\sin kr}{kr} - i\left(2\delta + \frac{\cos kr}{kr}\right)\right] B - i\Omega, \tag{S-6}$$
$$\ddot{r} = \frac{L^2}{m^2 r^3} - \frac{\Gamma\hbar k}{2m}\left(\frac{\sin kr}{kr} + \frac{\cos kr}{k^2 r^2}\right)\left(4\,|B|^2 - |b|^2\right), \tag{S-7}$$
$$\dot{L} = \frac{d}{dt}\left(mr^2\dot{\phi}\right) = 0, \tag{S-8}$$

where the center-of-mass dynamics of the two-atom system has naturally decoupled from all equations. The cooperative shift $-\cos kr/2kr$ appears clearly in Eq.(S-6), by choosing as zero the imaginary part of the brackets.

4.2.2 Derivation of the equilibrium condition Eq.(4)

As there is no source term Eq.(S-5), the relative dipoles coordinate b vanishes on a time scale of the order of $1/\Gamma$, which is very fast compared to the atomic motion. Therefore, the atoms can be considered always synchronized and the inter-atomic dynamics r couples only to the average dipole B. It is thus possible to write

$$B = \beta_1 = \beta_2 \equiv \beta e^{i\chi}, \tag{S-9}$$

with $\beta \geq 0$ and $\chi \in \mathbb{R}$. Then, the set of dynamical equations reduces to:

$$\dot{\beta} = -\frac{\Gamma}{2}\left(1 + \frac{\sin kr}{kr}\right)\beta - \Omega \sin\chi, \tag{S-10}$$

$$\dot{\chi} = \Delta + \frac{\Gamma}{2}\frac{\cos kr}{kr} - \Omega\frac{\cos\chi}{\beta}, \tag{S-11}$$

$$\ddot{r} = \frac{L^2}{m^2 r^3} - \frac{2\Gamma\hbar k}{m}\left(\frac{\sin kr}{kr} + \frac{\cos kr}{k^2 r^2}\right)\beta^2. \tag{S-12}$$

The equilibrium points of these equations will be given by setting $\dot{\beta} = \dot{\chi} = 0$:

$$\beta_0 = 2\frac{\Omega}{\Gamma}\left[\left(1 + \frac{\sin kr}{kr}\right)^2 + \left(2\delta + \frac{\cos kr}{kr}\right)^2\right]^{-\frac{1}{2}}, \tag{S-13}$$

$$\chi_0 = \arctan\left(-\frac{1 + \frac{\sin kr}{kr}}{2\delta + \frac{\cos kr}{kr}}\right). \tag{S-14}$$

which, combined with $\ddot{r} = 0$, gives the equilibrium condition for the interatomic separations, Eq.(4.4) in the main text. If one redefines Eq.(4.4) as

$$F \equiv \frac{\ell^2}{k^3 r^3} - \frac{\Omega^2}{\Gamma^2}\frac{\frac{\sin kr}{kr} + \frac{\cos kr}{k^2 r^2}}{\left(1 + \frac{\sin kr}{kr}\right)^2 + \left(2\delta + \frac{\cos kr}{kr}\right)^2}, \tag{S-15}$$

the equilibrium points are obtained from the zeros of F (see Fig.7). In Fig.7(a), observe that as the angular momentum increases, the equilibrium points with the shortest distances become more shallow, before disappearing.

4.2.3 Unstable equilibrium point

In Fig.8, we present a complementary example of an unstable equilibrium separation around $r \approx 3\lambda/2$. It contains always free-particle states whose escape time converge to $\tau \approx 10^{-1.2}$ ms ≈ 0.06 ms as the detuning increases. The diagram with angular momentum converges faster to this maximum τ with detuning than the unidimensional case and no phase transitions were found.

4.2.4 Collapse of the temperature threshold

The unbounded-bounded motion phase transition, which is symmetrical to the unstable-metastable one, satisfies the scaling laws of the main text. In order to ground it,

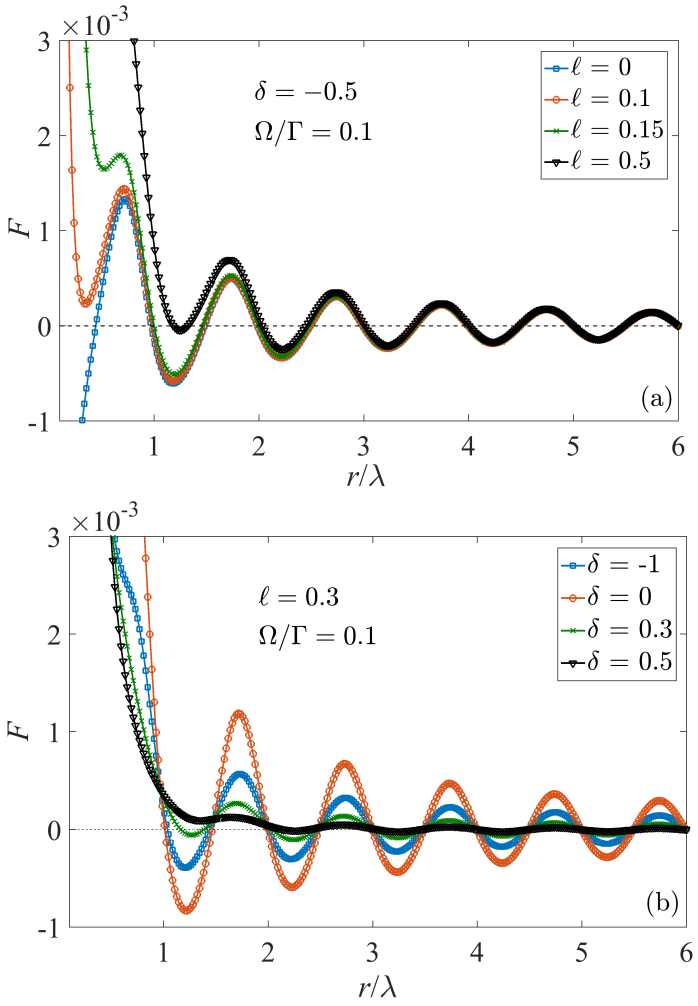

Figure 7 – Two-atoms equilibrium distances (a) for different ℓ and (b) different detunings.

Source: By the author.

we display in Figs.9 and 10 the linear collapse of several curves for both $\ell = 0$ and $\ell \neq 0$ cases.

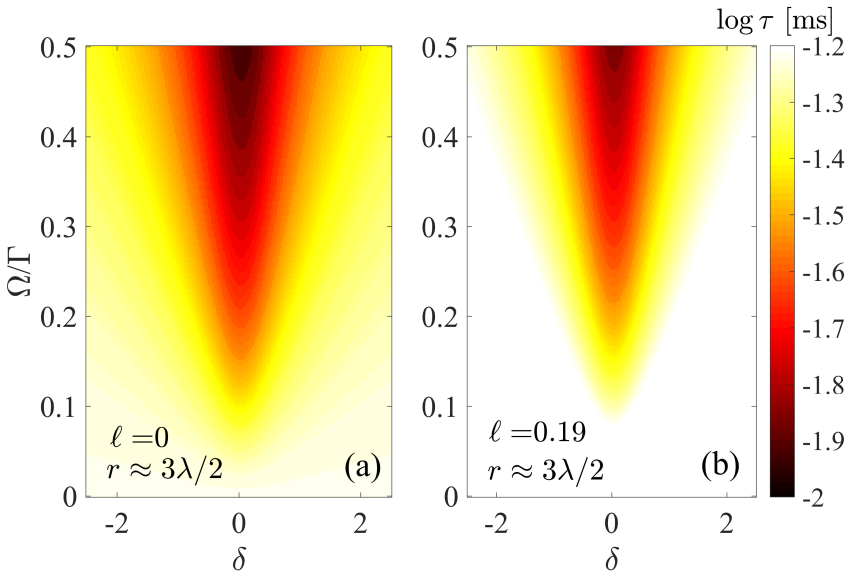

Figure 8 – Stability diagrams for the equilibrium point around $r \approx 3\lambda/2$.

Source: By the author.

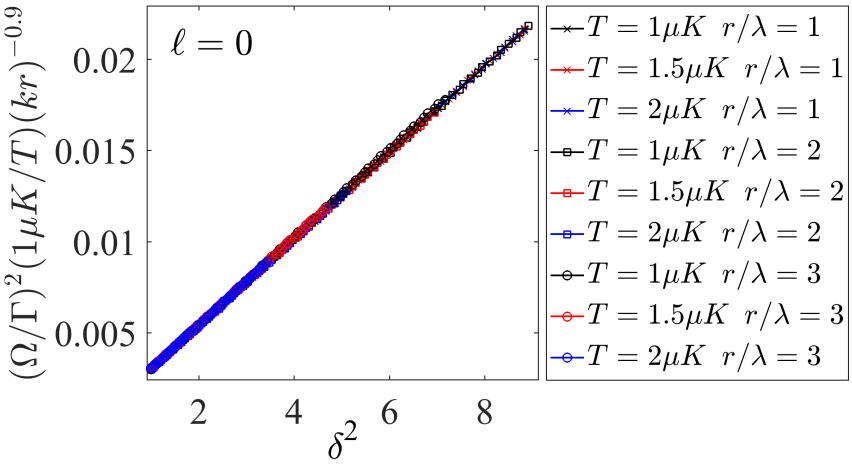

Figure 9 – Collapse of the phase transition slope from free-particle to bounded states for one-dimensional motion ($\ell = 0$).

Source: By the author.

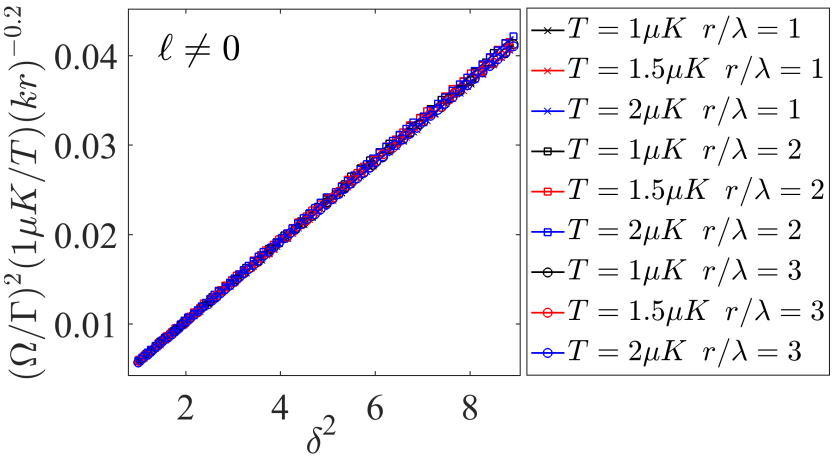

Figure 10 – Collapse of the phase transition slope from free-particle to bounded states for two-dimensional motion ($\ell \neq 0$).

Source: By the author.

5 GENERAL CONCLUSIONS AND FUTURE WORKS

We here draw general conclusions and future directions which naturally originate from the results of this Ph.D.. More specific conclusions regarding each topic can be found in the papers of chapter 3 and chapter 4.

In this thesis, we have explored several collective properties of light scattering by disordered cold atomic clouds. In particular, two theoretical predictions have been realized, which are strongly connected to light scattering experiments in São Carlos: the atomic lighthouse effect and the interference fringes of the mirror assisted coherent backscattering. The former phenomenon requires setting up a gradient of magnetic field, which is a common tool in cold atom experiments, used for example for manipulating atoms. The mCBS measurements have already been published and represents a new tool to investigate coherent interference phenomena in disordered atomic clouds, even in the saturated regime. This second line of research is being continued by exploiting the dispersion of light when it propagates over large distances. It allows to obtain different fringe pattern for the different spectral components of the atomic radiation.

Anderson localization studies were performed in two dimensions, where we show that the localization length of light is independent of subradiant decay rates. Such result was possible because the 2D scattering model allows for an accurate computation of the localization length, a very challenging task in 3D. The localization of light in 3D is still an open question, and new methodologies must be pursued at least to understand more clearly why near-field terms suppress localized decay modes. Our work in 2D point to some interesting directions which may facilitate the investigations in 3D. In particular, it was demonstrated that the 2D model is a powerful platform to study the role of polarization effects in the absence of localization transition.

Finally, optical binding with a pair of cold atoms was obtained in the deterministic case, when random spontaneous emission recoils are not taken into account. Although our approach consider only two-atom dynamics, it represents an important first step toward a many-body approach with stochastic quantum simulations.

REFERENCES

1 GUERIN, W.; ROUABAH, M.; KAISER, R. Light interacting with atomic ensembles: collective, cooperative and mesoscopic effects. **Journal of Modern Optics**, v. 64, n. 9, p. 895–907, 2017.

2 ANDERSON, P. W. More is different. **Science**, v. 177, n. 4047, p. 393–396, 1972.

3 DICKE, R. H. Coherence in spontaneous radiation processes. **Physical Review**, v. 93, n. 1, p. 99–110, 1954.

4 SKRIBANOWITZ, N. et al. Observation of dicke superradiance in optically pumped hf gas. **Physical Review Letters**, v. 30, n. 8, p. 309–312, 1973.

5 FRIEDBERG, R.; HARTMANN, S.; MANASSAH, J. Frequency shifts in emission and absorption by resonant systems ot two-level atoms. **Physics Reports**, v. 7, n. 3, p. 101–179, 1973.

6 BONIFACIO, R.; LUGIATO, L. A. Cooperative radiation processes in two-level systems: Superfluorescence. **Physical Review A**, v. 11, n. 5, p. 1507–1521, 1975.

7 GROSS, M.; HAROCHE, S. Superradiance: An essay on the theory of collective spontaneous emission. **Physics Reports**, v. 93, n. 5, p. 301–396, 1982.

8 MALCUIT, M. S. et al. Transition from superfluorescence to amplified spontaneous emission. **Physical Review Letters**, v. 59, n. 11, p. 1189, 1987.

9 PIERRAT, R.; GRÉMAUD, B.; DELANDE, D. Enhancement of radiation trapping for quasiresonant scatterers at low temperature. **Physical Review A**, v. 80, n. 1, p. 013831, 2009.

10 CHABÉ, J. et al. Coherent and incoherent multiple scattering. **Physical Review A**, v. 89, n. 4, p. 043833, 2014.

11 DEVOE, R. G.; BREWER, R. G. Observation of superradiant and subradiant spontaneous emission of two trapped ions. **Physical Review Letters**, v. 76, n. 12, p. 2049–2052, 1996.

12 BARNES, M. D. et al. Far-field modulation of fluorescence decay rates in pairs of oriented semiconducting polymer nanostructures. **Physical Review B**, v. 71, n. 24, p. 241303, 2005.

13 MCGUYER, B. et al. Precise study of asymptotic physics with subradiant ultracold molecules. **Nature Physics**, v. 11, n. 1, p. 32–36, 2015.

14 PAVOLINI, D. et al. Experimental evidence for subradiance. **Physical Review Letters**, v. 54, n. 17, p. 1917–1920, 1985.

15 GUERIN, W.; ARAÚJO, M. O.; KAISER, R. Subradiance in a large cloud of cold atoms. **Physical Review Letters**, v. 116, n. 8, p. 083601, 2016.

16 SCULLY, M. O. et al. Directed spontaneous emission from an extended ensemble of n atoms: Timing is everything. **Physical Review Letters**, v. 96, n. 1, p. 010501, 2006.

17 OLIVEIRA, R. A. de et al. Single-photon superradiance in cold atoms. **Physical Review A**, v. 90, n. 2, p. 023848, 2014.

18 EBERLY, J. H. Emission of one photon in an electric dipole transition of one among n atoms. **Journal of Physics B**, v. 39, n. 15, p. S599, 2006.

19 SCULLY, M. O. Correlated spontaneous emission on the volga. **Laser Physics**, v. 17, n. 5, p. 635–646, 2007.

20 MAZETS, I. E.; KURIZKI, G. Multiatom cooperative emission following single-photon absorption: Dicke-state dynamics. **Journal of Physics B**, v. 40, n. 6, p. F105, 2007.

21 DAS, S.; AGARWAL, G. S.; SCULLY, M. O. Quantum interferences in cooperative dicke emission from spatial variation of the laser phase. **Physical Review Letters**, v. 101, n. 15, p. 153601, 2008.

22 SVIDZINSKY, A. A.; CHANG, J.-T.; SCULLY, M. O. Dynamical evolution of correlated spontaneous emission of a single photon from a uniformly excited cloud of n atoms. **Physical Review Letters**, v. 100, n. 16, p. 160504, 2008.

23 SVIDZINSKY, A.; CHANG, J.-T. Cooperative spontaneous emission as a many-body eigenvalue problem. **Physical Review A**, v. 77, n. 4, p. 043833, 2008.

24 SVIDZINSKY, A. A.; SCULLY, M. O. Evolution of collective n atom states in single photon superradiance: Effect of virtual lamb shift processes. **Optics Communications**, v. 282, n. 14, p. 2894–2897, 2009.

25 SCULLY, M. O. Collective lamb shift in single photon dicke superradiance. **Physical Review Letters**, v. 102, n. 14, p. 143601, 2009.

26 SVIDZINSKY, A. A.; CHANG, J.-T.; SCULLY, M. O. Cooperative spontaneous emission of n atoms: Many-body eigenstates, the effect of virtual lamb shift processes, and analogy with radiation of n classical oscillators. **Physical Review A**, v. 81, n. 5, p. 053821, 2010.

27 SVIDZINSKY, A. A.; ZHANG, X.; SCULLY, M. O. Quantum versus semiclassical description of light interaction with atomic ensembles: Revision of the maxwell-bloch equations and single-photon superradiance. **Physical Review A**, v. 92, n. 1, p. 013801, 2015.

28 BIENAIMÉ, T. et al. Observation of a cooperative radiation force in the presence of disorder. **Physical Review Letters**, v. 104, n. 18, p. 183602, 2010.

29 BUX, S. et al. Cooperative scattering by cold atoms. **Journal of Modern Optics**, v. 57, n. 19, p. 1841–1848, 2010.

30 ARAÚJO, M. O. et al. Superradiance in a large and dilute cloud of cold atoms in the linear-optics regime. **Physical Review Letters**, v. 117, n. 7, p. 073002, 2016.

31 BROMLEY, S. L. et al. Collective atomic scattering and motional effects in a dense coherent medium. **Nature Communications**, v. 7, 2016. doi:10.1038/ncomms11039.

32 BIENAIMÉ, T. et al. Atom and photon measurement in cooperative scattering by cold atoms. **Journal of Modern Optics**, v. 58, n. 21, p. 1942–1950, 2011.

33 _____. Cooperativity in light scattering by cold atoms. **Fortschritte der Physik**, v. 61, n. 2-3, p. 377–392, 2013.

34 ROUABAH, M.-T. et al. Coherence effects in scattering order expansion of light by atomic clouds. **Journal of the Optical Society of America A**, v. 31, n. 5, p. 1031–1039, 2014.

35 BIENAIMÉ, T.; PIOVELLA, N.; KAISER, R. Controlled dicke subradiance from a large cloud of two-level systems. **Physical Review Letters**, v. 108, n. 12, p. 123602, 2012.

36 FENG, W.; LI, Y.; ZHU, S.-Y. Effect of atomic distribution on cooperative spontaneous emission. **Physical Review A**, v. 89, n. 1, p. 013816, 2014.

37 BACHELARD, R. et al. Resonances in mie scattering by an inhomogeneous atomic cloud. **Europhysics Letters**, v. 97, n. 1, p. 14004, 2012.

38 MÁXIMO, C. E. et al. Atomic lighthouse effect. **Journal of the Optical Society of America A**, v. 31, n. 11, p. 2511–2517, 2014.

39 ANDERSON, P. W. Absence of diffusion in certain random lattices. **Physical Review**, v. 109, n. 5, p. 1492–1505, 1958.

40 ABRAHAMS, E. et al. Scaling theory of localization: Absence of quantum diffusion in two dimensions. **Physical Review Letters**, v. 42, n. 10, p. 673–676, 1979.

41 ANDERSON, P. W. The question of classical localization a theory of white paint? **Philosophical Magazine Part B**, v. 52, n. 3, p. 505–509, 1985.

42 LAHINI, Y. et al. Anderson localization and nonlinearity in one-dimensional disordered photonic lattices. **Physical Review Letters**, v. 100, n. 1, p. 013906, 2008.

43 LAURENT, D. et al. Localized modes in a finite-size open disordered microwave cavity. **Physical Review Letters**, v. 99, n. 25, p. 253902, 2007.

44 WIERSMA, D. S. et al. Localization of light in a disordered medium. **Nature**, v. 390, n. 6661, p. 671–673, 1997.

45 STÖRZER, M. et al. Observation of the critical regime near anderson localization of light. **Physical Review Letters**, v. 96, n. 6, p. 063904, 2006.

46 SPERLING, T. et al. Direct determination of the transition to localization of light in three dimensions. **Nature Photonics**, v. 7, n. 1, p. 48–52, 2013.

47 _____. Can 3d light localization be reached in “white paint”? **New Journal of Physics**, v. 18, n. 1, p. 013039, 2016.

48 SKIPETROV, S. E.; SOKOLOV, I. M. Absence of anderson localization of light in a random ensemble of point scatterers. **Physical Review Letters**, v. 112, n. 2, p. 023905, 2014.

49 _____. Magnetic-field-driven localization of light in a cold-atom gas. **Physical Review Letters**, v. 114, n. 5, p. 053902, 2015.

50 MÁXIMO, C. E. et al. Spatial and temporal localization of light in two dimensions. **Physical Review A**, v. 92, n. 6, p. 062702, 2015.

51 WELLENS, T. et al. Coherent backscattering of light by two atoms in the saturated regime. **Physical Review A**, v. 70, n. 2, p. 023817, 2004.

52 ALBADA, M. P. V.; LAGENDIJK, A. Observation of weak localization of light in a random medium. **Physical Review Letters**, v. 55, n. 24, p. 2692–2695, 1985.

53 WOLF, P.-E.; MARET, G. Weak localization and coherent backscattering of photons in disordered media. **Physical Review Letters**, v. 55, n. 24, p. 2696–2699, 1985.

54 BIDEL, Y. et al. Coherent light transport in a cold strontium cloud. **Physical Review Letters**, v. 88, n. 20, p. 203902, 2002.

55 KUPRIYANOV, D. V. et al. Coherent backscattering of light from ultracold and optically dense atomic ensembles. **Laser Physics Letters**, v. 3, n. 5, p. 223, 2006.

56 MORIYA, P. H. et al. Coherent backscattering of inelastic photons from atoms and their mirror images. **Physical Review A**, v. 94, n. 5, p. 053806, 2016.

57 CHU, S. Nobel lecture: the manipulation of neutral particles. **Review of Modern Physics**, v. 70, n. 3, p. 685–706, 1998.

58 COHEN-TANNOUDJI, C. N. Nobel lecture: manipulating atoms with photons. **Review of Modern Physics**, v. 70, n. 3, p. 707–719, 1998.

59 PHILLIPS, W. D. Nobel lecture: laser cooling and trapping of neutral atoms. **Review of Modern Physics**, v. 70, n. 3, p. 721–741, 1998.

60 ASHKIN, A. Acceleration and trapping of particles by radiation pressure. **Physical Review Letters**, v. 24, n. 24, p. 156–159, 1970.

61 BLOCH, I. Ultracold quantum gases in optical lattices. **Nature Physics**, v. 1, p. 23–30, 2005. doi:10.1038/nphys138.

62 KHAYKOVICH, L.; DAVIDSON, N. Compression of a cold atomic cloud by on-resonance laser light. **Journal of the Optical Society of America B**, v. 16, n. 5, p. 702–709, 1999.

63 SAFFMAN, M. Self-induced dipole force and filamentation instability of a matter wave. **Physical Review Letters**, v. 81, n. 1, p. 65–68, 1998.

64 DHOLAKIA, K.; ZEMÁNEK, P. Colloquium: gripped by light: optical binding. **Review of Modern Physics**, v. 82, n. 2, p. 1767–1791, 2010.

65 BURNS, M. M.; FOURNIER, J.-M.; GOLOVCHENKO, J. A. Optical binding. **Physical Review Letters**, v. 63, n. 12, p. 1233–1236, 1989.

66 _____. Optical matter: crystallization and binding in intense optical fields. **Science**, v. 249, n. 4970, p. 749, 1990.

67 METZGER, N. K.; DHOLAKIA, K.; WRIGHT, E. M. Observation of bistability and hysteresis in optical binding of two dielectric spheres. **Physical Review Letters**, v. 96, n. 6, p. 068102, 2006.

68 METZGER, N. K. et al. Measurement of the restoring forces acting on two optically bound particles from normal mode correlations. **Physical Review Letters**, v. 98, n. 6, p. 068102, 2007.

69 KARÁSEK, V.; DHOLAKIA, K.; ZEMÁNEK, P. Analysis of optical binding in one dimension. **Applied Physics B**, v. 84, n. 1, p. 149, 2006.

70 CHAUMET, P. C.; NIETO-VESPERINAS, M. Optical binding of particles with or without the presence of a flat dielectric surface. **Physical Review B**, v. 64, n. 3, p. 035422, 2001.

71 GRZEGORCZYK, T. M.; KEMP, B. A.; KONG, J. A. Stable optical trapping based on optical binding forces. **Physical Review Letters**, v. 96, n. 11, p. 113903, 2006.

72 NG, J. et al. Photonic clusters formed by dielectric microspheres: Numerical simulations. **Physical Review B**, v. 72, n. 8, p. 085130, 2005.

73 SCHLEICH, W. P. **Quantum optics in phase space**. Berlin: Wiley-VCH, 2001.

74 WILKENS, M. Significance of röntgen current in quantum optics: Spontaneous emission of moving atoms. **Physical Review A**, v. 49, n. 1, p. 570–573, 1994.

75 RAIMOND, J. M.; BRUNE, M.; HAROCHE, S. Manipulating quantum entanglement with atoms and photons in a cavity. **Review of Modern Physics**, v. 73, n. 3, p. 565–582, 2001.

76 DAMANET, F. m. c.; BRAUN, D.; MARTIN, J. Master equation for collective spontaneous emission with quantized atomic motion. **Physical Review A**, v. 93, n. 2, p. 022124, 2016.

77 GLAUBER, R. J. The quantum theory of optical coherence. **Physical Review**, v. 130, n. 6, p. 2529–2539, 1963.

78 HILL, T.; SANDERS, B. C.; DENG, H. Cooperative light scattering in any dimension. **Physical Review A**, v. 95, n. 3, p. 033832, 2017.

79 JENKINS, S. D. et al. Optical resonance shifts in the fluorescence of thermal and cold atomic gases. **Physical Review Letters**, v. 116, n. 18, p. 183601, 2016.

80 GRIMM, R.; WEIDEMüLLER, M.; OVCHINNIKOV, Y. B. Optical dipole traps for neutral atoms. **Advances In Atomic, Molecular, and Optical Physics**, v. 42, p. 95–170, 2000. doi.org/10.1016/S1049–250X(08)60186–X.